UNIVERSIDAD DE EXTREMADURA

TESIS DOCTORAL

Cálculo electromagnético rápido de estructuras periódicas de gran tamaño

Alberto Serna Martín

Programa de Doctorado Interuniversitario en Tecnología Aeroespacial: Ingenierías Electromagnética, Electrónica, Informática y Mecánica

2020

UNIVERSIDAD DE EXTREMADURA

TESIS DOCTORAL

Cálculo electromagnético rápido de estructuras periódicas de gran tamaño

Alberto Serna Martín

Programa de Doctorado Interuniversitario en Tecnología Aeroespacial: Ingenierías Electromagnética, Electrónica, Informática y Mecánica

Memoria para optar al Grado de Doctor con Mención Internacional

Conformidad de los directores:

La conformidad del director/es de la tesis consta en el original en papel de esta Tesis Doctoral.
Dr. D. José Manuel Taboada Varela
Dr. D. Luis Landesa Porras

2020

A todos los que me sirvieron de apoyo
en este largo y arduo camino

"Estoy entre aquellos que piensan
que la ciencia tiene una gran belleza.
Un científico en su laboratorio no es solo un técnico,
también es un niño ante fenómenos naturales
que le impresionan como un cuento de hadas....."

- Marie Sklodowska Curie -

Agradecimientos institucionales

- Ministerio de Ciencia, Innovación y Universidades, proyectos FPU00022/15, EST17/00487 y EST18/00014.
- Ministerio de Economía y Competitividad y Fondos FEDER, proyectos MAT2014-58201-C2-1-R, MAT2014-58201-C2-2-R, TACTICA, TEC2017-85376-C2-X-R y MTM2015-63978-P.
- Junta de Extremadura y fondos FEDER, proyectos IB13185, IB18073, GR15052 y GR18055.
- Junta de Extremadura, Fondos FEDER y SferaOne, proyecto GlobalEnergy AA-16-0124-2.
- Xunta de Galicia y Fondos FEDER, proyectos CN2012/279 y CN2012/260 (AtlantTIC).

Agradecimientos personales

En primer lugar, me gustaría mostrar el más obvio de mis agradecimientos. Estar concluyendo esta obra habría sido imposible sin el apoyo de mi familia durante este largo camino. Aquí también entra quien me ha acompañado durante casi media vida, Leticia. Ella ha jugado un papel imprescindible en los últimos 10 años de mi vida y en las decisiones más importantes que he tomado en ese tiempo. Tengo completamente claro que sin ella ni estaría concluyendo este trabajo ni sería la persona que soy a día de hoy. Los siguientes son los de siempre, esa panda de cabritos del 88 que pese a estar ya bastante dispersa consigue juntarse de vez en cuando para alegrar la caja de los bares de Plasencia. En estos años me habéis brindado grandes momentos y alegrías que hicieron más liviano el camino hasta aquí.

Entrando ya en materia más específica, me gustaría dedicar un espacio a las personas que me han acompañado durante esta etapa en el mundo universitario. Comenzaré, como no podría ser de otra forma, por Luis. En primer lugar por el apoyo que me ha brindado brindado estos años de doctorado, pero sobre todo por haber sido un referente no solo como docente o investigador, sino también como persona. Posiblemente nadie sepa hasta qué punto su asignación como mi tutor en el PATT de teleco supuso un punto de inflexión en no pocos aspectos. También a Tabo, por la cantidad de veces que estando hasta arriba ha parado un momento para iluminarme junto a Luis con determinadas cuestiones de la tesis y por esos momentos de intensas discusiones (en el buen sentido) que supusieron unos buenos empujones para esta tesis. Como es de esperar los siguientes son Inma, Larios, Valten, Víctor, Lucía y Carlos, o lo que viene siendo el M3Lab de la UEx. Estoy seguro de que tiene que ser difícil encontrar un grupo de trabajo con mejor ambiente que el nuestro, de otra forma el esfuerzo que ha supuesto realizar esta tesis no hubiera sido tan llevadero.

Tampoco pueden faltarme palabras de agradecimiento para media Politécnica. Creo que estos años no hubieran sido tan entretenidos si Pablo, Torrecilla, Ceballos, Ramón, Carmen, Maribel, Silva, Aurora, etc. no hubiesen puesto su granito de arena entre proyectos, actividades y sobremesas varias. Y no puedo olvidarme de Paco y Faustino, cada ratito de estos cinco años con vosotros en la cafetería ha sido un pequeño soplo de aire fresco.

También tengo que agradecer a la gente del LACE (Politecnico di Torino) la acogida en mis dos estancias con ellos. A Francesca, Javi, Jorge, Marco, Fran, Rosella, David etc. Los conocimientos y la experiencia que adquirí allí contribuyeron a mejorar en

gran medida mi formación como investigador. Aquí merece una mención especial Javi Rivero, quien fue mi codirector de TFG en teleco y que años más tardes, por casualidades de la vida, me invitó en un inocente intercambio de correos a realizar mi primera estancia allí, para más tarde introducirme a los mejores sitios de Torino y a DnD, amén de hacer de lingüista y traductor italiano-español a tiempo completo. Jamás olvidaré los buenos ratos que pasé allí junto a vosotros. Allontanarsi dalla linea gialla. Grazie per tutto.

Y finalmente, y como no podía ser de otra manera, a Tote, Lupe, Viole, Lorena, Eli, Cris y Olga por toda la ayuda que me habéis brindado estos años y por los desahogos que habéis aguantado. Ahora más que nunca, tengo claro que fundar la Asociación de Doctorandos de la UEx junto a vosotros fue una de las mejores cosas que pudimos haber hecho para quienes deciden hacer este camino.

A todos y todas mi infinito agradecimiento.

Resumen

Las estructuras periódicas han sido objeto de creciente interés en el ámbito del electromagnetismo computacional. Se pueden encontrar estructuras de un elevado número de elementos desde ámbitos como la nanotecnología, por su presencia en metamateriales con propiedades electromagnéticas exóticas o en aplicaciones biomédicas, hasta agrupaciones de antenas que logren respuestas de altas prestaciones en sistemas radiantes.

Pese a esta relevancia, el análisis de estas estructuras a través de los métodos actuales supone un reto considerable. Si atendemos a los métodos más precisos, por ejemplo basados en ecuación integral de superficie y método de los momentos (SIE-MoM), el coste computacional resultante es prohibitivo, mientras que otros métodos solo están pensados para estructuras periódicas infinitas.

Esta tesis doctoral tiene por objetivo principal el desarrollo de un método que permita acelerar el análisis de estructuras periódicas finitas mediante métodos iterativos de manera eficiente y transparente, manteniendo la precisión de los métodos basados en SIE-MoM. Para ello, se aprovechan las propiedades que, fruto de las periodicidades, aparecen en las matrices de impedancia, dando lugar a un coste equivalente de $\mathcal{O}(N \log(N))$. A su vez, también pretende el desarrollo de métodos de aceleración mediante compresión de matrices a través del modelado de la potencia emitida y recibida por los elementos de dichas estructuras.

Abstract

The periodic structures have been subject of growing interest in the computational electromagnetics scope. Structures with a large number of elements can be found in a vast plethora of applications, from nanotechnology, for its presence in metamaterials with exotic electromagnetic properties or biomedical applications, to arrays of antennas to attain high performance responses in radiating structures.

Despite this relevance, the analysis of this structures through the present methods suppose a real challenge. If we attend, for example, to the most accurate methods, based on surface integral equation and method of moments (SIE-MoM), the resulting computational cost is prohibitive, whereas other methods are only intended for infinite periodic structures.

This doctoral thesis has as main goal the development of a method intended for the acceleration of the analysis of finite periodic structures through iterative methods in an efficient and transparent way, maintaining the precision of methods based on SIE-MoM. For this, the properties that, as a consequence of the periodicities, appear in impedance matrix are used, obtaining an equivalence cost of $\mathcal{O}(N\log(N))$. It also pretends the development of acceleration methods through matrix compression using for it the modeling of the emitted and received powers by the elements of the structures.

List of publications

International journals

[1] **A. Serna**, M. F. Manzano, L. Landesa, D. M. Solís and J. M. Taboada, "Fast and accurate electromagnetic solutions of finite periodic optical structures",*Optics Express*, vol. 25, pp. 18031-18039, 2017. DOI 10.1364/OE.25.018031.

[2] **A. Serna**, L. J. Molina, J. Rivero, L. Landesa and J. M. Taboada, "Multilayer homogeneous dielectric filler for electromagnetic invisibility",*Scientific Reports*, vol. 8, no. 1, 2018. DOI 10.1038/s41598-018-32070-5.

[3] Inma. T. Castro, Luis Landesa and **Alberto Serna**, "Modeling the Energy Harvested by an RF Energy Harvesting System Using Gamma Processes",*Mathematical Problems in Engineering*, vol. 2019, Article ID 8763580, 12 pages, 2019. DOI 10.1155/2019/8763580.

National and international conferences

[1] L. Landesa, M. F. Manzano, **A. Serna**, J. M. Taboada and D. M. Solís, "Fast solution of periodic electromagnetic problems using surface integral equations," *European Conference on Numerical Mathematics and Advance Applications (ENUMATH 2015)*, Ankara (Turkey), September, 2015. **Invited talk**.

[2] **A. Serna**, M. F. Manzano, L. Landesa, D. M. Solís and J. M. Taboada, "Electromagnetic analysis of periodic structures with slotFFT algorithm," *10th European Conference on Antennas and Propagation (EuCAP 2016)*, Davos (Switzerland), 12-15 April. 2016. **Invited talk**.

[3] **A. Serna**, L. Landesa, M. F. Manzano and J. M. Taboada, "Distributed macrobasis decomposition for the electromagnetic solution of large periodic structures," *International Applied Computational Electromagnetics Society Symposium (ACES 2017)*, Firenze (Italy), 27-31 March, 2017.

[4] L. Landesa, J. M. Taboada, J. L. Campón, **A. Serna**, F. Obelleiro, J. L. Rodríguez, D. M. Solís and M. Araujo, "Successes and frustrations in the solution of large electromagnetic problems in supercomputers," *International Applied Computational Electromagnetics Society Symposium (ACES 2017)*, Firenze (Italy), 27-31 March, 2017. **Invited talk**.

[5] L. Landesa, **A. Serna**, M. F. Manzano, J. M. Taboada and D. M. Solís, "SlotFFT techniques for fast computation of large and periodic electromagnetics problem," *2017 Computing and Electromagnetics International Workshop (CEM 2017)*, Barcelona (Spain), 26-28 June, 2017.

[6] I. T. Castro, L. Landesa and **A. Serna**, "Applications of the gamma process in storage models: energy harvesting systems," *10th IMA International Conference on Modelling in Industrial Maintenance and Reliability (MIMAR 2018)*, Manchester (United Kingdom), 12-15 June, 2018.

[7] **A. Serna**, L. Landesa, M. F. Manzano and J. M. Taboada, "Solving extremely large periodic structures through slot FFT techniques," *XXXIII Simposium Nacional de la Unión Científica Internacional de Radio (URSI 2018)*, Granada (Spain), 5-7 September, 2018.

[8] L. Landesa, **A. Serna** and J. M. Taboada, "macrobases desacopladas en potencia para el método de los momentos de dispersores dieléctricos," *XXXIII Simposium Nacional de la Unión Científica Internacional de Radio (URSI 2018)*, Granada (Spain), 5-7 September, 2018. **Invited talk**.

[9] **A. Serna**, J. Tobón, J. Rivero, L. Landesa and F. Vipiana, "Acceleration of Finite Periodic Structures Analysis through Matrix Compression Techniques,"

13th European Conference on Antennas and Propagation (EuCAP 2019), Krakow (Poland), 31 March-5th April, 2019.

[10] **A. Serna**, L. Landesa and J. M. Taboada, "Acceleration of Finite Periodic Structure Analysis through Full-Domain Basis for Matrix Compression," *2019 IEEE International Symposium on Antennas and Propagation and USNC-URSI Radio Science Meeting (AP-S/URSI 2019)*, Atlanta (USA), 7-12 July, 2019.

[11] L. Landesa , **A. Serna** and J. M. Taboada, " Aceleración de problemas periódicos finitos mediante bases desacopladas y slotFFT," *XXXIV Simposium Nacional de la Unión Científica Internacional de Radio (URSI 2018)*, Sevilla (Spain), 4-6 September, 2019.

[12] **A. Serna**, L. Landesa and J. M. Taboada, "Electromagnetic analysis of finite arrays with aperiodical element-wise materials," *International Conference on Electromagnetics in Advanced Applications (ICEAA 2019)*, Granada (Spain), 9-13 September, 2019. **Invited talk**.

[13] **A. Serna**, L. Landesa and J. M. Taboada, "Application of Matrix Compression Methods for Efficient Preconditioning Finite Periodic Structures," *XXXV Simposium Nacional de la Unión Científica Internacional de Radio (URSI 2020)*, Virtual, 2-4 September, 2020.

Contents

1 Introduction **1**
- 1.1 Motivations of the thesis . . . 1
- 1.2 Objectives . . . 2
- 1.3 Contribution of the thesis . . . 3
- 1.4 Structure of the thesis . . . 4

2 Surface Integral Equation-Method of Moments **7**
- 2.1 Method of moments . . . 8
- 2.2 Surface integral equation formulation . . . 10
  - 2.2.1 Tangential formulation . . . 13
  - 2.2.2 Normal formulation . . . 14
  - 2.2.3 Combined formulation . . . 15
- 2.3 Application of the formulation to multiple penetrable objects . . . 16

3 Efficient analysis of finite periodic structures **21**
- 3.1 Introduction . . . 22
- 3.2 SlotFFT Algorithm . . . 23
  - 3.2.1 Single sampling SlotFFT approach . . . 24
  - 3.2.2 Double sampling SlotFFT approach . . . 30
- 3.3 Application to finite periodic structures . . . 33
- 3.4 Extension to aperiodic element-wise materials structures . . . 41
- 3.5 Extension to roughly finite periodic structures . . . 43
  - 3.5.1 Validation and application . . . 46

4 Matrix compression for the acceleration of periodic CEM problems **51**
- 4.1 Introduction . . . 52
- 4.2 Full-domain power decoupled macrobasis . . . 53
  - 4.2.1 Definitions and formulation . . . 54
  - 4.2.2 Macrobasis generation . . . 61
  - 4.2.3 Macrobasis representativeness . . . 63
- 4.3 Skeletonization scheme . . . 69
- 4.4 Integration of matrix compression methods into slotFFT . . . 71
- 4.5 Application and results . . . 72

4.6 Application of matrix compression for preconditioning periodic problems 79

5 Conclusion and future lines **83**
5.1 Conclusion 83
5.2 Future lines 85

List of Tables

2.1 Values for the coefficients for the JMCFIE, CTF, PMCHWT and CNF formulations. 16

4.1 Comparison of the speed-up solving the problem through GMRES and error introduced by compression through skeletons in the superficial electric currents and in the RCS for a PEC problem. 74
4.2 Comparison of the speed-up solving the problem through GMRES and error introduced by compression through macrobasis in the superficial electric currents and in the RCS for a PEC problem. 75
4.3 Comparison of the speed-up solving the problem through GMRES and error introduced by compression through macrobasis and skeletons in the superficial electric currents and in the RCS for a PEC problem. . . 75
4.4 Comparison of the speed-up solving the structure shown in Fig. 4.18 through GMRES and error introduced by compression through macrobasis in the superficial electric currents and in the RCS for a plasmonic problem. 78

List of Figures

1.1 Example of the structure of a SERS substrate composed by gold nanospheres. 1

1.2 Example a structure composed of gold nanocubes disposed randomly whithin a periodic array of Huygens' surfaces. 4

2.1 Arbitrary body used as example for the development for the formulation of the surface integral equation. 10

2.2 Representation of the equivalent problem of the example shown in Fig. 2.1. 11

2.3 Generic example with multiple bodies used for the development of the extension of the formulation. 17

3.1 Logarithmic representation of an impedance matrix of the periodic linear array with periodic features remarked. 24

3.2 Generic periodic linear array with M bodies. 24

3.3 Comparison of the memory and computing time needed with MoM and single slotFFT method for 1, 2 and 3 dimensional patterns. 29

3.4 Comparison of the computing time needed with MoM and single and double sampling versions of the slotFFT method for one dimensional pattern. 32

3.5 Representation of the surface electric and magnetic currents obtained through the CEM analysis of a cube-shaped array of dielectric spheres ($\epsilon_r = 3$ and $\mu_r = 1$) of $\lambda/2$ diameter and a separation of $6\lambda/10$ between centers for an incident plane wave ($\theta = 0°$) with 780nm of wavelength. . 33

3.6 Representation of the scattering cross section at $\lambda = 780$nm obtained through the computation of the currents shown in Fig. 3.5. 34

3.7 Representation of a SERS substrate composed by 200×200 gold nanospheres. 35

3.8 Representation of the SERS intensity computed for the substrate shown in Fig. 3.7. 36

3.9 Representation of the RCS at $\lambda = 550$nm of a cube-shaped array of dielectric nanocubes with $\epsilon = 3$ of $\lambda/10$ side and a separation of $\lambda/5$ between centers obtained using the method of moments accelerated with slotFFT compared to the Maxwell-Garnett and Bruggerman homogeneization methods. 37
3.10 Representation of the surface electric and magnetic currents obtained through the CEM analysis of a simple helix for an incident plane wave ($\theta = 0°$) with 600nm of wavelength. 38
3.11 Scattering, absorption and extinction cross sections of the helical structure of Fig. 3.10 in the optical range for incident plane waves ($\theta = 0°$). 39
3.12 Representation of a double helical structure composed by 2x60 gold nanorods of 25nm of length. 40
3.13 Representation of the circular dichroism (left) and the extinction cross section (right) of the double helical structure shown in Fig. 3.12 for normal incidence ($\theta = 180°$) from 400nm to 1200nm. 40
3.14 Analyzed periodic array, composed by 20×20 dielectric spheres composed of multiple materials distributed arbitrarily(gold, silver, copper and silica) of λ diameter separated by 2λ. 41
3.15 MVP computing times for MoM, double slotFFT and double slotFFT for aperiodic element-wise material structures. 42
3.16 Representation of the RCS at $\lambda = 550$nm ($\epsilon_r = -5.9310 - j2.0971$ for gold, $\epsilon_r = -12.9374 - j0.4287$ for silver, $\epsilon_r = -5.6549 - j5.1989$ for cooper and $\epsilon_r = 2.1756 - j2.36e-7$ for silica) obtained for the structure shown in Fig. 3.14. 43
3.17 Representation of the application of the Huygens' equivalence theorem. 44
3.18 Representation of the steps to approach a generic problem with two bodies enclosed by Huygens' surfaces. 45
3.19 Surface electric currents distribution for the validation example of the integration on the Huygen's equivalence theorem compared to the straight approach. 46
3.20 Comparison of the scattering diagrams obtained from the currents shown in Fig. 3.19 using the straight and the Huygen's equivalence theorem procedure. 47
3.21 Structure composed by quasi-arbitrary distributed PEC cubes of 0.6λ of side and the associated periodic array of Huygen's surfaces. 48
3.22 Surface electric currents distribution obtained for the structure shown in Fig. 3.21 using the Huygens' equivalence theorem for its analysis as a periodic structure with slotFFT. 49
3.23 Scattering diagram obtained from the currents shown in Fig. 3.22. . . . 49

4.1 Radiation of an object as a result of electric and magnetic currents in the interior. Equivalent problem for an homogeneous object. 55

4.2 Representation of several low-order macrobasis computed for a dielectric sphere of 2λ of diameter for both electric and magnetic surface currents. 63
4.3 Representation of the power of each macrobasis (σ_i^2) for multiple geometries made of gold at 550nm. 64
4.4 Representation of the total power emitted by the first i macrobasis pondered by its corresponding coefficients over the total for multiple geometries made of gold at 550nm. 64
4.5 Representation of the total power emitted by the first i macrobasis over the total for multiple geometries made of gold at 550nm. 65
4.6 Comparison of the normalized RCS of a sphere of 2λ of diameter made of gold $\epsilon_r = -8.00 - j1.66$ at 550nm using different number of macrobasis functions per square wavelength. In blue the RCS with all the basis, in red the resulting RCS partially using the set of macrobasis. 66
4.7 Representation of the invisibilized object and comparison of the power emitted by the macrobasis of the object and the object invisibilized. . . 67
4.8 Comparison of the RCS for hollow sphere made of silica with $\lambda/2$ of diameter and the same sphere with a multilayer dielectric filler for invisibilizating it. 67
4.9 Comparison of the normalized RCS of arrays of 3×3 spheres of 2λ of diameter with different separations made of gold ($\epsilon_r = -8.00 - j1.66$) at 550nm obtained with complete SIE-MoM and SIE-MoM with a partial set of macrobasis. 68
4.10 Representation of the $\mathbf{Z}_s$ matrix for a cube with 18 RWG basis. 69
4.11 Representation of a nanorod and its associated proxy surface with 180 points (left) and its dominant basis after applying the skeletonization process with a tolerance of 0.001, achieving a compression rate of 87.6%. 70
4.12 Representation of the matrices of the skeleton scheme generated by the interpolative decomposition. 70
4.13 Analyzed periodic array, composed by 20×20 PEC spheres of $\lambda/6$ radius separated by $2\lambda/3$. 72
4.14 Comparison of the scattering diagrams of the proposed setups for the structure shown in Fig. 4.13 using skeletons with the scattering obtained through uncompressed slotFFT. 73
4.15 Comparison of the scattering diagrams of the proposed setups for the structure shown in Fig. 4.13 using macrobasis with the scattering obtained through uncompressed slotFFT. 74
4.16 Comparison of the scattering diagrams of the proposed setups for the structure shown in Fig. 4.13 using macrobasis and skeletons with the scattering obtained through uncompressed slotFFT. 76
4.17 Analyzed periodic array, composed by 25×25 gold spheres of λ diameter separated by 2λ. 77

4.18 Comparison of the scattering diagrams of the proposed setups for the structure shown in Fig. 4.17 using macrobasis with the scattering obtained through uncompressed slotFFT analyzed at λ=550nm ($\epsilon_r = -5.9310 - j2.0971$). 77
4.19 Representation of the RCS at $\lambda = 550$nm ($\epsilon_r = -5.9310 - j2.0971$ for gold, $\epsilon_r = -12.9374 - j0.4287$ for silver, $\epsilon_r = -5.6549 - j5.1989$ for cooper and $\epsilon_r = 2.1756 - j2.36e - 7$ for silica) for the uncompressed system and applying a 90% compression rate using macrobasis obtained for the structure shown in Fig. 3.14. 78
4.20 MVP computing times for MoM, double sampling slotFFT, double sampling slotFFT for aperiodic element-wise material structures and its compressed versions using 90% and 97.5% compression rates. 79
4.21 Representation of a canonical structure composed of 20×20 spheres of λ diameter and a separation of 2λ between centers. 80
4.22 Evolution of the convergence vs. number of iterations of the iterative solution of the structure shown in Fig. 4.21 made of silica ($\epsilon_r = 2.1756 - j2.36e - 7$ at 550nm) preconditioned with a block-jacobi preconditioner (in blue) vs. matrix-compressed preconditioner (in red). 81
4.23 Representation of a SERS substrate composed of 20×20 gold nanospheres ($\epsilon_r = -5.9310 - j2.0971$ at 550nm) of 55nm of diameter and a separation of 57nm between centers. 82
4.24 Evolution of the convergence vs. number of iterations of the iterative solution of the structure shown in Fig. 4.23 made of gold ($\epsilon_r = -5.9310 - j2.0971$) preconditioned with a block-jacobi preconditioner (in blue) vs. matrix-compressed preconditioner (in red). 82

Chapter 1

Introduction

Contenido

1.1 Motivations of the thesis 1

1.2 Objectives 2

1.3 Contribution of the thesis 3

1.4 Structure of the thesis 4

1.1 Motivations of the thesis

One of the main motivations of this thesis becomes from the contact of the research group with the biomedicine field. Within biomedicine, there are several cases where large periodic structures are useful for certain applications. Two examples of this that will be present in this thesis are surface-enhanced Raman spectroscopy (SERS), visible in Fig. 1.1 substrates or double-helix structures for dichroism applications.

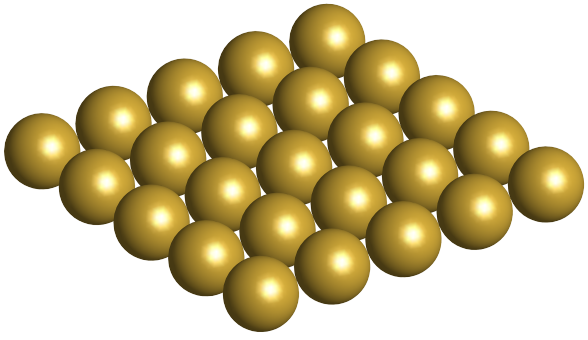

Figure 1.1: Example of the structure of a SERS substrate composed by gold nanospheres.

In particular, those problems that present some periodic patterns become especially costly to analyze. This is due to the combination of dense mesh discretization with the high number of elements that is commonly present in this kind of problems. This fact causes a limitation on the problem size that most of the current computational electromagnetics (CEM) frameworks can approach. Some examples of this are finite elements method (FEM) or integral equations and method of moments. In addition to this, the fact that the structures are finite imposes a limitation for other methods, i.e. Floquet harmonics theory.

As a solution to this, the multilevel fast multipole algorithm (MLFMA), with which the research group posses a strong background and one of the most solid frameworks in CEM, came into scene. Despite of some stages of the process (aggregation, translation and dissaggregation), the solutions obtained through its application are very accurate, providing an efficient level without competitors. This motivated its application for the new challenges that the research group was facing.

However, in that moment a new open problem was posed, giving place to the development of this thesis. The physical periodicity of this kind of structures should be present in some way in the matrix system used to solve them with surface integral equation-method of moments (SIE-MoM). This thesis was carried out with the goal of developing an algorithm capable of taking advantage of the periodicity of these structures to efficiently solve finite periodic problems with SIE-MoM in a transparent way.

Another feature present in these problems is the separation between elements. In the scope of CEM is common to find methods that perform the compression of the interactions between well separated parts of the problem. This is achievable due to the smaller number of unknowns to compute the far field couplings. In particular, periodic structures are especially suitable for compression methods, as the element to compress is always the same, there is an important saving in the computation of the interpolation and anterpolation matrix applied to perform the compression. This particular property motivated to the author and the advisers to undertake the development of macrobasis applicable in a distributed and efficient way.

1.2 Objectives

Therefore, after introducing the motivations of this thesis, the main objectives of this work are detailed bellow.

- The development of an algorithm to carry out the resolution of periodic and finite

CEM problems using the SIE-MoM in a transparent and efficient way.

- The development of a new full domain power-decoupled macrobasis for perfect electric conductors (PEC) and dielectric problems applicable to matrix compression.

- Application of macrobasis and skeletons for matrix compression to finite periodic structures for the acceleration of the solver.

- The development of a framework capable of apply the previous methods to other kind of applications and problems.

1.3 Contribution of the thesis

The main contribution of this thesis is the development of a framework to perform the electromagnetic analysis of finite periodic problems in an efficient way within the SIE-MoM developed by the research group where this work was carried out. This can be described through the following lines:

- Development of an efficient algorithm called slotFFT for finite periodic problems. The slotFFT algorithm is capable of approach structures with multiple periodic patterns achieving a computing cost reduction from $\mathcal{O}(N^2)$ to an equivalent cost of $\mathcal{O}(nM \log M)$ in the matrix-vector product (MVP), being n the number of unknowns of the periodic element, M the number of the elements in the structure and $N = nM$. At the same time, the number of elements in the matrix needed to solve the problem is reduced from $(nM)^2$ to $2^p n^2 M$, where p is a natural number related to the patterns of the periodicity present in the structure.

- Development of full domain power decoupled macrobasis for PEC and dielectric problems. The main property of these new macrobasis is the capability of properly describing the radiated power with a small number of basis over the total. Unlike other methods, like skeletons generated through interpolative decomposition (ID) method, these macrobasis cover the full domain. This supposes a slightly improvement in the precision in comparison to the referenced method.

- Integration of matrix compression methods (MCM) with slotFFT. In particular, the macrobasis introduced above and the skeletons method were integrated within the slotFFT algorithm. Through this, high acceleration rates in the MVP and memory reduction for large periodic problems are achieved, combined with a controlled impact over the precision of the solution.

- As last contribution, the Huygens' equivalence theorem is introduced into the slotFFT framework in order to extend the application of the method to non periodic distributed structures. Isolating each element of a finite structure by a periodic array of closed surfaces, imperfect structures and structures composed by different kind of elements can be analyzed as a periodic problem. An example of this application is shown in Fig. 1.2, where an array composed of gold nanocubes is disposed randomly within a periodic array of closed surfaces.

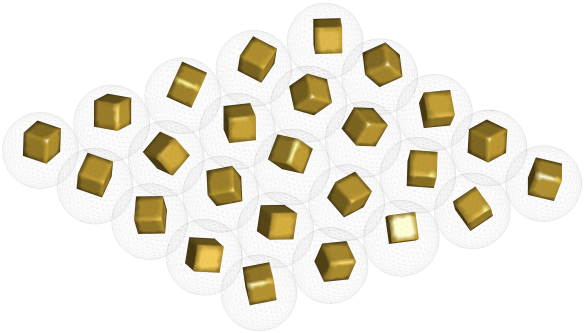

Figure 1.2: Example a structure composed of gold nanocubes disposed randomly whithin a periodic array of Huygens' surfaces.

1.4 Structure of the thesis

This document has been structured in six chapters. The first, and present, one, introduces formally the scope of the thesis, the objectives and the contributions of the work.

The second chapter is a detailed introduction to the CEM core that lies underneath of the methods used and developed in this work. In particular, the whole SIE-MoM will be explained.

The third chapter introduces the state-of-the-art of the different approached in scope of periodic structures. The slotFFT algorithm is fully formulated and analyzed, and the results attained through its application to problems are reviewed. Then, in a last section, it is described the Huygens' equivalence theorem for CEM problems and its application to approach non-periodic distributed problems as periodic problems.

Chapter forth introduces the application of MCM techniques to CEM problems. It comprehends a state-of-the-art review on the widespread methods, the formulation of the full domain power-decoupled macrobasis and its integration into the slotFFT algorithm. This chapter also includes the integration of the skeletons and the ID method

into slotFFT, carried out during an international research visit in the Politecnico di Torino. The last part of the chapter shows an study on the efficiency obtained and its impact over the precision.

The last chapter summarizes the main conclusions and remarks of the developed work, as well as some future lines and cases of application of the framework.

Chapter 2

Surface Integral Equation-Method of Moments

Contenido

2.1 Method of moments 8

2.2 Surface integral equation formulation 10

2.2.1 Tangential formulation 13

2.2.2 Normal formulation 14

2.2.3 Combined formulation 15

2.3 Application of the formulation to multiple penetrable objects 16

This chapter describes the fundamental core that lies underneath every single procedure implemented within this thesis: surface integral equation-method of moments. The surface-integral equation-method of moments (SIE-MoM) core used in this thesis applicable to arbitrary penetrable bodies and its implementation is explained in depth in [1, 2]. This chapter introduces part of that work into this thesis for the sake of consistency and to ease the comprehension of the core methods that are used. The study of the precision of the SIE-MoM core used in this thesis, as well as its convergence, can be consulted in [3–5]. Also, some examples of its capability of analyzing large and complex problems can be consulted in [6–8].

The chapter has been structured in a way that every particular aspect of the framework is well distinguishable from the rest, so they can be found quickly when referenced in the next chapters. First, MoM is introduced departing from a generic continuous function to conversion to a matrix system that allows its solving. Then, in the second

section, the formulation for a single arbitrary object is described. This comprehends the tangential and normal formulations, and their combination.

2.1 Method of moments

The method of moments [9] was first introduced into computational electromagnetics by R.F. Harrington, and it is one of the most widespread approaches in CEM. In particular, along with its application to SIE, MoM has been one of the strong work lines of the researchers that advised this thesis. MoM allows the resolution of continuous integral equations by transforming them into a finite discrete system of linear equations solvable through a numeric approach.

Equation (2.1) represents a general problem: $\mathbf{g}$ is a known function that induces a response $\mathbf{f}$, that we want to obtain, and $\mathcal{L}$ a functional operator that relates $\mathbf{g}$ with its response $\mathbf{f}$.

$$\mathcal{L}(\mathbf{f}) = \mathbf{g} \tag{2.1}$$

In order to solve eq. (2.1), the first step is to approximate $\mathbf{f}$ by performing its expansion into a series composed of N discrete known functions $\mathbf{f}_n$ multiplied element-wise by α_n unknown complex coefficients, as shown in eq. (2.2).

$$\mathbf{f} \simeq \sum_{n=1}^{N} \alpha_n \mathbf{f}_n \tag{2.2}$$

By replacing eq. (2.2) into eq. (2.1) we obtain eq. (2.3), where α_n can be extracted due to the linearity of $\mathcal{L}$.

$$\sum_{n=1}^{N} \alpha_n \mathcal{L}(\mathbf{f}_n) \simeq \mathbf{g} \tag{2.3}$$

In order to be able to solve eq. (2.3), we need to apply it over M points, with $M \geq N$. For this, $\mathbf{g}$ is projected over a set of functions $\mathbf{w}_m$, called test functions. By testing eq. (2.3) with this set of functions we obtain a system of M linear equations, as shown in eq. (2.4).

$$\sum_{n=1}^{N} \alpha_n \langle \mathbf{w}_m, \mathcal{L}(\mathbf{f}_n) \rangle = \langle \mathbf{w}_m, \mathbf{g} \rangle \tag{2.4}$$

Its application is performed through a symmetric product, defined in eq. (2.5), or a scalar product, defined in eq. (2.6), where * indicates the conjugated complex. Since this thesis, as will be stated later, will use real basis functions as basis, both products are equals.

$$\langle \mathbf{f}, \mathbf{g} \rangle = \int_S \mathbf{f} \cdot \mathbf{g} ds \tag{2.5}$$

$$\langle \mathbf{f}, \mathbf{g} \rangle = \int_S \mathbf{f} \cdot \mathbf{g}^* ds \tag{2.6}$$

Developing eq. (2.4) into its matrix from we can write it as shown in eq. (2.7), where $\mathbf{Z}$ is called the impedance matrix or MoM matrix, $\boldsymbol{I}$ is the unknowns vector with the coefficients that weighs $\mathbf{f}_n$ and $\boldsymbol{V}$ is the vector of excitation, defined in eq. (2.8) and eq. (2.9).

$$\mathbf{Z} \cdot \boldsymbol{I} = \boldsymbol{V}, \tag{2.7}$$

$$\mathbf{Z} = \begin{bmatrix} \langle \mathbf{w}_1, \mathcal{L}(\mathbf{f}_1) \rangle & \langle \mathbf{w}_1, \mathcal{L}(\mathbf{f}_2) \rangle & \cdots & \langle \mathbf{w}_1, \mathcal{L}(\mathbf{f}_N) \rangle \\ \langle \mathbf{w}_2, \mathcal{L}(\mathbf{f}_1) \rangle & \langle \mathbf{w}_2, \mathcal{L}(\mathbf{f}_2) \rangle & \cdots & \langle \mathbf{w}_2, \mathcal{L}(\mathbf{f}_N) \rangle \\ \vdots & \vdots & \ddots & \vdots \\ \langle \mathbf{w}_N, \mathcal{L}(\mathbf{f}_1) \rangle & \langle \mathbf{w}_N, \mathcal{L}(\mathbf{f}_2) \rangle & \cdots & \langle \mathbf{w}_N, \mathcal{L}(\mathbf{f}_N) \rangle \end{bmatrix} \tag{2.8}$$

$$\boldsymbol{I} = \begin{bmatrix} \alpha_1 \\ \alpha_2 \\ \vdots \\ \alpha_N \end{bmatrix} ; \boldsymbol{V} = \begin{bmatrix} \langle \mathbf{w}_1, \mathbf{g} \rangle \\ \langle \mathbf{w}_2, \mathbf{g} \rangle \\ \vdots \\ \langle \mathbf{w}_N, \mathbf{g} \rangle \end{bmatrix} \tag{2.9}$$

Now, the system in eq. (2.8) can be solved by matrix inversion or, as is usual due to the size of the resulting system in the field, by the use of iterative methods like generalized minimal residue (GMRES).

In this procedure, the choice of the functions for $\mathbf{f}_n$ and $\mathbf{w}_n$ plays a major role over the precision, the complexity for evaluating some terms or the conditioning of the impedance matrix. Also, using the same functions basis for $\mathbf{f}_n$ and $\mathbf{w}_n$ permits the application of the Galerkin method, allowing relevant improvements in the computation time due to the symmetries that appear into the impedance matrix. In the case of of this work, the $\mathbf{f}_n$ and $\mathbf{w}_n$ functions used are RWG basis functions [10], introduced by Rao, Wilton and Glisson in 1982. The achievable precision of this method is also

dependent on N. Otherwise informed, the criteria applied to every problem of this thesis will be a density of 300 RWG basis per square wavelength. This criterion comes from applying 10 basis per wavelength in a linear approach. Extending this criterion to a surface we obtain 100 surface basis conformed by squares per square wavelength. However, as full RWG basis are being used, this is multiplied by 2 as the meshes is conformed by triangles, and by 1.5 as each triangle is, in a general case, part of 3 basis shared with the adjacent triangles.

2.2 Surface integral equation formulation

The introduction to the SIE formulation is presented for a single arbitrary-shaped body composed by an electromagnetic penetrable material. Notice that the temporal harmonic $\exp(j\omega t)$ will be omitted in the whole development. The notation of the base problem is shown in Fig. 2.1. $\mathbf{E}_{i1}$ and $\mathbf{H}_{i1}$ denote the impinging electric and magnetic fields respectively from region R_1, S is the arbitrary surface separating the two regions that compose the problem, ϵ_i and μ_i are the relative constitutive parameters of the material that composes the region R_i, $\widehat{\mathbf{n}}_i$ is the unitary norm to S aiming to region R_i.

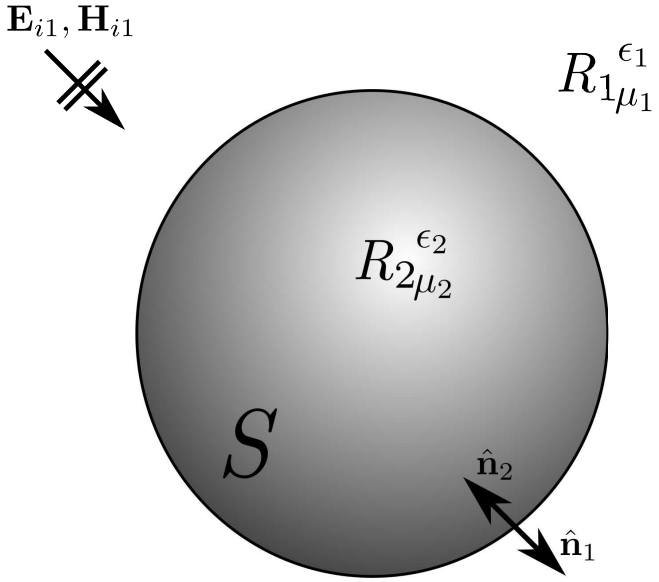

Figure 2.1: Arbitrary body used as example for the development for the formulation of the surface integral equation.

From this, we will develop the field integral equations (FIE), which will be the core of the resolution process. This can be classified into four different equations, depending on the boundary conditions and their application:

1. N-EFIE (Normal Electric Field Integral Equation).
2. N-MFIE (Normal Magnetic Field Integral Equation).
3. T-EFIE (Tangencial Electric Field Integral Equation).
4. T-MFIE (Tangencial Magnetic Field Integral Equation).

To start with, we depart from the problem in Fig. 2.1, we develop an equivalent problem, shown in Fig. 2.2, where $\mathbf{J}_i$ y $\mathbf{M}_i$ are respectively the electric and magnetic surface current densities over the surface S of region R_i.

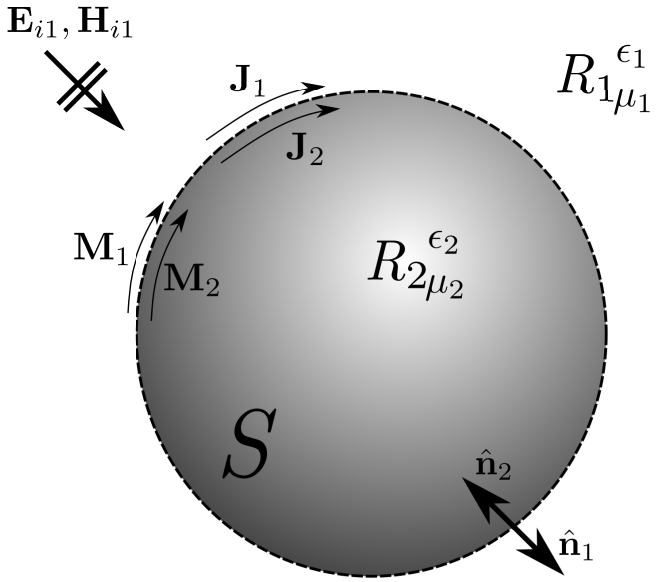

Figure 2.2: Representation of the equivalent problem of the example shown in Fig. 2.1.

The equivalent theorem [11] relates both the electric and magnetic surface currents with the total fields over the regions, as shown in eq. (2.10) and (2.11) respectively.

$$\mathbf{M}_i = -\hat{\mathbf{n}}_i \times \mathbf{E}_i^t \tag{2.10}$$

$$\mathbf{J}_i = \hat{\mathbf{n}}_i \times \mathbf{H}_i^t \tag{2.11}$$

The total $\mathbf{E}_i^t$ and $\mathbf{H}_i^t$ fields can be separated, as shown in eq. (2.12) and eq. (2.12), into the sum of the incident fields, denoted with superscript ^{i}, and the scattered fields, denoted with superscript ^{s}, which depend on the electric and magnetic surface currents.

$$\mathbf{E}_i^t = \mathbf{E}_i^i + \mathbf{E}_i^s(\mathbf{J}_i, \mathbf{M}_i) \tag{2.12}$$

$$\mathbf{H}_i^t = \mathbf{H}_i^i + \mathbf{H}_i^s(\mathbf{J}_i, \mathbf{M}_i) \tag{2.13}$$

The scattered fields by the currents can be calculated as shown in eq. (2.14) and eq. (2.15), where η_i is the intrinsic impedance of the region R_i, that can be calculates as $\eta_i = \sqrt{\mu_i/\varepsilon_i}$.

$$\mathbf{E}_i^s(\mathbf{J}_i, \mathbf{M}_i) = -\eta_i \mathcal{L}_i(\mathbf{J}_i) + \mathcal{K}_i(\mathbf{M}_i) \tag{2.14}$$

$$\mathbf{H}_i^s(\mathbf{J}_i, \mathbf{M}_i) = -\mathcal{K}_i(\mathbf{J}_i) - \frac{1}{\eta_i}\mathcal{L}_i(\mathbf{M}_i) \tag{2.15}$$

$\mathcal{L}(\cdot)$ and $\mathcal{K}(\cdot)$ are the integral operators defined in eq. (2.16) and eq. (2.17) respectively, where $\mathbf{r}$ are the observation points, $\mathbf{r}'$ the source points, k_i the wavenumber in region R_i, $G_i(\mathbf{r}, \mathbf{r}')$ the Green function in the region R_i and $\mathcal{K}_i^{PV}$ the principal value of integral operator $\mathcal{K}(\cdot)$, defined in eq. (2.18).

$$\mathcal{L}_i(\mathbf{X}_i) = jk_i \left[\int_S \mathbf{X}_i(\mathbf{r}') G_i(\mathbf{r}, \mathbf{r}') dS' + \frac{1}{k_i^2} \nabla \int_S \nabla' \cdot \mathbf{X}_i(\mathbf{r}') G_i(\mathbf{r}, \mathbf{r}') dS' \right] \tag{2.16}$$

$$\mathcal{K}_i(\mathbf{X}_i) = \mathcal{K}_i^{PV} + \frac{1}{2}\widehat{\mathbf{n}}_i \times \mathbf{X}_i \tag{2.17}$$

$$\mathcal{K}_i^{PV} = \int_{S,PV} \mathbf{X}_i(\mathbf{r}') \times \nabla G_i(\mathbf{r}, \mathbf{r}') dS' \tag{2.18}$$

Departing from eq. (2.10) and eq. (2.11) two integral equations can be obtained: the electric field integral equation (EFIE) and the magnetic field integral equation (MFIE) respectively. Depending on how the fields are projected over the surface S, two different kind of formulations can be obtained for both integral equations: tangential formulation, developed in subsection 2.2.1, and normal formulation, developed in subsection 2.2.2.

2.2.1 Tangential formulation

Applying the product by $\widehat{\mathbf{n}}$ to both sides of eq. (2.10) and eq. (2.11) over the surface S we obtain the tangential electric and magnetic integral equations. Developing them, taking into account eq. (2.12), eq. (2.13), eq. (2.14) and eq. (2.15) and introducing them into the result of the described product we obtain eq. (2.19) and eq. (2.20).

$$\text{T-EFIE}_i : (\eta_i \mathcal{L}_i(\mathbf{J}_i) - \mathcal{K}_i^{PV}(\mathbf{M}_i))_{tan} + \frac{1}{2}\widehat{\mathbf{n}}_i \times \mathbf{M}_i = \mathbf{E}^i_{i,tan} \tag{2.19}$$

$$\text{T-MFIE}_i : (\mathcal{K}_i^{PV}(\mathbf{J}_i) + \frac{1}{\eta_i}\mathcal{L}_i(\mathbf{M}_i))_{tan} - \frac{1}{2}\widehat{\mathbf{n}}_i \times \mathbf{J}_i = \mathbf{H}^i_{i,tan} \tag{2.20}$$

The applied boundary conditions to the problem consider the continuity of the tangential fields over the surface S, as shown in eq. (2.21) and eq. (2.22), with $\widehat{\mathbf{n}} = \widehat{\mathbf{n}}_1 = -\widehat{\mathbf{n}}_2$.

$$\widehat{\mathbf{n}} \times (\mathbf{H}_1^t - \mathbf{H}_2^t) = 0 \tag{2.21}$$

$$\widehat{\mathbf{n}} \times (\mathbf{E}_1^t - \mathbf{E}_2^t) = 0 \tag{2.22}$$

The combination of eq. (2.19) and eq. (2.20) for the inner and external regions R_i is performed as in [12], resulting in eq. (2.23) and eq. (2.24), where a_i and d_i are the coefficients for the formulation combination, which can be consulted in Table 2.1 for the widespread combinations.

$$a_1 \frac{1}{\eta_1}\text{T-EFIE}_2 + a_2 \frac{1}{\eta_2}\text{T-EFIE}_2 \tag{2.23}$$

$$d_1\eta_1\text{T-MFIE}_1 + d_2\eta_2\text{T-MFIE}_2 \tag{2.24}$$

Once the tangential integral equations have been developed, the next step is their discretization, for which will be used the procedure shown in section 2.1. For this, $\mathbf{J}$ and $\mathbf{M}$ currents are expanded using eq. (2.2), where α_n are complex unknown coefficients. Developing the rest of process for eq. (2.19) and eq. (2.20) and ordering taking into account the linearity of the operators we arrive to eq. (2.25) and eq. (2.26), where J_n and M_m are the expanded $\mathbf{J}$ and $\mathbf{M}$ currents and $m = 1 \dots N$.

$$\begin{aligned}\text{T-EFIE}_{12} : a_1 \sum_{n=1}^{N} \langle \mathbf{f}_m, \mathcal{L}_1(\mathbf{f}_n)\rangle \, J_n - \frac{a_1}{\eta_1} \sum_{n=1}^{N} \langle \mathbf{f}_m, \mathcal{K}_1(\mathbf{f}_n)\rangle \, M_n \\ + a_2 \sum_{n=1}^{N} \langle \mathbf{f}_m, \mathcal{L}_2(\mathbf{f}_n)\rangle \, J_n - \frac{a_2}{\eta_2} \sum_{n=1}^{N} \langle \mathbf{f}_m, \mathcal{K}_2(\mathbf{f}_n)\rangle \, M_n \\ + \frac{1}{2}\left(\frac{a_1}{\eta_1} - \frac{a_2}{\eta_2}\right) \sum_{n=1}^{N} \langle \mathbf{f}_m, \widehat{\mathbf{n}} \times \mathbf{f}_n\rangle M_n \\ = \left\langle \mathbf{f}_m, a_1 \frac{1}{\eta_1} \mathbf{E}_1^i - a_2 \frac{1}{\eta_2} \mathbf{E}_2^i \right\rangle \end{aligned} \tag{2.25}$$

$$\begin{aligned}\text{T-MFIE}_{12} : d_1\eta_1 \sum_{n=1}^{N} \langle \mathbf{f}_m, \mathcal{K}_1(\mathbf{f}_n)\rangle \, J_n + d_1 \sum_{n=1}^{N} \langle \mathbf{f}_m, \mathcal{L}_1(\mathbf{f}_n)\rangle \, M_n \\ + d_2\eta_2 \sum_{n=1}^{N} \langle \mathbf{f}_m, \mathcal{K}_2(\mathbf{f}_n)\rangle \, J_n + d_2 \sum_{n=1}^{N} \langle \mathbf{f}_m, \mathcal{L}_2(\mathbf{f}_n)\rangle \, M_n \\ + \frac{1}{2}\left(d_2\eta_2 - d_1\eta_1\right) \sum_{n=1}^{N} \langle \mathbf{f}_m, \widehat{\mathbf{n}} \times \mathbf{f}_n\rangle J_n \\ = \left\langle \mathbf{f}_m, d_1\eta_1 \mathbf{H}_1^i - d_2\eta_2 \mathbf{H}_2^i \right\rangle \end{aligned} \tag{2.26}$$

2.2.2 Normal formulation

The approach to develop the normal surface integral equations for electric and magnetic fields is the same described in 2.2.1, but departing from the rotated tagential component of the fields in R_i over S. This gives place to eq. (2.27) and eq. (2.28). Notice that its called *normal formulation* because the product by $\widehat{\mathbf{n}}_i$ appears explicitly, but, despite this, the boundary conditions are still the the tangential fields, rotated in this case.

$$\text{N-EFIE}_i : \widehat{\mathbf{n}}_i \times (\eta_i \mathcal{L}_i(\mathbf{J}_i) - \mathcal{K}_i^{PV}(\mathbf{M}_i)) - \frac{1}{2}\mathbf{M}_i = \widehat{\mathbf{n}}_i \times \mathbf{E}_i^i \tag{2.27}$$

$$\text{N-MFIE}_i : \widehat{\mathbf{n}}_i \times (\mathcal{K}_i^{PV}(\mathbf{J}_i) + \frac{1}{\eta_i}\mathcal{L}_i(\mathbf{M}_i)) + \frac{1}{2}\mathbf{J}_i = \widehat{\mathbf{n}}_i \times \mathbf{H}_i^i \tag{2.28}$$

Applying the formulation of [12], in a similar way as done in eq. (2.23) and eq. (2.24), we obtain eq. (2.29) and eq. (2.30).

$$b_1 \text{N-MFIE}_1 + b_2 \text{N-MFIE}_2 \tag{2.29}$$

$$-c_1\text{N-EFIE}_1 - c_2\text{N-EFIE}_2 \tag{2.30}$$

By developing eq. (2.29) and eq. (2.30) as done with eq. (2.23) and eq. (2.24) in 2.2.1 we arrive to the complete expressions for both equations, as shown in eq. (2.31) and eq. (2.32).

$$\begin{aligned}\text{N-MFIE}_{12} : b_1 \sum_{n=1}^{N} \left\langle \mathbf{f}_m, \widehat{\mathbf{n}} \times \mathcal{K}_1^{PV}(\mathbf{f}_n) \right\rangle J_n - \frac{b_1}{\eta_1} \sum_{n=1}^{N} \langle \mathbf{f}_m, \widehat{\mathbf{n}} \times \mathcal{L}_1(\mathbf{f}_n) \rangle M_n \\ -b_2 \sum_{n=1}^{N} \left\langle \mathbf{f}_m, \widehat{\mathbf{n}} \times \mathcal{K}_2^{PV}(\mathbf{f}_n) \right\rangle J_n - \frac{b_2}{\eta_2} \sum_{n=1}^{N} \langle \mathbf{f}_m, \widehat{\mathbf{n}} \times \mathcal{L}_2(\mathbf{f}_n) \rangle M_n \\ + \frac{1}{2}(b_1 + b_2) \sum_{n=1}^{N} \langle \mathbf{f}_m, \mathbf{f}_n \rangle J_n \\ = \left\langle \mathbf{f}_m, b_1(\widehat{\mathbf{n}} \times \mathbf{H}_1^i) + b_2(\widehat{\mathbf{n}} \times \mathbf{H}_2^i) \right\rangle\end{aligned} \tag{2.31}$$

$$\begin{aligned}\text{N-EFIE}_{12} : -c_1\eta_1 \sum_{n=1}^{N} \langle \mathbf{f}_m, \widehat{\mathbf{n}} \times \mathcal{L}_1(\mathbf{f}_n) \rangle J_n + c_1 \sum_{n=1}^{N} \left\langle \mathbf{f}_m, \widehat{\mathbf{n}} \times \mathcal{K}_1^{PV}(\mathbf{f}_n) \right\rangle M_n \\ +c_2\eta_2 \sum_{n=1}^{N} \langle \mathbf{f}_m, \widehat{\mathbf{n}} \times \mathcal{L}_2(\mathbf{f}_n) \rangle J_n - c_2 \sum_{n=1}^{N} \left\langle \mathbf{f}_m, \widehat{\mathbf{n}} \times \mathcal{K}_2^{PV}(\mathbf{f}_n) \right\rangle M_n \\ + \frac{1}{2}(c_1 + c_2) \sum_{n=1}^{N} \langle \mathbf{f}_m, \mathbf{f}_n \rangle M_n \\ = \left\langle \mathbf{f}_m, -c_1(\widehat{\mathbf{n}} \times \mathbf{E}_1^i) - c_2(\widehat{\mathbf{n}} \times \mathbf{E}_2^i) \right\rangle\end{aligned} \tag{2.32}$$

2.2.3 Combined formulation

The tangential and normal formulations are capable of solving any penetrable problem. However, each of them has some particular problems like stability or precision, as was studied in [13] through the application of CTF (*combined tangential formulation*) and CNF (*combined normal formulation*). In order to compensate those problems, a weighted combination of both formulations can be performed [12], as shown in eq. (2.33), where $i = 1$ is external part of the surface $S$and $i = 2$ the internal part.

$$\sum_{i=1}^{2} \frac{a_i}{\eta_i} \text{T-EFIE}_i + \sum_{i=1}^{2} b_i \text{N-MFIE}_i \tag{2.33}$$

$$- \sum_{i=1}^{2} c_i \text{N-EFIE}_i + \sum_{i=1}^{2} d_i \eta_i \text{T-MFIE}_i, \tag{2.34}$$

Equation (2.33) is called electric current (J) combined field integral equation (JCFIE), and perfect electric conductors (PEC) can be analyzed through it weighting by zero the inner region. On the other hand, eq. (2.33) describes the magnetic current (M) combined field integral equation (MCFIE). The most widespread combination of the equations above are shown in Table 2.1, where PMCHWT stands for Poggio-Miller-Chang-Harrington-Wu-Tsai [14].

Formulación	a_i	b_i	c_i	d_i
JMCFIE	1	1	1	1
CTF	1	0	0	1
PMCHWT	η_i	0	0	$1/\eta_i$
CNF	0	1	1	0

Table 2.1: Values for the coefficients for the JMCFIE, CTF, PMCHWT and CNF formulations.

2.3 Application of the formulation to multiple penetrable objects

In this section the SIE-MoM framework is extended for multiple penetrable objects, departing from the generic scheme shown in Fig. 2.3. As in the example used in Fig. 2.1, R_i is the region or medium with constitutive parameters ϵ_i and μ_i. The interface between regions R_i and R_j is denoted as S_{ij} meeting $i < j$, and the normal unit vector pointing to region R_i is denoted as $\widehat{\mathbf{n}}_{ij}$.

Applying the equivalence theorem, every interface is replaced by equivalent electric $\mathbf{J}_{ij}$ and magnetic $\mathbf{M}_{ij}$ currents, which are dependent of the relation shown in equations (2.35) and (2.36), where $\mathbf{E}_i^t$ and $\mathbf{H}_i^t$ are the total electric and magnetic field respectively in the region R_i.

$$\widehat{\mathbf{n}}_{ij} \times \mathbf{M}_{ij} = \mathbf{E}_i^t \tag{2.35}$$

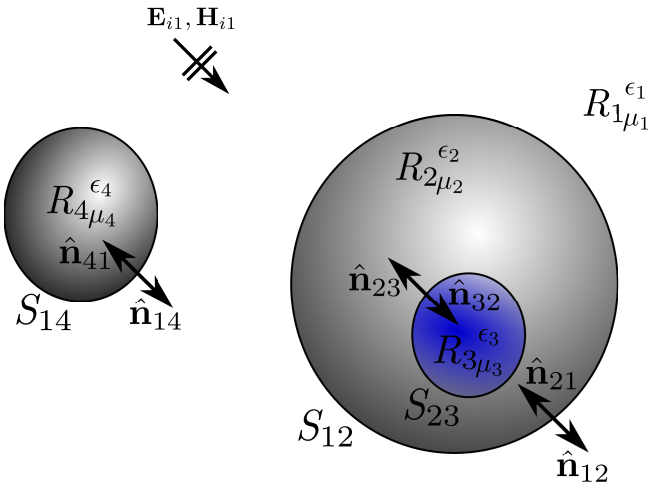

Figure 2.3: Generic example with multiple bodies used for the development of the extension of the formulation.

$$-\widehat{\mathbf{n}}_{ij} \times \mathbf{J}_{ij} = \mathbf{H}_i^t \tag{2.36}$$

The total fields in R_i can be expressed as the sum of the incident fields and the scattered fields by the surface equivalent currents, shown in equations (2.37) and (2.38), where j' is the index of the adjacent region index to R_i.

$$\mathbf{H}_i^t = \mathbf{H}_i^i + \sum_{j'} \mathbf{H}_i^s(\mathbf{J}_{ij'}\mathbf{M}_{ij'}) \tag{2.37}$$

$$\mathbf{E}_i^t = \mathbf{E}_i^i + \sum_{j'} \mathbf{E}_i^s(\mathbf{J}_{ij'}, \mathbf{M}_{ij'}) \tag{2.38}$$

The scattered fields $\mathbf{E}_i^s(\mathbf{J}_{ij'}, \mathbf{M}_{ij'})$ and $\mathbf{H}_i^s(\mathbf{J}_{ij'}, \mathbf{M}_{ij'})$ can be obtained from eq. (2.39) and eq. (2.40) respectively, where $\mathcal{L}(\cdot)$ and $\mathcal{K}(\cdot)$ are the previously defined integral operators and η_i is the intrinsic impedance of region R_i.

$$\mathbf{E}_i^s(\mathbf{J}_{ij'}, \mathbf{M}_{ij'}) = -\eta_i \mathcal{L}_i(\mathbf{J}_{ij'}) + \mathcal{K}_i(\mathbf{M}_{ij'}) \tag{2.39}$$

$$\mathbf{H}_i^s(\mathbf{J}_{ij'}, \mathbf{M}_{ij'}) = -\mathcal{K}_i(\mathbf{J}_{ij'}) - \frac{1}{\eta_i}\mathcal{L}_i(\mathbf{M}_{ij'}) \tag{2.40}$$

The equivalent currents $\mathbf{J}_{ij}$ and $\mathbf{M}_{ij}$ over S_{ij} can be computed based on the total fields over it, as shown in eq. (2.41) and eq (2.42), being $\mathbf{E}_i^t|_{S_{ij}}$ and $\mathbf{H}_i^t|_{S_{ij}}$ the total electric and magnetic fields in the region R_i. Both equations describe the EFIE and the MFIE within region R_i.

$$\text{EFIE}_i|_{S_{ij}} : \mathbf{M}_{ij} = -\widehat{\mathbf{n}}_{ij} \times \mathbf{E}_i^t|_{S_{ij}} \tag{2.41}$$
$$\text{MFIE}_i|_{S_{ij}} : \mathbf{J}_{ij} = \widehat{\mathbf{n}}_{ij} \times \mathbf{H}_i^t|_{S_{ij}} \tag{2.42}$$

By following a similar process as described previously in 2.2.1 and 2.2.2, we can obtain the set of surface integral equations for both the tangential and the normal fields. The result of this process is shown in equations (2.43), (2.44), (2.45) and (2.46).

$$\text{T-EFIE}_i|_{S_{ij}} : \widehat{\mathbf{n}}_{ij} \times \mathbf{M}_{ij} + \sum_{j'} \Big((\eta_i \mathcal{L}_i(\mathbf{J}_{ij'}) - \mathcal{K}_i^{PV}(\mathbf{M}_{ij'}))_{tan} - \frac{1}{2}\widehat{\mathbf{n}}_{ij} \times \mathbf{M}_{ij'} \Big) = \mathbf{E}_{i,tan}^i \tag{2.43}$$

$$\text{T-MFIE}_i|_{S_{ij}} : -\widehat{\mathbf{n}}_{ij} \times \mathbf{J}_{ij} + \sum_{j'} \left((\mathcal{K}_i^{PV}(\mathbf{J}_{ij'}) + \frac{1}{\eta_i}\mathcal{L}_i(\mathbf{M}_{ij'}))_{tan} + \frac{1}{2}\widehat{\mathbf{n}}_{ij} \times \mathbf{J}_{ij'} \right) = \mathbf{H}_{i,tan}^i \tag{2.44}$$

$$\text{N-EFIE}_i|_{S_{ij}} : -\mathbf{M}_{ij'} + \widehat{\mathbf{n}}_{ij} \times \sum_{j'} \Big(\eta_i \mathcal{L}_i(\mathbf{J}_{ij'}) - \mathcal{K}_i^{PV}(\mathbf{M}_{ij'}) - \frac{1}{2}\widehat{\mathbf{n}}_{ij} \times \mathbf{M}_{ij'} \Big) = \widehat{\mathbf{n}}_{ij} \times \mathbf{E}_i^i \tag{2.45}$$

$$\text{N-MFIE}_i|_{S_{ij}} : \mathbf{J}_{ij} + \widehat{\mathbf{n}}_{ij} \times \sum_{j'} \left(\mathcal{K}_i^{PV}(\mathbf{J}_{ij'}) + \frac{1}{\eta_i}\mathcal{L}_i(\mathbf{M}_{ij'}) + \frac{1}{2}\widehat{\mathbf{n}}_{ij} \times \mathbf{J}_{ij'} \right) = \widehat{\mathbf{n}}_{ij} \times \mathbf{H}_i^i \tag{2.46}$$

This set of integral equations can be gathered as shown in eq. (2.47) and eq. (2.48), where the parameters a_i, b_i, c_i and d_i can be found in Table 2.1.

$$\text{JCFIE}_i|_{S_{ij}} \quad = \quad a_i \frac{1}{\eta_i} \text{T-EFIE}_i + b_i \text{N-MFIE}_i \tag{2.47}$$

$$\text{MCFIE}_i|_{S_{ij}} \quad = \quad -c_i\text{N-EFIE}_i + d_i\eta_i\text{T-MFIE}_i \tag{2.48}$$

The last step is combining the JCFIE and MCFIE of the regions R_i y R_j in order to obtain the SIE over S_{ij}, as shown in equations. (2.49) and (2.50).

$$\begin{aligned}
\text{JCFIE}_{ij} : a_i \sum_{j'} \left(\eta_i \mathcal{L}_i(\mathbf{J}_{ij'}) - \frac{1}{\eta_i}\mathcal{K}_i^{PV}(\mathbf{M}_{ij'}) \right)_{tan} \\
+a_j \sum_{j'} \left(\eta_j \mathcal{L}_j(\mathbf{J}_{jj'}) - \frac{1}{\eta_j}\mathcal{K}_i^{PV}(\mathbf{M}_{jj'}) \right)_{tan} \\
+b_i\widehat{\mathbf{n}}_{ij} \times \sum_{j'} \left(\mathcal{K}_i^{PV}(\mathbf{J}_{ij'}) + \frac{1}{\eta_i}\mathcal{L}_i(\mathbf{M}_{ij'}) \right) \\
+b_j\widehat{\mathbf{n}}_{ji} \times \sum_{j'} \left(\mathcal{K}_j^{PV}(\mathbf{J}_{jj'}) + \frac{1}{\eta_j}\mathcal{L}_j(\mathbf{M}_{jj'}) \right) \\
+\frac{1}{2}\left(\frac{a_i}{\eta_i}\widehat{\mathbf{n}}_{ij} \times \mathbf{M}_{ij} + \frac{a_j}{\eta_i}\widehat{\mathbf{n}}_{ji} \times \mathbf{M}_{ji} + b_i\mathbf{J}_{ij} + b_j\mathbf{J}_{ji} \right) \\
= a_i \left(\mathbf{E}^i_{i,tan}\right) + a_j \left(\mathbf{E}^j_{j,tan}\right) + \widehat{\mathbf{n}}_{ij} \times \mathbf{H}^i_i + \widehat{\mathbf{n}}_{ji} \times \mathbf{H}^i_j
\end{aligned} \tag{2.49}$$

$$\begin{aligned}
\text{MCFIE}_{ij} : -c_i\widehat{\mathbf{n}}_{ij} \times \sum_{j'} \left(\eta_i \mathcal{L}_i(\mathbf{J}_{ij'}) - \mathcal{K}_i^{PV}(\mathbf{M}_{ij'}) \right) \\
-c_j\widehat{\mathbf{n}}_{ji} \times \sum_{j'} \left(\eta_j \mathcal{L}_j(\mathbf{J}_{jj'}) - \mathcal{K}_j^{PV}(\mathbf{M}_{jj'}) \right) \\
+d_i \sum_{j'} \left(\eta_i \mathcal{K}_i^{PV}(\mathbf{J}_{ij'}) + \mathcal{L}_i(\mathbf{M}_{ij'}) \right)_{tan} \\
+d_j \sum_{j'} \left(\eta_j \mathcal{K}_j^{PV}(\mathbf{J}_{jj'}) + \mathcal{L}_j(\mathbf{M}_{jj'}) \right)_{tan} \\
+\frac{1}{2}\left(c_i\mathbf{M}_{ij} + c_j\mathbf{M}_{ji} - d_i\widehat{\mathbf{n}}_{ij} \times \mathbf{J}_{ij} - d_j\widehat{\mathbf{n}}_{ji} \times \mathbf{J}_{ji} \right) \\
= c_i\widehat{\mathbf{n}}_{ij} \times \mathbf{E}^i_i + c_i\widehat{\mathbf{n}}_{ji} \times \mathbf{E}^i_j + d_i\eta_i\mathbf{H}^i_{i,tan} + d_j\eta_j\mathbf{H}^i_{i,tan}
\end{aligned} \tag{2.50}$$

If we gather the expressions (2.49) and (2.50) by interfaces and apply matrix notation, it can be expressed as shown in eq. (2.51).

$$\begin{bmatrix} \mathbf{Z}_{ij,ij} & \mathbf{Z}_{ij,kl} & \cdots & \mathbf{Z}_{ij,pq} \\ \mathbf{Z}_{kl,ij} & \mathbf{Z}_{kl,kl} & \cdots & \mathbf{Z}_{kl,pq} \\ \vdots & \vdots & \ddots & \vdots \\ \mathbf{Z}_{pq,ij} & \mathbf{Z}_{pq,kl} & \cdots & \mathbf{Z}_{pq,pq} \end{bmatrix} \begin{bmatrix} \boldsymbol{I}_{ij} \\ \boldsymbol{I}_{kl} \\ \vdots \\ \boldsymbol{I}_{pq} \end{bmatrix} = \begin{bmatrix} \boldsymbol{V}_{ij} \\ \boldsymbol{V}_{kl} \\ \vdots \\ \boldsymbol{V}_{pq} \end{bmatrix} \tag{2.51}$$

In this expression, each sub-block $\mathbf{Z}_{ij,i'j'}$ corresponds to the coupling of interface $S_{i'j'}$ over S_{ij}, and are defined as in eq. (2.52), where vectors $\boldsymbol{I}_{ij}$ and $\boldsymbol{V}_{ij}$ are defined in (2.53), being $\boldsymbol{J}_{ij}[n] = J_n$ and $\boldsymbol{M}_{ij}[n] = M_n$. Notice that when there is no shared medium between interface, all the elements of the coupling sub-block between them are equal to zero, as is usual in many CEM problems.

$$\mathbf{Z}_{ij,i'j'} = \begin{bmatrix} \mathbf{Z}^{1J}_{ij,i'j'} & \mathbf{Z}^{1M}_{ij,i'j'} \\ \mathbf{Z}^{2J}_{ij,i'j'} & \mathbf{Z}^{2M}_{ij,i'j'} \end{bmatrix} \tag{2.52}$$

$$\boldsymbol{I}_{ij} = \begin{bmatrix} \boldsymbol{J}_{ij} \\ \boldsymbol{M}_{ij} \end{bmatrix}; \boldsymbol{V}_{ij} = \begin{bmatrix} \boldsymbol{V}^1_{ij} \\ \boldsymbol{V}^2_{ij} \end{bmatrix} \tag{2.53}$$

Expressions (2.54) and (2.55) show the definition of $\boldsymbol{V}^1_{ij}$ and $\boldsymbol{V}^2_{ij}$, where $b_m = \langle \mathbf{f}_m, \frac{a_1}{\eta_1}\mathbf{E}^i_1 - \frac{a_2}{\eta_2}\mathbf{E}^i_2 \rangle$ and $c_m = \langle \mathbf{f}_m, d_1\eta_1\mathbf{H}^i_1 - d_2\eta_2\mathbf{H}^i_2 \rangle$.

$$\boldsymbol{V}^1_{ij} = b^{ij}_m + b'^{ij}_m \tag{2.54}$$

$$\boldsymbol{V}^2_{ij} = c^{ij}_m + c'^{ij}_m \tag{2.55}$$

Chapter 3

Efficient analysis of finite periodic structures

Contenido

3.1 Introduction 22

3.2 SlotFFT Algorithm 23

3.2.1 Single sampling SlotFFT approach 24

3.2.2 Double sampling SlotFFT approach 30

3.3 Application to finite periodic structures 33

3.4 Extension to aperiodic element-wise materials structures 41

3.5 Extension to roughly finite periodic structures 43

3.5.1 Validation and application 46

This chapter focuses on the efficient analysis of periodic structures. The first section introduces the problems that appear when CEM analysis is carried for this kind of structures, followed by a review of the most relevant techniques used to tackle periodic problems. In section two slotFFT algorithm, the core method developed in this thesis, is introduced. Single and double sampling formulations of the algorithm are developed, including a mean computing time of the MVP comparisons for the straight approach and for both versions of the algorithm. The third section shows the remarkable results obtained used this method, from the first results obtained at the beginning of the thesis to a replicated case with biomedical applications. The fourth and fifth sections introduce two extensions of slotFFT for especial cases in the limits of the thesis.

3.1 Introduction

Computational electromagnetic analysis is a vast field of research with many topics. From the ships and planes communication systems or the modern 5G antennas to the cutting-edge applications of electromagnetism within biotechnology, even in the now not-so-science fiction apps of metamatelaries like invisibility, periodic structures are very common. Periodic structures present many interesting properties with a vast plethora of applications: they can be frequency selective, achieve chiral behavior, achieve extreme field concentrations or allow special radiation patterns, to mention few examples.

However, when it comes to CEM, periodic structures become a major issue. The large size of the structures combined with the large number of elements that compose them and the mesh densities to properly analyze the problems give place to prohibitive computational needs. In terms of memory, it is easy to pose impedance matrix with few hundreds of gigabytes of RAM memory, making the analysis impossible without specific computational infrastructure that is not available for everyone. At the same time, the extreme number of unknowns that composes the problems is also translated into a large number of operations to attain the solution, hence very long computational times even with iterative methods like generalized minimal residual method (GMRES). As a response to these kind problems, several methods are available to perform the CEM analysis.

The Floquet's harmonic theory [15–19] is based on expansion series, intended for compute the electromagnetic behavior of infinite arrays. However, most of the real world systems cannot be approximated as infinite structures. Due to this inconvenient, there are Floquet based methods capable of approach finite periodic structures. This comes with a cost, as the approximation does not properly take inot account important effects like stationary waves or edge-effects, which are relevant in the system response.

Despite its complexity to implement, the multilevel fast miltipole algorithm (MLFMA) [20–29] is a widespread method to approach finite periodic problems due to its high efficiency. It is based on the discretization of the surface integral equations and for solving problems uses iterative solvers as well as it integrates other methods to achieve higher accelerations of the solving stage. In order to accelerate the MVP, the MLFMA relies on a multipolar expansion of the Green's function, and performs the aggregation, translation and dissaggregation processes, which limit the precision attainable. This precision limit depends on parameters like the number of multipoles that make the computational cost to scale but allowing to get closer the the precision of SIE-MoM. Due to its implementation, the MLFMA achieves a high efficiency, with an equivalent cost of $\mathcal{O}(N\log(N))$ (where N is the problem number of unknowns). In addition to this, the MLFMA does not take advantage of the periodicity of the problem, as is

intended for arbitrary geometries.

Another approach, intended for the fast computation of the MVP, is the precorrected fast Fourier transform (p-FFT) [30–35]. The p-FFT method performs the transformation of a general problem into an uniform three dimension grid scheme and computes in a different way the near and the far couplings. By carry out this, the result must pass through a precorrection stage in order to compensate precision losses. The CG-FFT method [36] is a similar procedure also intended for accelerating a three dimensional uniform grid using the FFT.

Besides the applications of the FFT in non periodic problems, it has been applied for some kind of specific periodic problems without any precision loss. Some particular antenna arrays present a multilevel block-Toeplitz impedance matrix when solve using MoM, which allow the application of the FFT to accelerate the solving process [37–39]. The FFT based approach proposed in [40, 41] offers a fast solver for antenna array, whereas the techniques proposed in [37–41] approach the periodicity of the composites, achieving in both cases an acceleration without precision loss.

At last, a different approach has been applied to greatly simplify ensembles of elements that are periodic or that present some kind of periodicity in three dimensions for both cases. The homogeneization methods [42, 43] builds an equivalent problem, creating a body with shape similar to the original problem which encloses it. By calculating specific constitutive properties for the equivalent problem, these methods greatly reduce the number of unknowns that compose it, but at the cost of precision in the solution obtained.

3.2 SlotFFT Algorithm

When dealing with finite periodic problems using the SIE-MoM, the periodical patterns of the structures are translated into the impedance matrix. This can be appreciated in Fig. 3.1, where the impedance matrix of a linear array of three elements is shown using a logarithmic representation to magnify the patterns. In particular, part of the self-coupling sub-matrix are remarked in order to ease the appreciation.

Though the extraction of set of elements from the MoM impedance matrix by sampling it, the MVP can be carried out with a low number of operations using the FFT in comparison with the straight MVP. We have named this new approach *slotFFT algorithm*.

This section introduces two different versions of this algorithm, as it evolved during

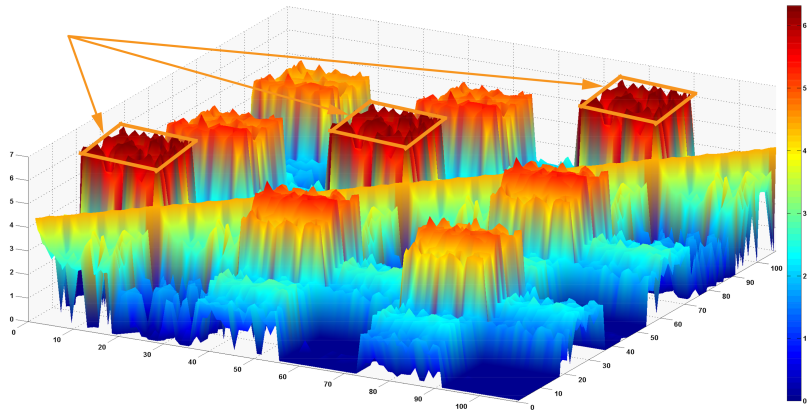

Figure 3.1: Logarithmic representation of an impedance matrix of the periodic linear array with periodic features remarked.

the development of this thesis. The first version of slotFFT [44] performs a single sampling of the MoM impedance matrix, hence the name, whereas the second version perform a double sampling, increasing considerably the efficiency attainable in the MVP.

3.2.1 Single sampling SlotFFT approach

For the sake of simplicity, the formulation is only introduced for 1D arrays. A generic linear array of M elements is considered, shown in Fig. 3.2, where every element of the array is identically described with RWG basis functions, giving place to n unknowns per element and a total number of unknown of N for the whole problem, being $N = nM$.

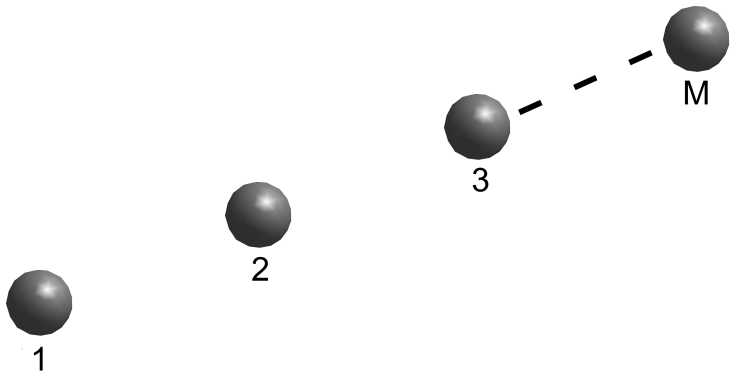

Figure 3.2: Generic periodic linear array with M bodies.

The generic impedance matrix of a problem of this nature is shown in eq. (3.1),

where submatrix $\mathbf{Z}_{i,j}$ contains $n \times n$ coefficients which describe the coupling between of the source basis functions of element j over the test basis functions of element i.

$$\mathbf{Z} = \left\{ \begin{array}{cccccc} \mathbf{Z}_{1,1} & \mathbf{Z}_{1,2} & \mathbf{Z}_{1,3} & \mathbf{Z}_{1,4} & \cdots & \mathbf{Z}_{1,M} \\ \mathbf{Z}_{2,1} & \mathbf{Z}_{2,2} & \mathbf{Z}_{2,3} & \mathbf{Z}_{2,4} & \cdots & \mathbf{Z}_{2,M} \\ \mathbf{Z}_{3,1} & \mathbf{Z}_{3,2} & \mathbf{Z}_{3,3} & \mathbf{Z}_{3,4} & \cdots & \mathbf{Z}_{3,M} \\ \vdots & \vdots & \vdots & \vdots & \ddots & \vdots \\ \mathbf{Z}_{M,1} & \mathbf{Z}_{M,2} & \mathbf{Z}_{M,3} & \mathbf{Z}_{M,4} & \cdots & \mathbf{Z}_{M,M} \end{array} \right\}_{\{N \times N\}} , \tag{3.1}$$

As all the elements of the array are identically discretized, and taking into account the symmetries between identical relative positions, we can set the identities shown in equations (3.2)-(3.4).

$$\mathbf{Z}_{i,i} = \mathbf{Z}_{1,1} \tag{3.2}$$

$$\mathbf{Z}_{i,j} = \mathbf{Z}_{1,j-i+1} \quad \text{if} \quad j > i \tag{3.3}$$

$$\mathbf{Z}_{i,j} = \mathbf{Z}_{i-j+1,1} \quad \text{if} \quad j < i \tag{3.4}$$

Introducing eqs. (3.2)-(3.4) into eq. (3.1), we can see that $\mathbf{Z}$ presents the structure of a *block Toeplitz Matrix*, as shown in eq. (3.5).

$$\mathbf{Z} = \left\{ \begin{array}{cccccc} \mathbf{Z}_{1,1} & \mathbf{Z}_{1,2} & \mathbf{Z}_{1,3} & \mathbf{Z}_{1,4} & \cdots & \mathbf{Z}_{1,M} \\ \mathbf{Z}_{2,1} & \mathbf{Z}_{1,1} & \mathbf{Z}_{1,2} & \mathbf{Z}_{1,3} & \cdots & \mathbf{Z}_{1,M-1} \\ \mathbf{Z}_{3,1} & \mathbf{Z}_{2,1} & \mathbf{Z}_{1,1} & \mathbf{Z}_{1,2} & \cdots & \mathbf{Z}_{1,M-1} \\ \vdots & \vdots & \vdots & \vdots & \ddots & \vdots \\ \mathbf{Z}_{M,1} & \mathbf{Z}_{M-1,1} & \mathbf{Z}_{M-2,1} & \mathbf{Z}_{M-3,1} & \cdots & \mathbf{Z}_{1,1} \end{array} \right\}_{\{N \times N\}} \tag{3.5}$$

In order to simplify the expressions we can set $\mathbf{Z}^k$ as stated in eq. (3.6).

$$\mathbf{Z}^k \equiv \mathbf{Z}_{i,j} \qquad \text{where} \qquad k = j - i, \qquad -M + 1 < k < M - 1 \tag{3.6}$$

By replacing eq. (3.6) into eqs. (3.2)-(3.4) the expressions can be written as in eqs.(3.8)-(3.9) .

$$\mathbf{Z}^0 \equiv \mathbf{Z}_{1,1} \tag{3.7}$$

$$\mathbf{Z}^{j-i} \equiv \mathbf{Z}_{1,j-i+1} \quad \text{if} \quad j > i \tag{3.8}$$

$$\mathbf{Z}^{j-i} = \mathbf{Z}^{-(i-j)} \equiv \mathbf{Z}_{i-j+1,1} \quad \text{if} \quad j < i \tag{3.9}$$

If we apply these set of equations to eq. (3.5), we can express $\mathbf{Z}$ as shown in eq. (3.10).

$$\mathbf{Z} = \left\{ \begin{array}{cccccc} \mathbf{Z}^0 & \mathbf{Z}^1 & \mathbf{Z}^2 & \mathbf{Z}^3 & \cdots & \mathbf{Z}^{M-1} \\ \mathbf{Z}^{-1} & \mathbf{Z}^0 & \mathbf{Z}^1 & \mathbf{Z}^2 & \cdots & \mathbf{Z}^{M-2} \\ \mathbf{Z}^{-2} & \mathbf{Z}^{-1} & \mathbf{Z}^0 & \mathbf{Z}^1 & \cdots & \mathbf{Z}^{M-3} \\ \vdots & \vdots & \vdots & \vdots & \ddots & \vdots \\ \mathbf{Z}^{-(M-1)} & \mathbf{Z}^{-(M-2)} & \mathbf{Z}^{-(M-3)} & \mathbf{Z}^{-(M-4)} & \cdots & \mathbf{Z}^0 \end{array} \right\}_{\{N \times N\}} \tag{3.10}$$

From this expression the similitude with a *Toeplitz matrix* can be quickly appreciated. If that were the case, the MVP of $\mathbf{Z}$ with a vector could be computed in an efficient way using the FFT, reducing the cost of the MVP from $\mathcal{O}(N^2)$ to $\mathcal{O}(N \log N)$. However, $\mathbf{Z}$ is a *block-Toeplitz matrix*, which makes necessary the application of a process to decompose $\mathbf{Z}$ in a set of sub-matrix able to be compute through the stated procedure using FFT, being this process of decomposition the core of the slotFFT method.

To model each one of the block rows in eq. (3.10) using the notation introduced in eq. (3.6), a block row matrix R_i of $n \times N$ elements can be posed, meeting the expression in eq. (3.11).

$$\mathbf{R}_i \equiv \left\{ \begin{array}{cccc} \mathbf{Z}^{1-i} & \mathbf{Z}^{2-i} & \mathbf{Z}^{3-i} & \cdots \quad \mathbf{Z}^{M-i} \end{array} \right\} \qquad 0 < i \leq M \tag{3.11}$$

Replacing in $\mathbf{Z}$ the sets of block row matrix, it can be expressed as in eq. (3.12).

$$\mathbf{Z} = \left\{ \begin{array}{c} \mathbf{R}_1 \\ \mathbf{R}_2 \\ \mathbf{R}_3 \\ \vdots \\ \mathbf{R}_M \end{array} \right\}_{\{N \times N\}} \tag{3.12}$$

From this, a special matrix $\mathbf{R}$ of $n \times (2N-n)$ elements can be posed, that contains all the unique elements in $\mathbf{Z}$, as shown in eq. (3.13). As it is written, it can be appreciated that each $\mathbf{R}_i$ can be extracted from $\mathbf{R}$.

$$\mathbf{R} \equiv \left\{ \begin{array}{cccccccccc} \mathbf{Z}^{-(M-1)} & \mathbf{Z}^{-(M-2)} & \cdots & \mathbf{Z}^{-1} & \mathbf{Z}^{0} & \mathbf{Z}^{1} & \mathbf{Z}^{2} & \cdots & \mathbf{Z}^{M-1} \end{array} \right\} \tag{3.13}$$

All $\mathbf{R}_i$ can be extracted from $\mathbf{R}$, meeting $0 < i \leq M$, taking the columns from $N - in + 1$ to $2N - in$. Using MatLab notation this can be performed through the expression $R_i = R(:, (N - in + 1) : (2N - in))$.

Departing from eq. (3.13) a matrix $\mathcal{Z}_k$ $N \times N$ can be expressed as shown in eq. (3.14), where $0 < k \leq n$. In general $i - j - k + N + 1$ are greater than 0. However, there will be too few elements out of the range of $\mathbf{R}$. These elements can be filled with any value. Notice that this can be done because due to the way slotFFT approach the MVP in its final stage, these elements do not introduce any effect into the solution.

$$\{\mathcal{Z}_k\}_{i,j} \equiv \{\mathbf{R}\}_{k,i-j-k+N+1} \tag{3.14}$$

It can be appreciated that every $k + in$ row of $\mathcal{Z}_k$ corresponds to the same $k + in$ row of $\mathbf{Z}$, as shown in eq. (3.15). Furthermore, each row of $\mathcal{Z}_k$ can be obtained by shifting the precedent row, as shown in eq. (3.16), which implies that each $\mathcal{Z}_k$ is a Toeplitz matrix.

$$\{\mathcal{Z}_k\}_{k+in,j} = \{\mathbf{Z}\{_{k+in,j} \qquad 0 \leq i < M, 1 \leq j \leq N \tag{3.15}$$

$$\{\mathcal{Z}_k\}_{i,j} = \{\mathcal{Z}_k\}_{i-1,j-1} \qquad 1 < i, j \leq N \tag{3.16}$$

We define $\mathbf{S}_k$, which will be named the *sampling matrix*, whose elements $\{S\}_k$ can be seen in eq. (3.17), where $\dot{n}$ is a multiple of n.

$$\{S_k\}_{i,j} = \left\{ \begin{array}{lll} 1 & \text{if} \quad i = j \quad \text{and} \quad i = k + \dot{n} \\ 0 & \text{elsewhere} \end{array} \right\} \tag{3.17}$$

This matrix presents a diagonal composed by ones with a periodic distribution dependent on M. An example for $M = 3$, $n = 3$ and $k = 2$ can be found in eq. (3.18). Also the properties shown bellow eq. (3.18) can be defined.

$$\begin{pmatrix} 0 & 0 & 0 & 0 & 0 & 0 & 0 & 0 & 0 \\ 0 & 1 & 0 & 0 & 0 & 0 & 0 & 0 & 0 \\ 0 & 0 & 0 & 0 & 0 & 0 & 0 & 0 & 0 \\ 0 & 0 & 0 & 0 & 0 & 0 & 0 & 0 & 0 \\ 0 & 0 & 0 & 0 & 1 & 0 & 0 & 0 & 0 \\ 0 & 0 & 0 & 0 & 0 & 0 & 0 & 0 & 0 \\ 0 & 0 & 0 & 0 & 0 & 0 & 0 & 0 & 0 \\ 0 & 0 & 0 & 0 & 0 & 0 & 0 & 1 & 0 \\ 0 & 0 & 0 & 0 & 0 & 0 & 0 & 0 & 0 \end{pmatrix} \tag{3.18}$$

- Product of two sampling matrix:

$$\mathbf{S}_k \mathbf{S}_l = \begin{cases} \mathbf{S}_k & k = l \\ 0_{N \times N} & k \neq l \end{cases} \tag{3.19}$$

- The sum of the complete set of $\mathbf{S}_k$ is the identity matrix:

$$\mathbf{I} = \sum_{k=1}^{n} \mathbf{S}_k \tag{3.20}$$

  Then, any matrix $\mathbf{A}$ can be written as:

$$\mathbf{A} = I\mathbf{A} = \sum_{k=1}^{n} \mathbf{S}_k \mathbf{A} \tag{3.21}$$

- The $\mathbf{S}_k$ operator gives the same result when it is applied to $\mathbf{Z}$ and to $\mathcal{Z}_k$:

$$\mathbf{S}_k \mathbf{Z} = \mathbf{S}_k \mathcal{Z}_k \tag{3.22}$$

Summing over k in Eq. (3.22) we obtain the expression shown in eq. (3.23).

$$\sum_{k=1}^{n} \mathbf{S}_k \mathbf{Z} = \sum_{k=1}^{n} \mathbf{S}_k \mathcal{Z}_k \tag{3.23}$$

If we replace (3.21) into (3.23), $\mathbf{S}$ can be obtained from the sampled $\mathcal{Z}_k$ matrices, as shown in eq. (3.24).

$$\mathbf{Z} = \sum_{k=1}^{n} \mathbf{S}_k \mathcal{Z}_k \tag{3.24}$$

Departing from eq. (3.24), the product of the impedance matrix $\mathbf{Z}$ by a vector can be expressed as shown in eq. (3.25).

$$\mathbf{Z}x = \sum_{k=1}^{n} \left[\mathbf{S}_k \left(\mathcal{Z}_k x\right)\right] \tag{3.25}$$

The computational cost of eq. (3.25) by the MVP of $\mathcal{Z}_k x$, as the product by $\mathbf{S}_k$ has no cost due to the implementation in the codes. As stated previously, $\mathcal{Z}_k$ is a Toeplitz matrix, making possible to compute the MVP through the FFT with a cost of $\mathcal{O}(N \log N)$. As n MVP must be carried to compute all the elements, the final cost to carry out the MVP of $\mathbf{Z}x$ is $\mathcal{O}(nN \log N)$.

It must be taken into account that the $\mathcal{Z}_k$ matrices are not computed, meaning that no cost is introduced. Also, there is an important saving in terms of computation and storage in Z, as the stored matrix is R, shown in eq. (3.13), which needs $n \times (2N - n)$ elements in memory. From this, it can be appreciated that n domains the costs of the method. In Fig. 3.3 is shown the result of running the simple sampling slotFFT algorithm in a computing cluster composed by 4 Intel Xeon E7-4820 at 2.00GHz (eight cores each one, 32 cores in all), with 512GB of RAM memory. The structures used to perform the simulation are 1D, 2D and 3D periodic ensembles of gold nanospheres of radius 100nm and 180nm separation between surfaces, using 240 unknowns for each element and modifying the number of spheres, M, from just 75 to 40000. The analysis performed using as excitation an impinging planewave with $\lambda = 540$nm.

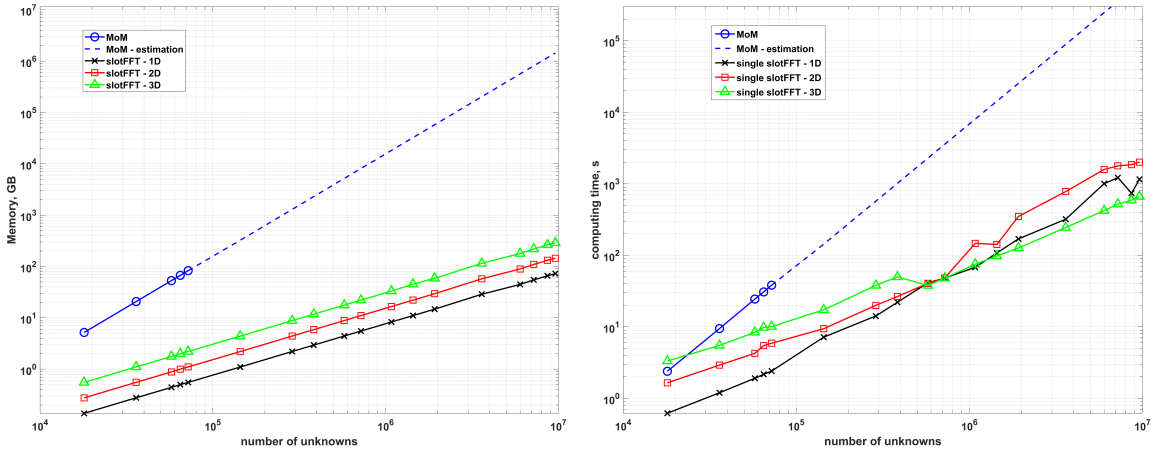

(a) Memory usage.

(b) MVP computing time.

Figure 3.3: Comparison of the memory and computing time needed with MoM and single slotFFT method for 1, 2 and 3 dimensional patterns.

Fig. 3.3(a) shows the memory cost of the storage of the MoM impedance matrix and the slotFFT using periodic structures in 1D, 2D and 3D uniform grids. As it can be expected from eq. (3.13), the needs of storage are reduced significantly. In Fig. 3.3(b) the mean MVP computing cost for the same structure is shown. The comparison of the MVP computing time was carried out without parallelization to avoid possible performance bias. The time saving derived from the reduction of the number of operations from $\mathcal{O}(N^2)$ to $\mathcal{O}(nN \log N)$ can be observed. The fluctuation in times that can be observed in the MVP mean times for slotFFT can be explained due to the different factorization of the FFT for each example. Also possible fluctuations are expectable depending on the FFT algorithm implementation.

3.2.2 Double sampling SlotFFT approach

In a similar development that in 3.2.1, this section introduces the formulation for the double sampling version of slotFFT. For this the *reduced sampling matrix* $(\overline{\mathbf{S}}_k)_{i,j}$ of $n \times nM$ elements is introduced in eq. (3.26), a sampled version of $\mathbf{S}_k$ matrix shown in eq. (3.17), with $0 < k \leq n$. Notice that the k index is used in this equation, but in the following development it will be named l or r depending the side where it is applied, as there are two sampling matrices in the development.

$$(\overline{\mathbf{S}}_k)_{i,j} = \begin{cases} 1 & for\ j = (i-1)n + k \\ 0 & otherwise \end{cases} \tag{3.26}$$

An example of this matrix is shown in eq. (3.27), in particular for a case with $n = 3$, $M = 3$ and $k = 2$.

$$\begin{pmatrix} 0 & 1 & 0 & 0 & 0 & 0 & 0 & 0 & 0 \\ 0 & 0 & 0 & 0 & 1 & 0 & 0 & 0 & 0 \\ 0 & 0 & 0 & 0 & 0 & 0 & 0 & 1 & 0 \end{pmatrix} \tag{3.27}$$

This matrix $\overline{\mathbf{S}}_k$, multiplied by its transpose, results in the sampling matrix of the same index, as shown in eq. (3.28).

$$\overline{\mathbf{S}}_k^T \overline{\mathbf{S}}_k = \mathbf{S}_k \tag{3.28}$$

Also is convenient describe other two properties as will be used in the development of the formulation. The first one, shown in eq. (3.29) (also used in the development of

the single sampling slotFFT), states that the sum of the product of a matrix $\mathbf{Z}$ by the complete set of sampling matrices results in the same matrix $\mathbf{Z}$.

$$\mathbf{Z} = \sum_{l=1}^{n} \mathbf{S}_l \mathbf{Z} \tag{3.29}$$

The second property, shown in eq. (3.30), is the extension of the first one to vectors, stating that the sum of the product of a vector x by the complete set of sampling matrices results in the same vector x.

$$x = \sum_{l=1}^{n} \mathbf{S}_l x \tag{3.30}$$

Departing from the property shown in eq. (3.29), the formulation of the problem is developed starting with eq. (3.31).

$$\mathbf{Z}x = \sum_{l=1}^{n} \mathbf{S}_l \mathbf{Z}x \tag{3.31}$$

Introducing eq. (3.30) into eq. eq. (3.31) to slot the x vector we obtain eq. (3.32).

$$\mathbf{Z}x = \sum_{l=1}^{n} \mathbf{S}_l \mathbf{Z} \left(\sum_{r=1}^{n} \mathbf{S}_r x \right) \tag{3.32}$$

The next step is decomposing the $\mathbf{S}_l$ and $\mathbf{S}_r$ matrices into products of their sub-sampling matrices by applying the property introduced in eq. (3.28), which results in eq. (3.33).

$$\mathbf{Z}x = \sum_{l=1}^{n} \overline{\mathbf{S}}_l^T \overline{\mathbf{S}}_l \mathbf{Z} \left(\sum_{r=1}^{n} \overline{\mathbf{S}}_r^T \overline{\mathbf{S}}_r x \right) \tag{3.33}$$

Introducing the term $\overline{\mathbf{S}}_l \mathbf{Z}$ into the summatory over r we arrive to the expression eq. (3.34).

$$\mathbf{Z}x = \sum_{l=1}^{n} \overline{\mathbf{S}}_l^T \sum_{r=1}^{n} \overline{\mathbf{S}}_l \mathbf{Z} \overline{\mathbf{S}}_r^T \overline{\mathbf{S}}_r x \tag{3.34}$$

In order to simplify the expression, an auxiliary matrix $\mathbf{z}_{lr}$ is stated as shown in eq. (3.35). Notice that $\mathbf{z}_{lr}$ is a Toeplitz matrix of $M \times M$ elements. For the same purpose, also an auxiliary vector x_r is expressed as shows eq. (3.36).

$$\mathbf{z}_{lr} = \overline{\mathbf{S}}_l \mathbf{Z} \overline{\mathbf{S}}_r^T \tag{3.35}$$

$$x_r = \overline{\mathbf{S}}_r x \tag{3.36}$$

Introducing equations (3.35) and (3.36) into eq. (3.34) results in equation (3.37).

$$\mathbf{Z}x = \sum_{l=1}^{n} \overline{\mathbf{S}}_l^T \sum_{r=1}^{n} \mathbf{z}_{lr} x_r \tag{3.37}$$

As $\mathbf{z}_{lr}$ is a Toeplitz matrix, its product with x_r can be performed using the FFT to reduce the overall cost. However, due to the double sampling in this case the overall cost is reduced from $\mathcal{O}(N^2)$ to $\mathcal{O}(N \log M)$ instead of $\mathcal{O}(nN \log N)$. In Fig. 3.4 can be seen the comparison of the mean MVP for MoM, single sampling slotFFT and double sampling slotFFT in the same conditions performed for Fig. 3.3(b). Apart from the increment in the efficiency for the double sampling version, it can also be noticed an improvement in the stability of the curve, which presents almost no fluctuations compared with the single sampling version. This is due to the size of the FFTs, which are smaller by a factor of n compared to the single sampling version, which reduces memory accesses and the complexity of the FFT factorization.

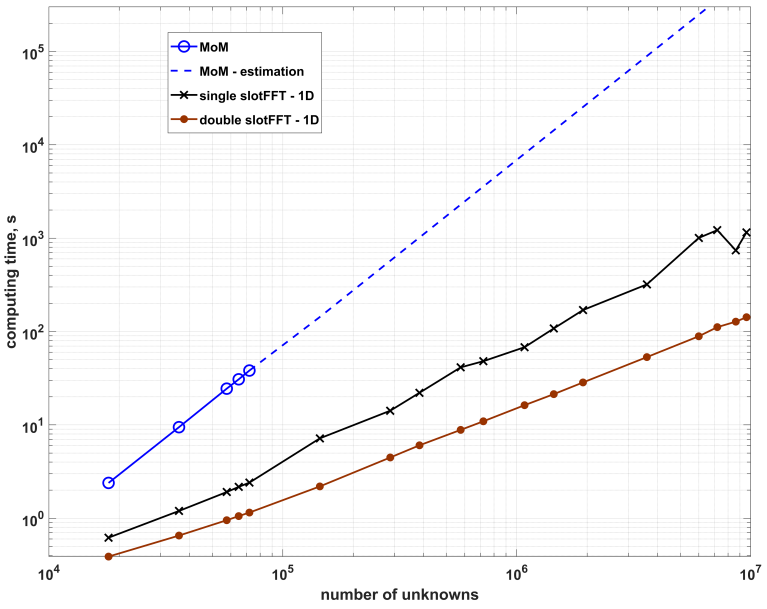

Figure 3.4: Comparison of the computing time needed with MoM and single and double sampling versions of the slotFFT method for one dimensional pattern.

3.3 Application to finite periodic structures

This section presents the results from applying slotFFT to some generic and specific problems, covering several fields of application. All the simulations were performed in the same computing cluster of the previous section, composed by 4 Intel Xeon E7-4820 at 2.00GHz (eight cores each one, 32 cores in all) and with 512GB of RAM memory, but without restrictions to the parallelization tools.

The first example presented corresponds to a large 3D cube-shaped array of dielectric spheres, used to test the simple sampling version of slotFFT applied to large structures and its stability. The structure is composed of 20×20×20 spheres of $\lambda/2$ of diameter, separated by $6\lambda/10$ between centers in the 3 dimensions. Each sphere is identically modeled with 270 RWG basis functions for the electric currents and other 270 basis for the magnetic currents, which leads to a total number of unknowns for the complete structure of $N = 4.32$ million and 298.6GB of RAM memory to storage the slotFFT impedance matrix. The problem was carried out under a normal impinging plane wave at $\theta = 0°$ with a wavelength of 780nm. The total computing time was 11 hours of CPU time to achieve a relative residual under 10^{-4} using JMCFIE formulation.

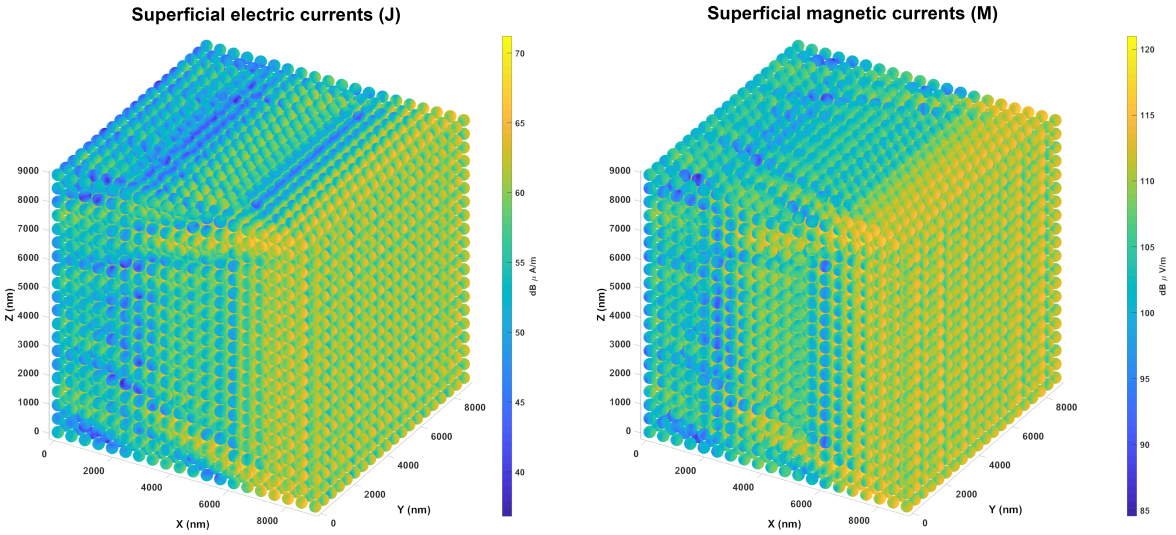

Figure 3.5: Representation of the surface electric and magnetic currents obtained through the CEM analysis of a cube-shaped array of dielectric spheres ($\epsilon_r = 3$ and $\mu_r = 1$) of $\lambda/2$ diameter and a separation of $6\lambda/10$ between centers for an incident plane wave ($\theta = 0°$) with 780nm of wavelength.

Despite of the regular and expectable distribution of the electric and magnetic surface currents, only easily appreciable in the external elements of the structure, the radar cross section (RCS) was computed to look for anomalies, shown in Fig. 3.6. This is way is easy to validate the method without needing other approaches, as the problems that my be introduced by indexation errors of the implementation would give

place to asymmetrical diagrams, which are not observable in the result obtained.

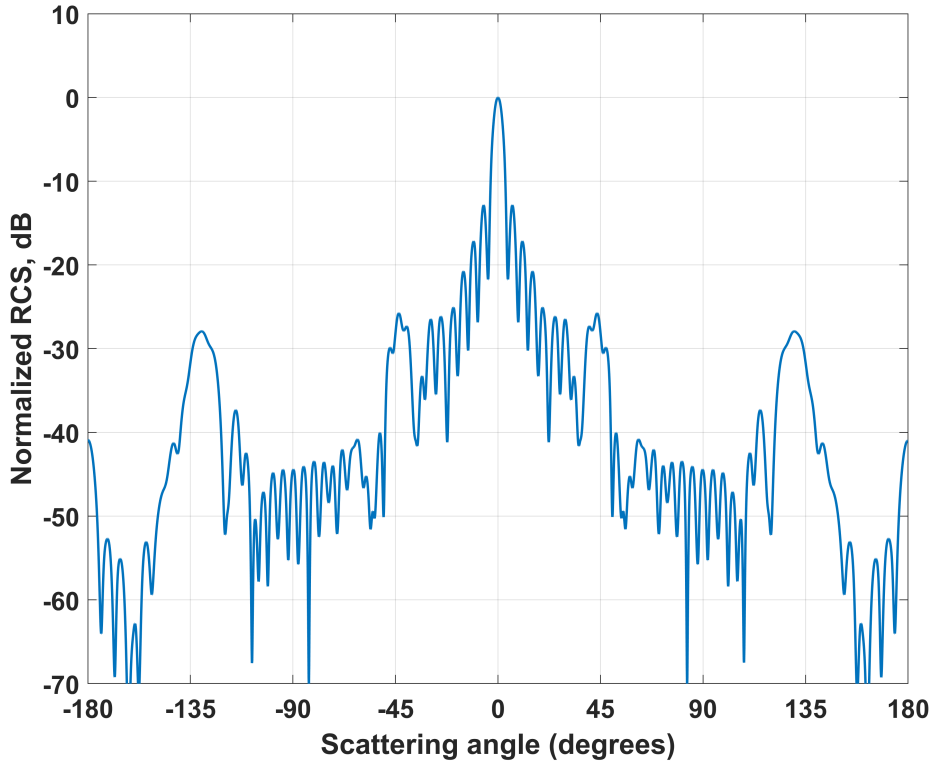

Figure 3.6: Representation of the scattering cross section at $\lambda = 780$nm obtained through the computation of the currents shown in Fig. 3.5.

As example of application to 2D structure, a plane-shaped composed of nanospheres is proposed. The structure disposes of the proper characteristics of a surface-enhancement Raman spectroscopy (SERS) substrate [45–47]. In particular, the substrate is composed of 200×200 nanospheres made of gold ($\epsilon_r = -9.3866 - j1.5293$) with 55nm of diameter separated by 56nm between centers suspended in water ($\epsilon_r = 1.7689$), shown in Fig. 3.7. The analysis required nearly 10 million unknowns to properly address the problem, illuminated by two perpendicular plane waves at a wavelength of 600nm. The simulation used 32 hours of CPU to perform the analysis using the simple sampling implementation of slotFFT and JMCFIE formulation.

The purpose of this analysis, published in [44], was to prove the effects that appear in large structures. Due to the limitations of computational resources, as well as the limitations of some commercial CEM software, often this kind of structure is studied departing from infinite structures or, on the other hand, using small ensembles, which may hide important effects common in a real scenario. This plays an important role in these kind of applications, as the SERS intensity distribution may present stationary wave-patterns effects.

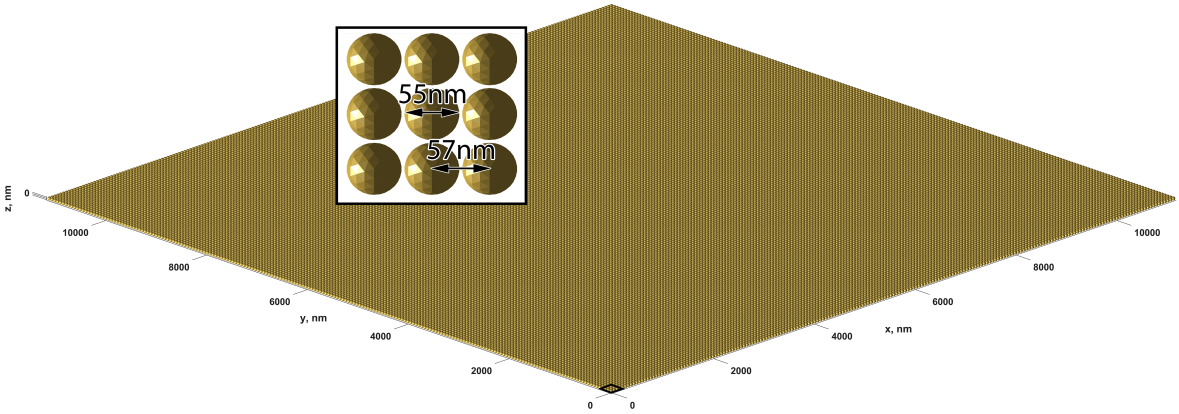

Figure 3.7: Representation of a SERS substrate composed by 200×200 gold nanospheres.

The results shown were computed applying no Raman shift [47], using for it the expression shown in eq. (3.38), where $\mathbf{E}$ is the total electric field in the presence of the SERS substrate and $\mathbf{E}_i$ the field of the incident plane wave.

$$SERS\ enhancement \approx |\mathbf{E}(\omega_{in})|^4 |\mathbf{E}_i(\omega_{in})|^{-4}, \tag{3.38}$$

In Fig. 3.8(a) it can be observed the SERS enhancement obtained after smoothing with a 2D Gaussian filter, which simulated the effect of the lenses used to observed and measure the effect. As can be appreciated in the color axis of the representation, the SERS representation is saturated to ease the observation of the the effects present in the structure. A stationary wave pattern can be seen over the structure at the analyzed frequency, as well as a remarkable the edge-effect in the borders of the substrate, demonstrating how recommendable is to avoid approximations in the simulations of this kind of structures. Figure 3.8(b) shows the field represented without filtering, as could be measured with gauge. The hotspots, points with high field concentration, between nanospheres can be easily appreciated, with peaks of $1.0824 \cdot 10^5$ arbitrary units. Notice that the SERS magnitude is also saturated to remark the hotspots.

The following result belongs to a comparison of the precision of two homogeneization methods versus the method of moments, also published in [44]. This kind of methods consists in approaching a complex 3D grid of elements with a size minor than the incident wavelength as an homogeneous solid body with an intermediate permittivity. For the case of study two different homogeneization methods were used. The first one is the Maxwell-Garnett formula [43], shown in eq. (3.39), and the Bruggeman rule [43], shown in eq. (3.40), where ϵ_{eff} is the resulting permittivity, ϵ_1 is the permittivity of the elements, ϵ_2 the permittivity of the sorrounding medium and q is the fraction of volume of the inclusions over the total space, which in our case is equal to 1/8.

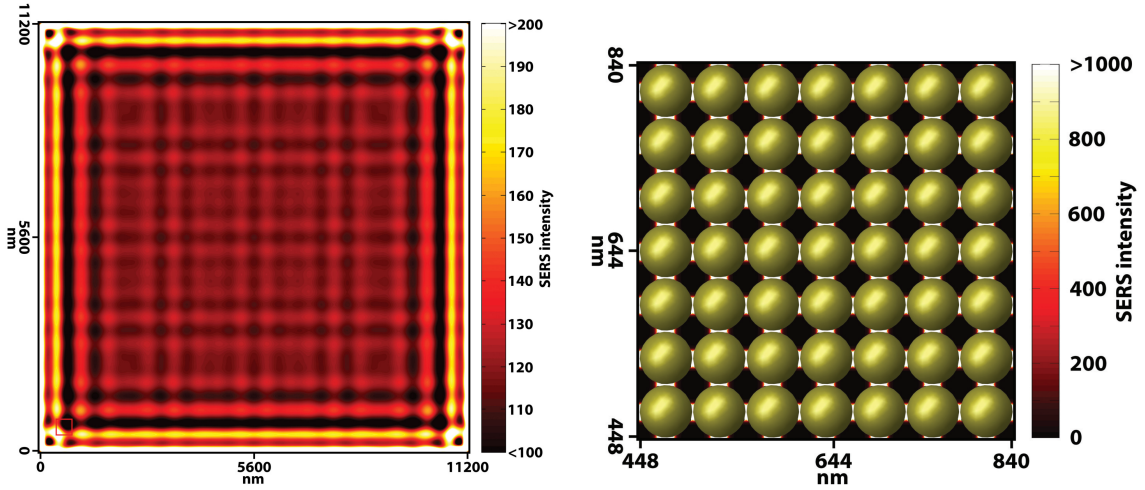

(a) Representation of the SERS intensity obtained filtered by a Gaussian mask.

(b) Detail of the region marked showing the hotspots between adjacent nanospheres.

Figure 3.8: Representation of the SERS intensity computed for the substrate shown in Fig. 3.7.

$$\epsilon_{eff} = \epsilon_2 + 3q\epsilon_2 \frac{\epsilon_1 - \epsilon_2}{\epsilon_1 + 2\epsilon_2 - q(\epsilon_1 - \epsilon_2)} \tag{3.39}$$

$$(1-q)\frac{\epsilon_2 - \epsilon_{eff}}{\epsilon_2 + 2\epsilon_{eff}} + q\frac{\epsilon_1 - \epsilon_{eff}}{\epsilon_1 + 2\epsilon_{eff}} = 0 \tag{3.40}$$

The example analyzed at 550nm of wavelength is a cube-shaped metastructure, partially represented in red color in Fig. 3.9. It is composed of $110 \times 110 \times 110$ nanocubes of $\lambda/10$ side, with $\epsilon_r = 3$ and $\mu_r = 1$ and a separation of $\lambda/5$ between centers distributed in a uniform 3D grid. The constitutive properties of the dielectric material of the nanocubes is $\epsilon_r = 3$ and $\mu_r = 1$ and the nanocubes are suspended in vacuum medium. The structure analyzed with the simple sampling version of slotFFT and JMCFIE formulation possesses 48 million of unknowns.

In Fig. 3.9 can be seen the resulting RCS of the structure, obtained for an incident plane wave ($\theta = 0^o$). The same example is analyzed through the MLFMA algorithm [26], using equivalent homogeneous structures with 12.1μm with $\epsilon_r = 1.1579$ and $\epsilon_r = 1.1638$, obtained with the Maxwell-Garnett and Bruggeman homogenization formulas respectively. Using the appropriated mesh density, the equivalent problem needed 1.7 million unknowns.

In order to compare the results, the RMS error is calculated using the expression $\eta(\vec{x}_{ref}, \vec{x}_{approx}) = \|\vec{x}_{ref} - \vec{x}_{approx}\|/\|\vec{x}_{ref}\|$, where $\vec{x}_{ref}$ is the reference signal obtained

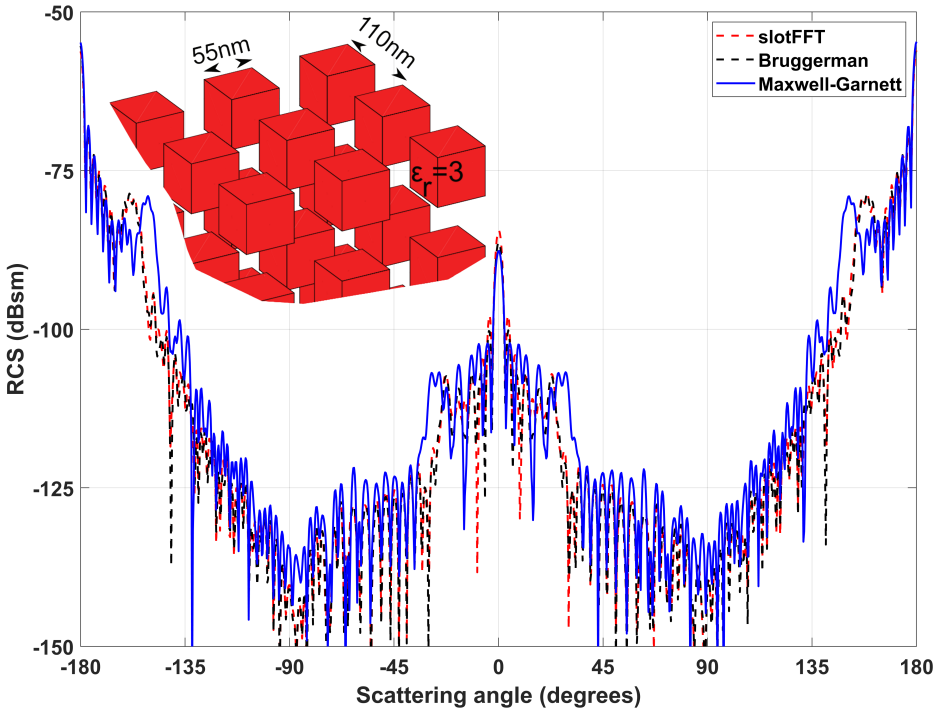

Figure 3.9: Representation of the RCS at $\lambda = 550$nm of a cube-shaped array of dielectric nanocubes with $\epsilon = 3$ of $\lambda/10$ side and a separation of $\lambda/5$ between centers obtained using the method of moments accelerated with slotFFT compared to the Maxwell-Garnett and Bruggerman homogeneization methods.

with slotFFT, $\vec{x}_{approx}$ is the signal obtained through the homogeization method, and $\|\vec{x}\|$ is the euclidean norm of vector $\vec{x}$. The obtained RCS for both homogeneization formulas provide accurate results for general purposes, attaining a RMS error $\eta = 0.0211$ when the Maxwell-Garnett formula is used and $\eta = 0.0623$ with Bruggeman. However, it can be appreciated the differences at 30 degrees from the principal directions between the electromagnetic scattering of the two homogeneous cubes and response of the real large periodic composite object obtained with slotFFT algorithm.

The next example, analyzed with the double sampling version of slotFFT, is a periodic helical structure [48], whose periodicity is not based only on translations, but also in rotations. Despite this, it can be analyzed by slotFFT without any modifications in the code. It id compose by 90 gold nanorods of 550nm disposed in 15 spirals distributed as shown in Fig. 3.10, which shows the electric and magnetic surface currents distribution of the problem at a wavelength of 600nm. Each nanorod is modeled with 1209 RWG basis functions for each electric and magnetic surface currents, which results in a total number of unknowns of $N = 218K$. The electromagnetic analysis was carried at 31 different wavelengths from 400nm to 900nm. Each example was analyzed using as excitation an impinging plane wave with $\theta = 0°$ and vertical polarization. The total computing time for the example was 9 hours of CPU time to achieve a tolerance lower

than 10^{-6} using JMCFIE formulation with the double sampling version of slotFFT.

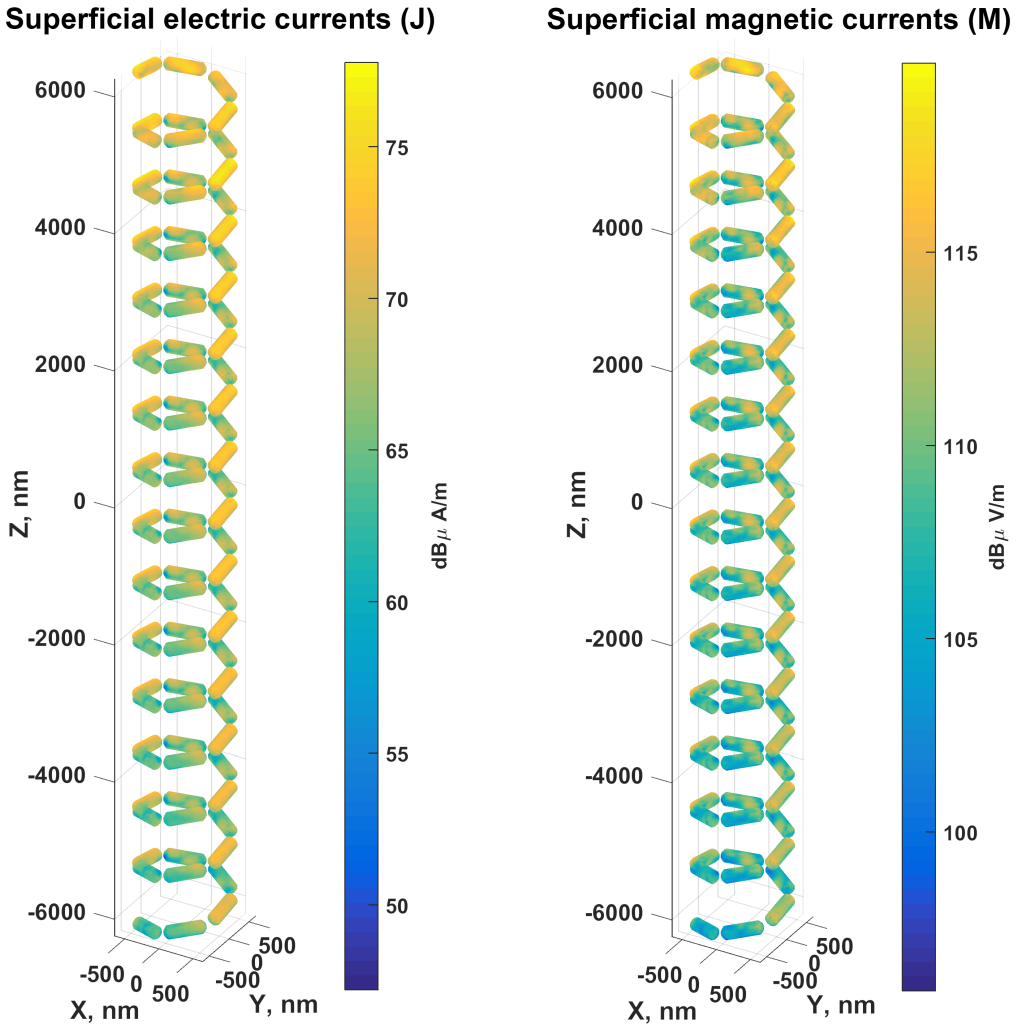

Figure 3.10: Representation of the surface electric and magnetic currents obtained through the CEM analysis of a simple helix for an incident plane wave ($\theta = 0°$) with 600nm of wavelength.

The resulting currents were used to compute the *scattering, absorption and extinction cross sections* in the analyzed range, shown in Fig. 3.11. The convergence was not regular at all the frequencies analyzed, as there were some of them where the structure resulted to be resonating, slowing down the resolution.

The last example introduced is a double helical structure composed of 2×60 gold nanorods of 25nm of length, represented in Fig 3.12. The purpose of the analysis was to compute the circular dichroism [49–53] of the structure, which has application in biomedical field to detect specific diseases. The structure analyzed is a bigger approximate replication of the structure shown in Figure S10. of the *SI Appendix* of [53].

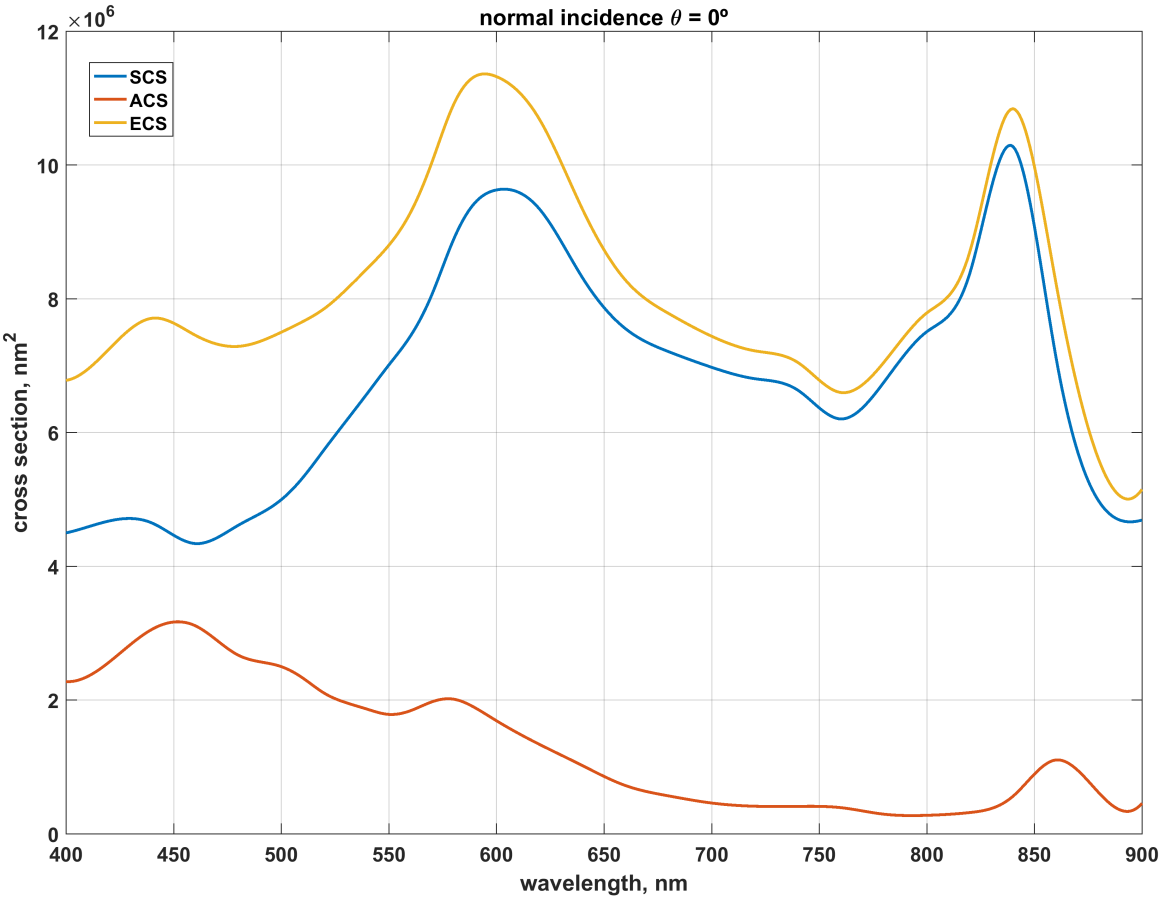

Figure 3.11: Scattering, absorption and extinction cross sections of the helical structure of Fig. 3.10 in the optical range for incident plane waves ($\theta = 0°$).

The structure, modeled with half-million unknowns, was analyzed at 45 wavelengths from 400nm to 1200nm, performing at each one two analyses using right and left-hand circular polarized planewaves impinging with $\theta = 0°$. The analysis took a mean time of 10 hours per wavelength using JMCFIE formulation. The circular dichroism is computed using the expression in eq. (3.41), where ECS_{LH} is the extinction cross section resulting from the left-handed excitation and ECS_{RH} the resulting from the right-handed excitation.

$$C.D. = \frac{ECS_{LH} - ECS_{RH}}{ECS_{LH} + ECS_{RH}} \tag{3.41}$$

Figure 3.13 shows the resulting circular dichroism (left), obtained from the extinction cross sections for each polarization (right).

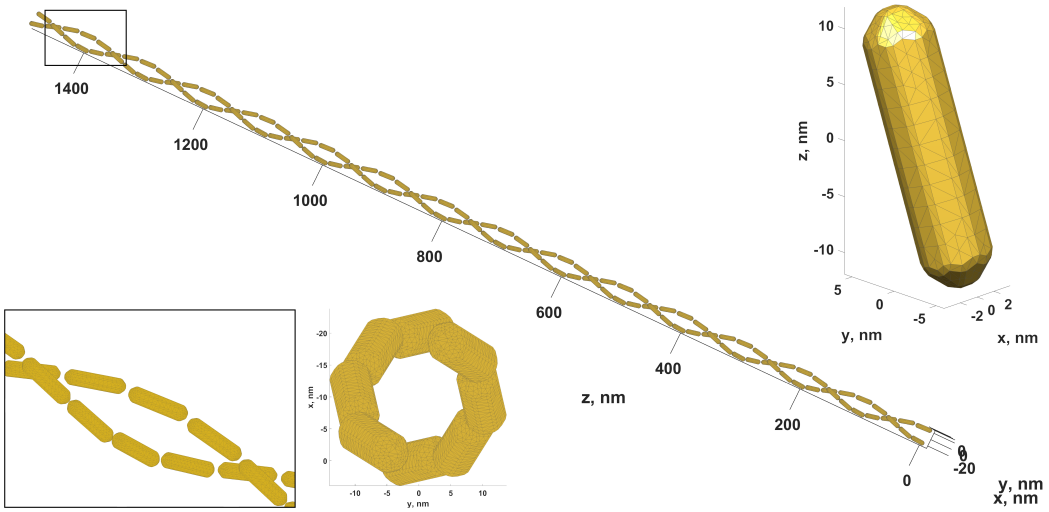

Figure 3.12: Representation of a double helical structure composed by 2x60 gold nanorods of 25nm of length.

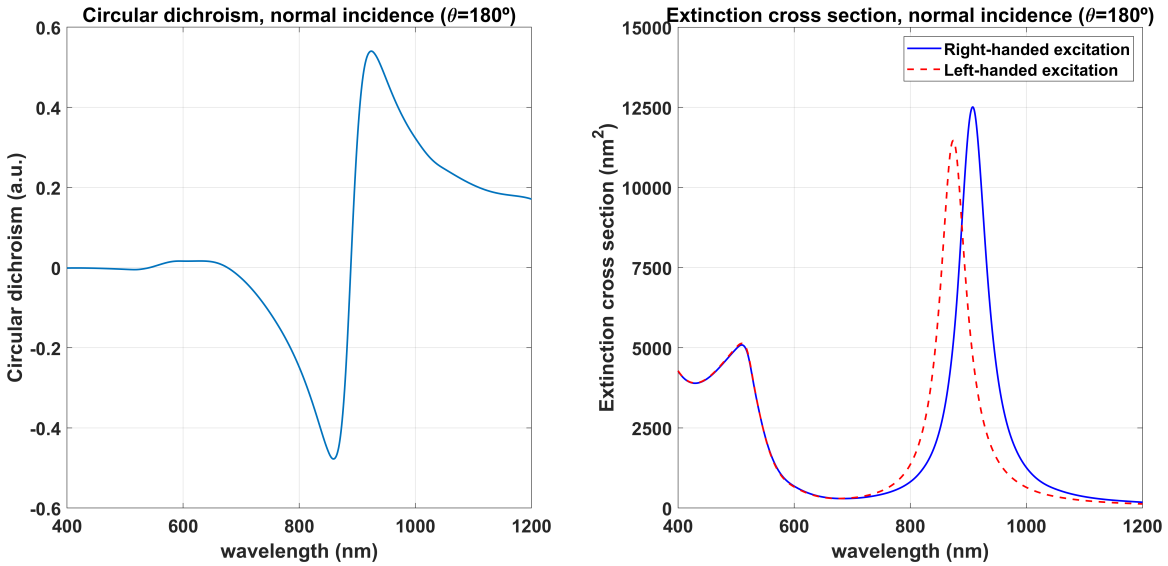

Figure 3.13: Representation of the circular dichroism (left) and the extinction cross section (right) of the double helical structure shown in Fig. 3.12 for normal incidence ($\theta = 180°$) from 400nm to 1200nm.

3.4 Extension to aperiodic element-wise materials structures

In the expressions developed in 2.3 it can be observed that the coupling sub-blocks in expression (2.51) are only dependent on the constitutive parameters of the common medium. In the case of finite periodic structures, this met for the coupling between all elements, with the exception of the self-coupling sub-block, which depends on the constitutive properties of the inner and the external mediums.

Due to this, slotFFT can be extended to structures with geometrical periodicity composed by homogeneous elements with different materials as, for example, the structure shown in Fig. 3.14.

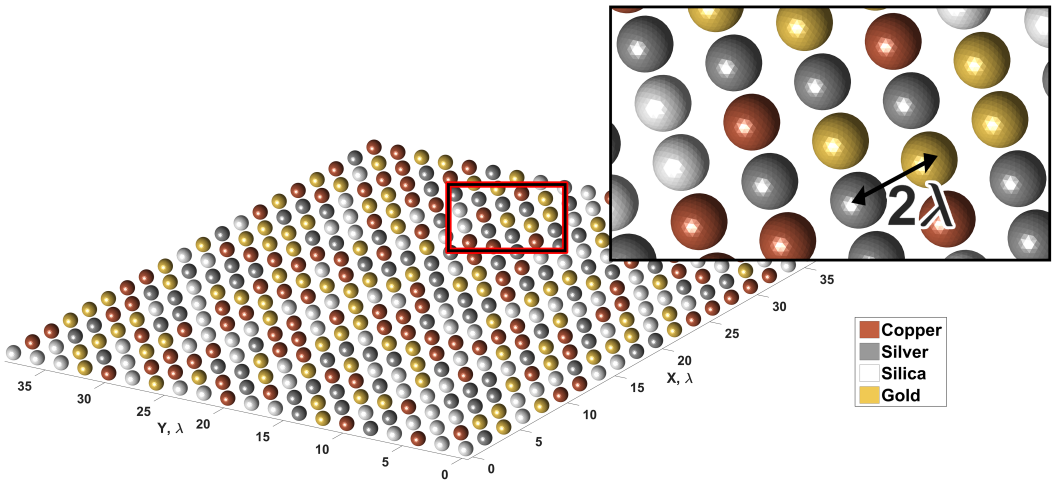

Figure 3.14: Analyzed periodic array, composed by 20×20 dielectric spheres composed of multiple materials distributed arbitrarily(gold, silver, copper and silica) of λ diameter separated by 2λ.

To carry out this, the process is simple. When setting the impedance matrix for the method, the self-coupling sub-block is set entirely to zero to remove its contribution to the solution. Then, after the main MVP has been carried out with slotFFT, the contribution of the self-coupling is computed individually for each element and added to the solution. Despite of this, the impact over the computing time is negligible, as shown in Fig. 3.15, where the slotFFT version for this kind of problem does not differ from the standard version for structures of only one material.

As example of this capability, the structure shown in Fig. 3.14, presented at [54], was analyzed. For this the excitation was a vertically polarized incident planewave with λ =550nm an $\theta = 0°$, using PMCHWT formulation. The spheres, of λ diameter and separated by 2λ between centers, have been modeled with n =2160 basis functions, making a total of N =864K unknowns for the complete structure. The distribution

was generated randomly using the following materials: golf ($\epsilon_r = -5.9310 - j2.0971$), silver ($\epsilon_r = -12.9374 - j0.4287$), copper ($\epsilon_r = -5.6549 - j5.1989$) and silica ($\epsilon_r = 2.1756 - j2.36e - 7$).

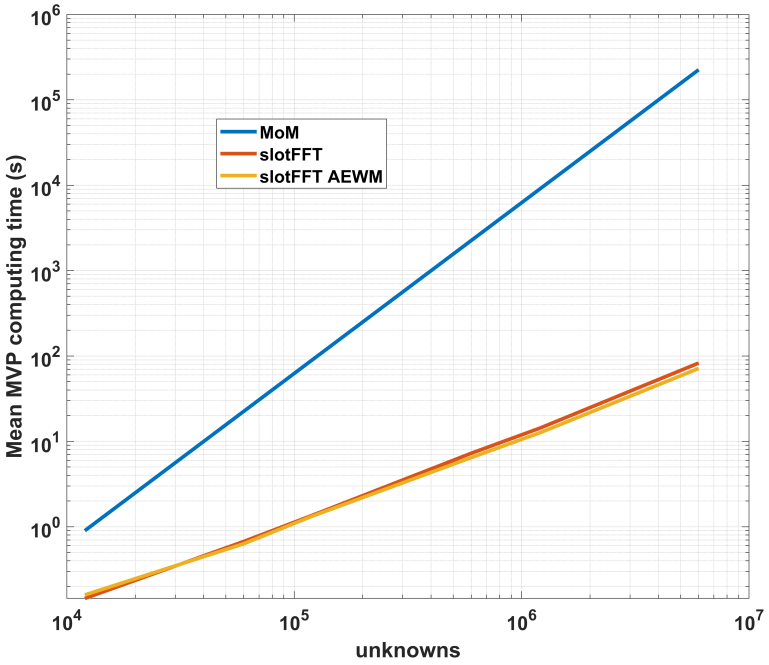

Figure 3.15: MVP computing times for MoM, double slotFFT and double slotFFT for aperiodic element-wise material structures.

The obtained RCS is shown in Fig. 3.16, where, as could be expected from the random distribution of the materials, appear several asymmetries.

This is just an example in the limits if the scope of the thesis, which opens the possibility of applying the method for approaching specific problems and even for optimization processes, i.e. optimization of discrete dielectric lenses [55]. Despite of this capability of analyzing finite periodic structures with multiple constitutive parameters, the method is still limited to structures composed by geometrically identical elements.

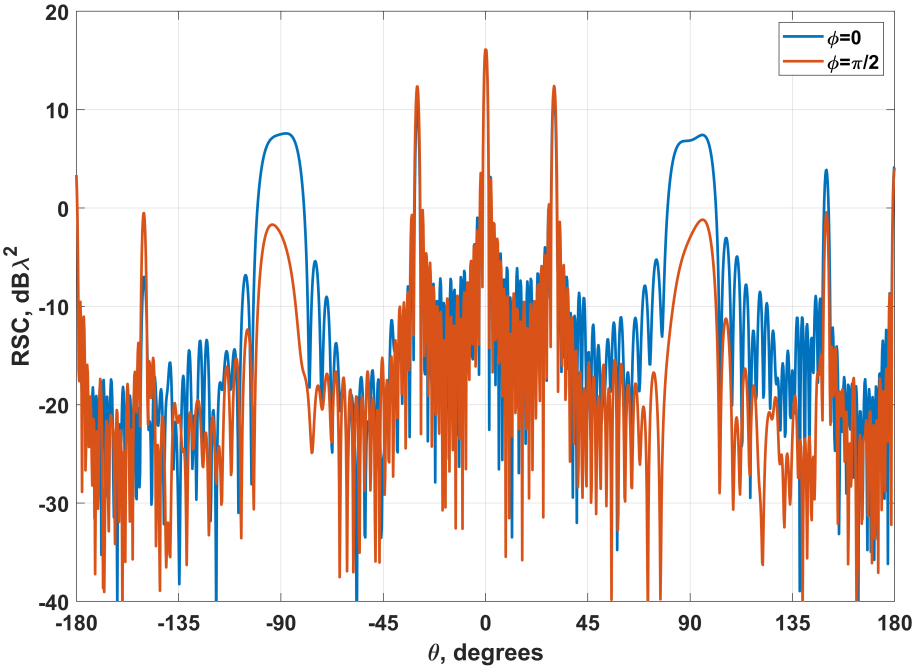

Figure 3.16: Representation of the RCS at $\lambda = 550$nm ($\epsilon_r = -5.9310 - j2.0971$ for gold, $\epsilon_r = -12.9374 - j0.4287$ for silver, $\epsilon_r = -5.6549 - j5.1989$ for cooper and $\epsilon_r = 2.1756 - j2.36e - 7$ for silica) obtained for the structure shown in Fig. 3.14.

3.5 Extension to roughly finite periodic structures

Up until now, all the structures shown in this documents have been *perfect* periodic structures. This is, all the elements were identically modeled and perfectly distributed in uniform grids or according to certain patterns described by translations and rotations. However, this is not close to reality, as due to the fabrication processes, i.e. based on wet chemistry processes or lithography [52], small imperfections, displacements or rotations in the elements and their distribution into the structure are common. Also, there are special structures, i.e. metasurfaces or reflectarrays, that do not tend to present these problems but, instead, are composed of geometrically different elements, which makes impossible to treat them with slotFFT.

In order to address such kind of problems, several possibilities were considered. In particular one of the possible approaches was the application of the Huygens' equivalence theorem. This theorem was the core of the project developed in the second research visit performed in Autumn 2019, held by the Laboratory of Advanced Computational Electromagnetics (LACE), which was focused on its application to local mesh refinement techniques [56]. The theorem states that the fields inside *or* outside

of a close surface, named Huygens' surface (HS), can be described by equivalent surface currents determined by the tangential components of the fields on the surface. This is illustrated in figures 3.17(a) and 3.17(b), which represents the application of the theorem to isolate a local problem from the surroundings and the inverse process respectively, where $\mathbf{E}_i$ and $\mathbf{H}_i$ are incident electric and magnetic fields respectively, $\mathbf{E}_s$ and $\mathbf{H}_s$ are scattered electric and magnetic fields respectively, S is the HS used to apply the theorem, and ϵ_i and μ_i the constitutive parameters of region R_i.

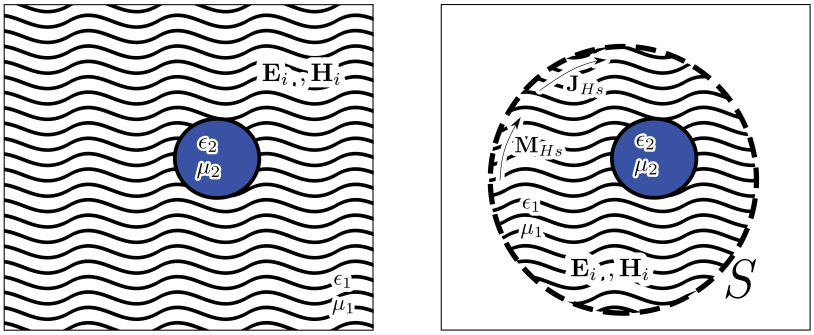

(a) Isolating the local problem from the medium.

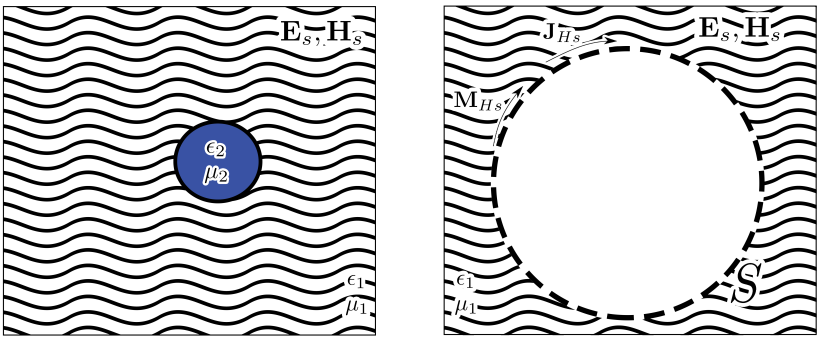

(b) Isolating the medium from the local problem.

Figure 3.17: Representation of the application of the Huygens' equivalence theorem.

The surface electric and magnetic currents on the HS $\mathbf{J}_{Hs}$ and $\mathbf{M}_{Hs}$ are given by equations (3.42) and (3.43), where $\mathbf{H}_{Hs}$ and $\mathbf{E}_{Hs}$ are the magnetic and electric fields on the Huygens' surface S and $\hat{\mathbf{n}}$ the normal to S. $\mathbf{H}_{Hs}$ and $\mathbf{E}_{Hs}$ can have any origin, i.e. they can be generated by external sources to S, i.e. an impinging planewave, or internal to S, i.e. an antenna.

$$\mathbf{J}_s = \hat{\mathbf{n}} \times \mathbf{H}_{Hs} \tag{3.42}$$

$$\mathbf{M}_s = \mathbf{E}_{Hs} \times \hat{\mathbf{n}} \tag{3.43}$$

In order to analyze non-periodic problems with the integration of Huygens' equivalence theorem into slotFFT,the process described next is applied to perform the MVP, as illustrated in Fig. 3.18. This figure represents the steps needed to compute the transmission from one element to another through multiple HS. The HS enclose the individual elements, isolating them form the surrounding (external) medium R_1. In this way, the original problem can be solved using slotFFT as long as the HS surfaces are chosen properly, posing a perfectly periodic collection of equivalent surfaces with no contact between them. The MVP can be then computed as follows:

1. First, the fields generated by the electric and magnetic surface currents $\mathbf{J}_i$ and $\mathbf{M}_i$ of body i are computed on its corresponding HS S_i. Then, using equations (3.42) and (3.43) the electric and magnetic surface currents $\mathbf{J}_{Hs_i}$ and $\mathbf{M}_{Hs_i}$ are computed on S_i.

2. The transmission between all the HS is performed using the couplings between them. This is carried out with slotFFT. In the case of multiple elements this step aggregates the radiation of all HS S_i on receiving HS S_j, with $1 \leq i \leq M$, being M the number of elements in the structure, except for $i = j$.

3. Using again expressions (3.42) and (3.43) the electric and magnetic fields over the HS S_j are converted into equivalent surface electric and magnetic currents $\mathbf{J}_{Hs_j}$ and $\mathbf{M}_{Hs_j}$. Then, the $\mathbf{J}_{Hs_j}$ and $\mathbf{M}_{Hs_j}$ are used to calculate the incoming radiation into the receiving element j.

In addition to these steps, the self-coupling of each element must be carried out separately (in the same way that is performed in 3.4).

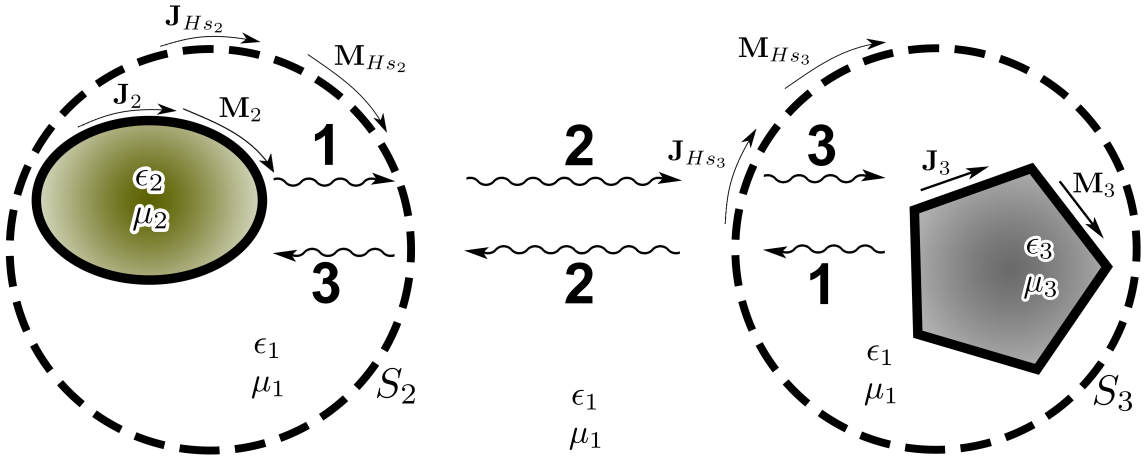

Figure 3.18: Representation of the steps to approach a generic problem with two bodies enclosed by Huygens' surfaces.

3.5.1 Validation and application

The first step was to test the proposed framework and its possible impact on the solution. For this, an array of 5×5 PEC cubes with $\lambda/2$ of side and a separation of 1.65λ between centers was used. Each cube is modeled with 460 basis functions. The structure was illuminated by an impinging planewave with $\theta = 0°$. The Huygens' surfaces used were spheres with 1.4λ diameter modeled with 1800 basis functions. Notice that, in order to work properly, the separation must be enough to avoid the contact between the enclosing Huygens' surfaces.

In Fig. 3.19 the obtained surface electric currents distribution is shown for the solution with slotFFT and slotFFT with the integrated Huygens' surfaces. The RMS error introduced by the Huygens' surfaces for the currents was η =0.00486 (η =0.00216 and η =0.04848 for magnitude and phase). The RCS computed from the solution is shown in Fig. 3.20. It can be seen how both curves fit perfectly. The RMS error introduced on the RCS is η =0.001. In view of these results the well behavior of the integration of the Huygens' surfaces with slotFFT is confirmed.

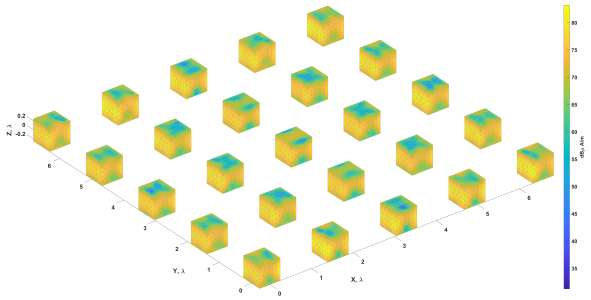

(a) straight procedure.

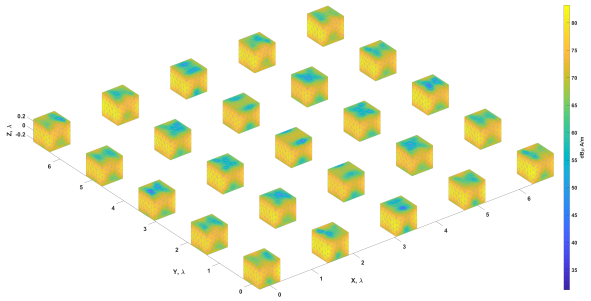

(b) with Huygen's surface.

Figure 3.19: Surface electric currents distribution for the validation example of the integration on the Huygen's equivalence theorem compared to the straight approach.

With the framework validated, the method was ready to be applied to a non-periodic structure. For this case, a randomly generated 10×10 was generated, as shown

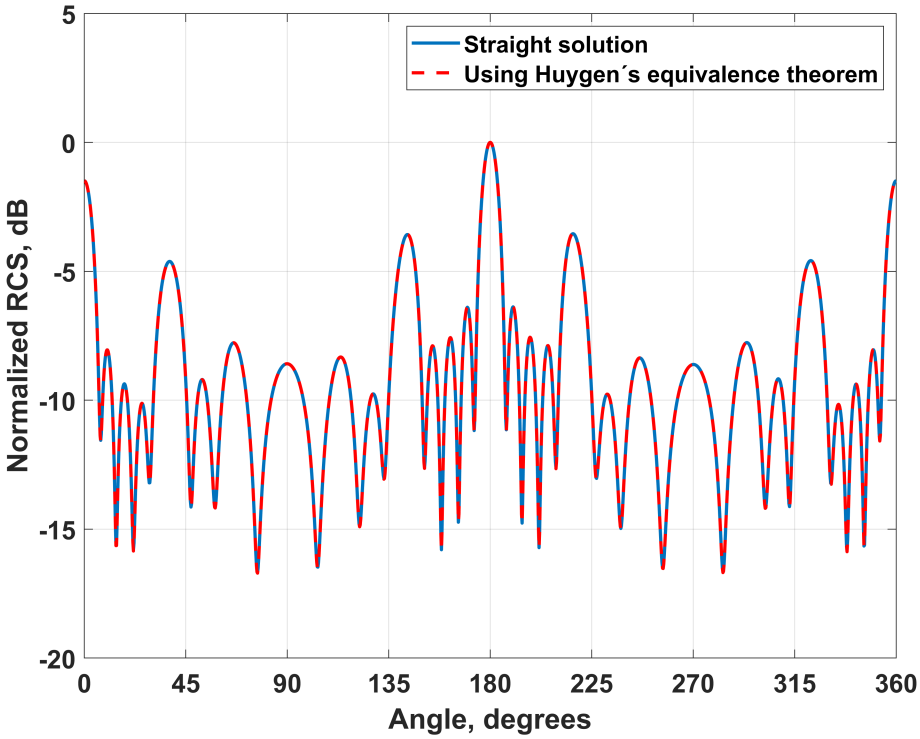

Figure 3.20: Comparison of the scattering diagrams obtained from the currents shown in Fig. 3.19 using the straight and the Huygen's equivalence theorem procedure.

in Fig. 3.21. The displacements and rotations are carried out in such a way that the elements are always kept within the limits of the Huygens surface. The elements that compose the structure are the same PEC cubes that in the validation example, as well as the Huygens' surfaces and their distribution and the excitation of the problem. The obtained surface electric currents are represented in Fig. 3.22, and the RCS associated is presented in Fig. 3.23.

It must be taken into account that the approach is not as efficient as slotFFT applied to pure periodic structures, as it needs an important number of additional operations. However, this is a first proof of concept, revealing that this procedure brings new possibilities, such as the introduction of small defects in the a priori periodic structures, or the use of different elements, transforming non-periodic into periodic problems which can be directly addressed by slotFFT.

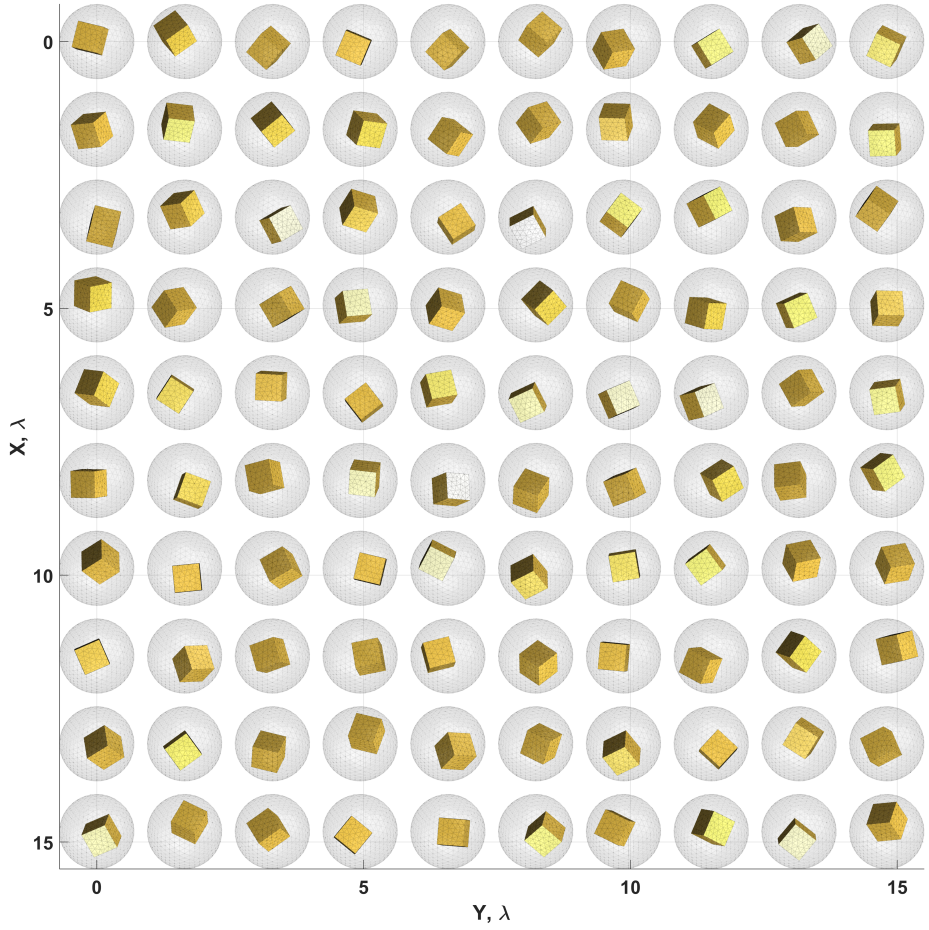

Figure 3.21: Structure composed by quasi-arbitrary distributed PEC cubes of 0.6λ of side and the associated periodic array of Huygen's surfaces.

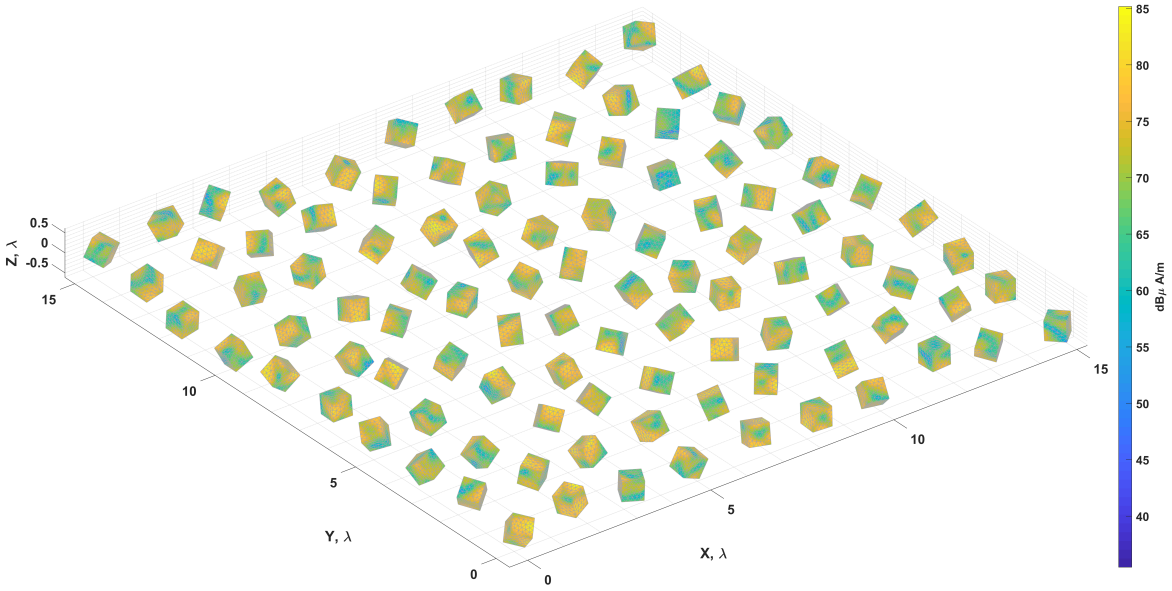

Figure 3.22: Surface electric currents distribution obtained for the structure shown in Fig. 3.21 using the Huygens' equivalence theorem for its analysis as a periodic structure with slotFFT.

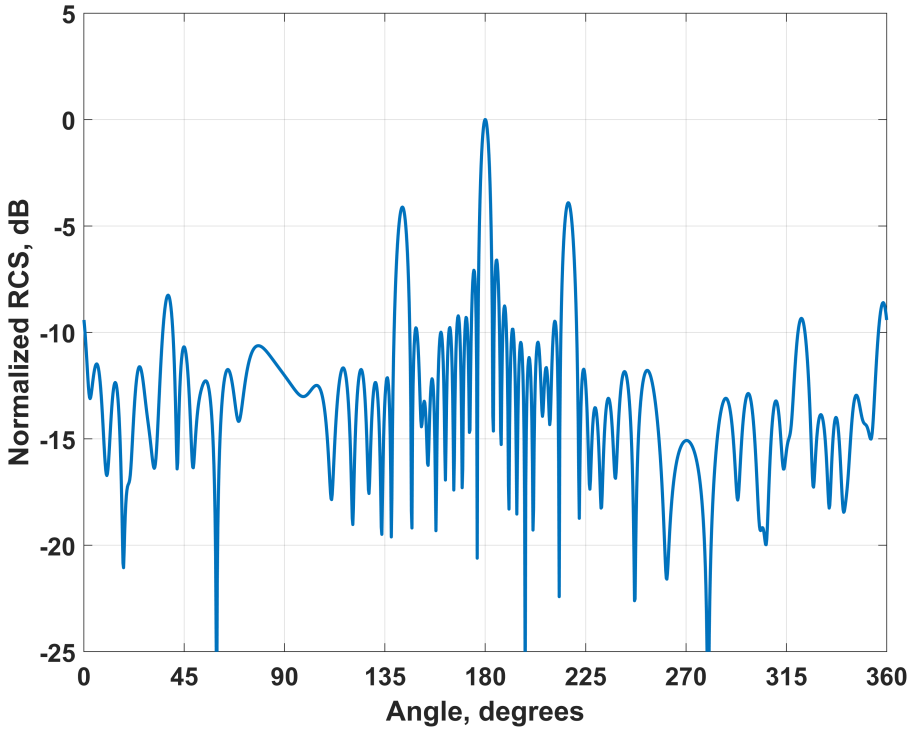

Figure 3.23: Scattering diagram obtained from the currents shown in Fig. 3.22.

Chapter 4

Matrix compression for the acceleration of periodic CEM problems

Contenido

4.1 Introduction 52

4.2 Full-domain power decoupled macrobasis 53

4.2.1 Definitions and formulation 54

4.2.2 Macrobasis generation 61

4.2.3 Macrobasis representativeness 63

4.3 Skeletonization scheme 69

4.4 Integration of matrix compression methods into slotFFT 71

4.5 Application and results 72

4.6 Application of matrix compression for preconditioning periodic problems 79

This chapter is focused on the integration of matrix compression methods (MCM) into the slotFFT method in order to increase the acceleration achievable with limited precision loss. The first section introduces why CEM problems are suitable for MCM application and provides a review of the main methods withing the state-of-the-art of MCM applicable to CEM problems. In the second section a novel kind of full-domain macrobasis, applicable to PEC and dielectric problems, are introduced as part of work developed in this thesis. The next chapter introduces the skeleton decomposition, which was the topic that the first research visit performed during the thesis focused

on. The fourth chapter introduces how is performed the matrix compression within slotFFT algorithm and how some basic problems of the process are avoided. At last, some results are introduced in the fifth section with an analysis of the impact over the precision of the MCM. Among these results some especial cases of application are also shown to prove the potential of the complete framework.

4.1 Introduction

The procedure to solve scattering problems through SIE-MoM gives place to prohibitive needs in terms of CPU time and memory to compute and store the MoM impedance matrix when large structures are tackled. This also derives in high computing times to perform the MVP when the problem is solved through iterative solvers. This is especially noticeable in the case of large structures with high level of details, which increases the mesh density to properly model the currents behavior, hence the number of basis functions needed rises drastically. Despite this, when the problem is solved, the influence of the basis of those high detail parts are only noticeable in the coupling between near elements of the structure, whereas in the coupling with distant parts the small details do not contribute with the same significance. This is due to the rank-deficient property of the sub-matrices that model the coupling between well-separated bodies, derived from the nature of the Green's function. In the case of finite periodic structures, most of the coupling sub-matrices of the MoM present noticeable low rank, which makes this kind of problem especially suitable for the application of MCM.

One of the most widespread method to deal with the low-rank property of the CEM problems is named characteristic basis functions method (CBFM) [57–61], which has particular applications to periodic structures [62,63].In order to approach the problem, the CBFM manipulated the MoM impedance matrix. From this, a first set of primary macrobasis is generated for the self-coupling interactions, and a secondary and higher order set of macrobasis is computed specifically for the rest of the interactions. Due to this procedure, CBFM achieves a high reduction over the total number of unknowns, hence the computational resources are reduced.

The adaptive cross approximation (ACA) algorithm [64–69] is another widespread method proposed originally in [70], and can integrate the CBFM for other purposes [71]. This algorithm uses the rank deficient property of the MoM coupling sub-matrices when the coupled source and test basis functions clusters are well separated to perform matrix compression taking into account a set tolerance. The synthetic functions approach (SFX) [72, 73] is similar to the CBFM but, it generates the macrobasis functions from each domain introducing field considerations and domain boundaries, and unions between adjacent domains (when connected) to properly address the problem, instead

of manipulating the matrix and using overlapping regions between domains as CBFM does.

A different approach to compress the MoM impedance matrix in contrast to the methods above is to discard the basis functions that posses a low contribution to the solution. For this, a process to identify what are named *dominant basis* can be performed. The equivalent source approximation, introduced in [74], and its nested version [75–77], perform this process. To perform the MoM impedance matrix, it departs from the capability of describing the fields generated over a closed surface from the possible sources within it, by equivalent sources over the closed surface. By doing this, the number of equivalent sources used to describe the inner sources can be smaller, reducing the number of unknowns needed to model the problem.

Another method to get rid of the basis functions with low contribution to the far field consists in generating the skeletons of the structure through interpolative decomposition (ID) [78–81]. This method is introduced briefly in section 4.3, as was fully integrated in the slotFFT algorithm during the research visit performed in 2018 at the Politecnico di Torino.

In addition to these methods, the full-domain power decoupled macrobasis developed in this thesis, presented in several conferences [82–87], can be efficiently applied to CEM periodic problems. As will be introduced in section 4.2 theses macrobasis are independent of the position of the elements of the structure and the applied excitation, which permits the application of the method with a negligible additional computational cost.

4.2 Full-domain power decoupled macrobasis

This section departs from the work developed in the PhD thesis of Gloria Gajardo [88], which focused on the applications on acceleration and compression of transformations based on the electromagnetic radiation in PEC structures. In the case of dielectric problems, the surface electric and magnetic currents could be modeled separately with that framework. In this thesis a novel approach is developed, which is derived from the energy conservation theorem in electromagnetics. The macrobasis obtained in through the developed method in this thesis combines both surface electric and magnetic currents.

4.2.1 Definitions and formulation

A body suspended in an homogeneous medium without losses, with constitutive properties ϵ_1 and μ_1, radiates power generated its scattered fields, or by its currents in the case of an antenna. This radiated power can be calculated using eq. (4.1), where S is a closed surface enclosing the body, $\mathbf{E}$ and $\mathbf{H}$ are the harmonic electric and magnetic field radiated by the body, i.e. the scattered fields, and the superscript * denotes conjugate complex. Figure 4.1 shows a generic representation of this for a problem of an homogeneous arbitrary object with constitutive properties ϵ_2 and μ_2.

$$P_r = \frac{1}{2} \oiint_S \Re\left(\mathbf{E} \times \mathbf{H}^*\right) \cdot d\mathbf{s} = \Re\left(P_e\right) \tag{4.1}$$

The term P_e, expressed in eq. (4.2), is the complex radiated power.

$$P_e = \frac{1}{2} \oiint_S \left(\mathbf{E} \times \mathbf{H}^*\right) \cdot d\mathbf{s} \tag{4.2}$$

Based on the conservation of energy theorem, P_e can be expressed as in eq. (4.3), where V represents the volume enclosed by S and $\mathbf{J}$ and $\mathbf{M}$ are the electric and magnetic currents inside the volume.

$$\begin{aligned} P_e &= \oiint_S \left(\mathbf{E} \times \mathbf{H}^*\right) \cdot d\mathbf{s} \\ &= -\iiint_V \left(\mathbf{H}^* \cdot \mathbf{M} + \mathbf{E} \cdot \mathbf{J}^*\right) dv - j\omega \iiint_V \left(\mu \left|\mathbf{H}\right|^2 + \epsilon \left|\mathbf{E}\right|^2\right) dv \end{aligned} \tag{4.3}$$

Based on the Huygens' theorem an equivalent problem can be posed, where the object is replace by surface electric and magnetic currents over the surface that encloses the object, also shown in Fig. 4.1. Under this conditions, $\mathbf{J}$ and $\mathbf{M}$ in eq. (4.3) are surface density current functions over the surface S. Theses equivalent electric and magnetic currents can be calculated by the Huygens' theorem as $\mathbf{J} = \vec{n}_1 \times \mathbf{H}$ and $\mathbf{M} = -\vec{n}_1 \times \mathbf{E}$. In the equivalent problem the first volume integral in the right part of eq. (4.3) only takes values at the surface S' of the body and then it can be expressed as in eq. (4.4). It must be taken into account that in the left part of this expression $\mathbf{J}$ and $\mathbf{M}$ denote volumetric current densities, whereas in the right part denote surface

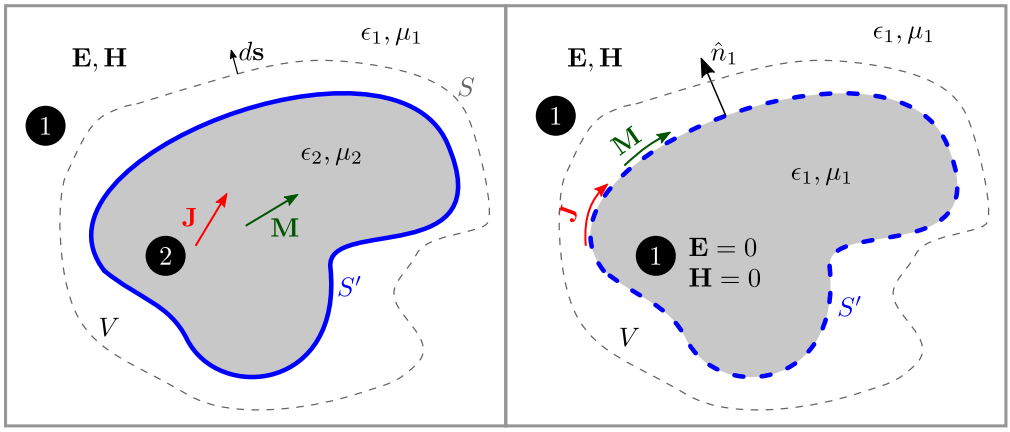

Figure 4.1: Radiation of an object as a result of electric and magnetic currents in the interior. Equivalent problem for an homogeneous object.

current densities.

$$\iiint_V \left(\mathbf{H}^* \cdot \mathbf{M} + \mathbf{E} \cdot \mathbf{J}^*\right) dv = \oiint_{S'} \left(\mathbf{H}^* \cdot \mathbf{M} + \mathbf{E} \cdot \mathbf{J}^*\right) ds'. \tag{4.4}$$

By replacing the integral in (4.4) in (4.3), we obtain the expression shown in eq. (4.5).

$$\begin{aligned} P_e &= \oiint_S \left(\mathbf{E} \times \mathbf{H}^*\right) \cdot d\mathbf{s} \\ &= -\oiint_{S'} \left(\mathbf{H}^* \cdot \mathbf{M} + \mathbf{E} \cdot \mathbf{J}^*\right) ds' - j\omega \iiint_V \left(\mu_1 \left|\mathbf{H}\right|^2 + \epsilon_1 \left|\mathbf{E}\right|^2\right) dv \end{aligned} \tag{4.5}$$

As the medium 1 is lossless ($\Im(\epsilon_1) = \Im(\mu_1) = 0$) then expression eq. (4.6) is met, and eq. (4.1) can be rewritten as shown in eq. (4.7).

$$\Re\left\{ j\omega \iiint_V \left(\mu_1 \left|\mathbf{H}\right|^2 + \epsilon_1 \left|\mathbf{E}\right|^2\right) dv \right\} = 0 \tag{4.6}$$

$$P_r = \frac{1}{2}\Re\left\{ -\oiint_{S'} \left(\mathbf{H}^* \cdot \mathbf{M} + \mathbf{E} \cdot \mathbf{J}^*\right) ds' \right\} \tag{4.7}$$

The electric and magnetic fields, $\mathbf{E}$ and $\mathbf{H}$ respectively, due to the scattering of the body can be calculated from the electric and magnetic currents using the expressions shown in eq. (4.8) and eq. (4.9), where $\mathbf{X}$ represents to $\mathbf{J}$ or $\mathbf{M}$, $\mathbf{r}$ represents the observation point, PV represents the principal value of integral, and G_1 is the Green function in the medium 1. Notice that the operators are expressed in a more detailed than introduced in chapter 2.2.

$$\mathbf{E} = \mathcal{K}(\mathbf{M}) - \eta_1 \mathcal{L}(\mathbf{J}) \tag{4.8}$$

$$\mathbf{H} = -\mathcal{K}(\mathbf{J}) - \frac{1}{\eta_1}\mathcal{L}(\mathbf{M}) \tag{4.9}$$

with $\mathcal{L}(\mathbf{X})$ and $\mathcal{K}(\mathbf{X})$ are defined as:

$$\begin{aligned}\mathcal{L}(\mathbf{X}) &= -j\frac{1}{2k_1}\hat{\mathbf{n}}_i \nabla' \cdot \mathbf{X} + jk_1 \left\{ \oiint_{S'} \mathbf{X} G_1(\mathbf{r}, \mathbf{r}') ds' + \frac{1}{k_1^2} \nabla \oiint_{S', PV} \nabla' \cdot \mathbf{X} G_1(\mathbf{r}, \mathbf{r}') ds' \right\} \\ &= -j\frac{1}{2k_1}\hat{\mathbf{n}}_i \nabla' \cdot \mathbf{X} + \mathcal{L}_0(\mathbf{X}) \end{aligned} \tag{4.10}$$

$$\begin{aligned}\mathcal{K}(\mathbf{X}) &= \frac{1}{2}\hat{\mathbf{n}}_i \times \mathbf{X} + \oiint_{S', PV} \mathbf{X} \times \nabla G_1(\mathbf{r}, \mathbf{r}') ds' \\ &= \mathcal{I}_{\hat{\mathbf{n}}_i}(\mathbf{X}) + \mathcal{K}_0(\mathbf{X}) \end{aligned} \tag{4.11}$$

where $\mathcal{L}_0(\mathbf{X})$, $\mathcal{K}_0(\mathbf{X})$ and $\mathcal{I}_{\hat{\mathbf{n}}_i}(\mathbf{X})$ can be obtained respectively from the following expressions.

$$\mathcal{L}_0(\mathbf{X}) = jk_1 \left\{ \oiint_{S'} \mathbf{X} G_1(\mathbf{r}, \mathbf{r}') ds' + \frac{1}{k_1^2} \nabla \oiint_{S', PV} \nabla' \cdot \mathbf{X} G_1(\mathbf{r}, \mathbf{r}') ds' \right\} \tag{4.12}$$

$$\mathcal{K}_0(\mathbf{X}) = \oiint_{S', PV} \mathbf{X} \times \nabla G_1(\mathbf{r}, \mathbf{r}') ds' \tag{4.13}$$

$$\mathcal{I}_{\hat{\mathbf{n}}_i}(\mathbf{X}) = \frac{1}{2}\hat{\mathbf{n}}_i \times \mathbf{X} \tag{4.14}$$

Substituting eqs. (4.8) and (4.9) into eq. (4.7) we obtain the expression shown in eq. (4.15).

$$P_r = \frac{1}{2}\Re \left\{ - \oiint_{S'} \left(\left(-\mathcal{K}(\mathbf{J}) - \frac{1}{\eta}\mathcal{L}(\mathbf{M}) \right)^* \cdot \mathbf{M} + (-\eta \mathcal{L}(\mathbf{J}) + \mathcal{K}(\mathbf{M})) \cdot \mathbf{J}^* \right) ds' \right\} \tag{4.15}$$

In order to simplify the expressions, eq. (4.15) is splitted into equations (4.16)-(4.19).

$$P_r^{(1)} = \frac{\eta}{2}\Re\left\{\oiint_{S'} \mathcal{L}\left(\mathbf{J}\right)\cdot\mathbf{J}^* ds'\right\} \tag{4.16}$$

$$P_r^{(2)} = \frac{1}{2\eta}\Re\left\{\oiint_{S'} \mathcal{L}^*\left(\mathbf{M}\right)\cdot\mathbf{M} ds'\right\} \tag{4.17}$$

$$P_r^{(3)} = \frac{1}{2}\Re\left\{\oiint_{S'} \mathcal{K}^*\left(\mathbf{J}\right)\cdot\mathbf{M} ds'\right\} \tag{4.18}$$

$$P_r^{(4)} = -\frac{1}{2}\Re\left\{\oiint_{S'} \mathcal{K}\left(\mathbf{M}\right)\cdot\mathbf{J}^* ds'\right\} \tag{4.19}$$

It can be noticed that $\mathcal{L}$ operator in equations (4.16)-(4.17) can be substituted by $\mathcal{L}_0$, as the currents are orthogonal to $\hat{\mathbf{n}}$, the normal vector to surface S, so the scalar product only takes values from $\mathcal{L}_0$. Also, using the property $\Re\phi^* = \Re\phi$, terms $P_r^{(2)}$ and $P_r^{(3)}$, eq. (4.17) and eq. (4.18) can be expressed taking the complex conjugate to the right part of the dot product. Applying both changes we arrive to the following expressions:

$$P_r^{(1)} = \frac{\eta}{2}\Re\left\{\oiint_{S'} \mathcal{L}_0\left(\mathbf{J}\right)\cdot\mathbf{J}^* ds'\right\} \tag{4.20}$$

$$P_r^{(2)} = \frac{1}{2\eta}\Re\left\{\oiint_{S'} \mathcal{L}_0\left(\mathbf{M}\right)\cdot\mathbf{M}^* ds'\right\} \tag{4.21}$$

$$P_r^{(3)} = \frac{1}{2}\Re\left\{\oiint_{S'} \mathcal{K}\left(\mathbf{J}\right)\cdot\mathbf{M}^* ds'\right\} \tag{4.22}$$

$$P_r^{(4)} = -\frac{1}{2}\Re\left\{\oiint_{S'} \mathcal{K}\left(\mathbf{M}\right)\cdot\mathbf{J}^* ds'\right\} \tag{4.23}$$

If MoM is applied to discretize the electric and magnetic currents, $\mathbf{J}$ and $\mathbf{M}$ can be expressed as a sum of N basis functions with coefficients J_i and M_i, with $i = 1 \ldots N$, as shown in equations (4.24) and (4.25).

$$\mathbf{J}(\mathbf{r}') = \sum_{i=1}^{N} J_i \mathbf{f}_i(\mathbf{r}') \tag{4.24}$$

$$\mathbf{M}(\mathbf{r}') = \sum_{i=1}^{N} M_i \mathbf{f}_i(\mathbf{r}') \tag{4.25}$$

Then, the first term of the real radiated power $P_r^{(1)}$ can be expressed as in eq. (4.26).

$$\begin{aligned} P_r^{(1)} &= \frac{\eta}{2}\Re\left\{ \oiint_{S'} \mathcal{L}_0\left(\sum_{i=1}^{N} J_i \mathbf{f}_i(\mathbf{r}')\right) \cdot \left(\sum_{j=1}^{N} J_j \mathbf{f}_j(\mathbf{r}')\right)^* ds' \right\} \\ &= \frac{\eta}{2}\Re\left\{ \sum_{i=1}^{N} J_i \sum_{j=1}^{N} J_j^* \oiint_{S'} \mathcal{L}_0\left(\mathbf{f}_i(\mathbf{r}')\right) \cdot \mathbf{f}_j^*(\mathbf{r}') ds' \right\} \\ &= \frac{\eta}{2}\Re\left\{ \sum_{j=1}^{N} J_j^* \sum_{i=1}^{N} J_i \oiint_{S'} \mathcal{L}_0\left(\mathbf{f}_i(\mathbf{r}')\right) \cdot \mathbf{f}_j^*(\mathbf{r}') ds' \right\} \end{aligned} \tag{4.26}$$

This can be expressed in matrix notation as shown in eq. (4.27), where $J = \{J_i\}_{i=1\ldots N}$ and $\mathbf{Q}^{(1)}$ the $N \times N$ matrix, defined in eq. (4.28).

$$P_r^{(1)} = \Re\{J^H \mathbf{Q}^{(1)} J\} \tag{4.27}$$

$$Q_{i,j}^{(1)} = \frac{\eta}{2} \oiint_{S'} \mathcal{L}_0\left(\mathbf{f}_i(\mathbf{r}')\right) \cdot \mathbf{f}_j^*(\mathbf{r}') ds' \tag{4.28}$$

Following the same procedure, the other terms can be obtained as shown in equations bellow:

$$P_r^{(1)} = \Re\{J^H \mathbf{Q}^{(1)} J\} = \Re\{J^H \mathbf{A} J\} \tag{4.29}$$

$$P_r^{(2)} = \Re\{M^H \mathbf{Q}^{(2)} M\} = \Re\{M^H \mathbf{B} M\} = \Re\{M^H \frac{\mathbf{A}}{\eta^2} M\} \tag{4.30}$$

$$P_r^{(3)} = \Re\{M^H \mathbf{Q}^{(3)} J\} = \Re\{M^H \mathbf{C} J\} \tag{4.31}$$

$$P_r^{(4)} = \Re\{J^H \mathbf{Q}^{(4)} M\} = \Re\{J^H \mathbf{D} M\} = \Re\{J^H (-\mathbf{C}) M\} \tag{4.32}$$

Where $\mathbf{Q}^{(i)}$ are defined as:

$$Q_{i,j}^{(1)} = \frac{\eta}{2} \oiint_{S'} \mathcal{L}_0 \left(\mathbf{f}_i(\mathbf{r}')\right) \cdot \mathbf{f}_j^*(\mathbf{r}') ds' \tag{4.33}$$

$$\mathbf{Q}^{(2)} = \frac{1}{\eta^2}\mathbf{Q}^{(1)} \tag{4.34}$$

$$Q_{i,j}^{(3)} = \frac{1}{2} \oiint_{S'} \mathcal{K} \left(\mathbf{f}_i(\mathbf{r}')\right) \cdot \mathbf{f}_j^*(\mathbf{r}') ds' \tag{4.35}$$

$$\mathbf{Q}^{(4)} = -\mathbf{Q}^{(3)} \tag{4.36}$$

Introducing the property $\Re\phi = \frac{1}{2}(\phi + \phi^*)$ we can obtain

$$\begin{aligned} P_r &= P_r^{(1)} + P_r^{(2)} + P_r^{(3)} + P_r^{(4)} = \\ &= \frac{1}{2}\Big\{ J^H \mathbf{A} J + J^H \mathbf{A}^H J + M^H \mathbf{B} M + M^H \mathbf{B}^H M + \\ &\quad + M^H \mathbf{C} J + J^H \mathbf{C}^H M + J^H(-\mathbf{C}) M + M^H(-\mathbf{C}^H) J \Big\} \\ &= \frac{1}{2}\Big\{ J^H(\mathbf{A} + \mathbf{A}^H) J + M^H(\mathbf{B} + \mathbf{B}^H) M + \\ &\quad + M^H(\mathbf{C} - \mathbf{C}^H) J + J^H(-\mathbf{C} + \mathbf{C}^H) M \Big\} \\ &= J^H \mathbf{A}^R J + M^H \frac{\mathbf{A}^R}{\eta^2} M + M^H \mathbf{C}^I J - J^H \mathbf{C}^I M \end{aligned} \tag{4.37}$$

where $\mathbf{A}^R = \mathbf{A} + \mathbf{A}^H$ and $\mathbf{C}^I = \mathbf{C} - \mathbf{C}^H$. Considering the $2N \times 1$ column vector

$$I = \begin{bmatrix} J \\ M \end{bmatrix} = [J_1, J_2, \ldots, J_N, M_1, M_2, \ldots, M_N]^T$$

where $(\cdot)^T$ denotes transposed, we define the $2N \times 2N$ matrix

$$\mathbf{G} = \begin{bmatrix} \mathbf{A}^R & -\mathbf{C}^I \\ \mathbf{C}^I & \frac{1}{\eta^2}\mathbf{A}^R \end{bmatrix} = \begin{bmatrix} \mathbf{A}^R & (\mathbf{C}^I)^H \\ \mathbf{C}^I & \frac{1}{\eta^2}\mathbf{A}^R \end{bmatrix} \tag{4.38}$$

where $(\cdot)^H$ denotes hermitic and the elements of $\mathbf{A}^R$ and $\mathbf{C}^I$ are:

$$A_{i,j}^R = \eta \Re \left\{ \oiint_{S'} \mathcal{L}_0 \left(\mathbf{f}_i(\mathbf{r}')\right) \cdot \mathbf{f}_j^*(\mathbf{r}') ds' \right\} \tag{4.39}$$

$$C_{i,j}^I = \frac{1}{2} \left[\oiint_{S'} \mathcal{K} \left(\mathbf{f}_i(\mathbf{r}')\right) \cdot \mathbf{f}_j^*(\mathbf{r}') ds' - \oiint_{S'} \mathcal{K}^* \left(\mathbf{f}_j(\mathbf{r}')\right) \cdot \mathbf{f}_i(\mathbf{r}') ds' \right]. \tag{4.40}$$

It must be taken into account that despite of $\mathcal{L}_0$ operator being symmetric when Galerkin ponderation it is used, the $\mathcal{K}$ operator does not satisfy that same property. In particular, in eq. (4.11), the $\mathcal{K}_0$ operator is symmetric, shown in eq. (4.41), but the $\mathcal{I}_{\hat{\mathbf{n}}_i}$ operator is antisymmetric, as shown in eq. (4.42).

$$\oiint_{S'} \mathcal{K}_0\left(\mathbf{f}_i(\mathbf{r}')\right) \cdot \mathbf{f}_j^*(\mathbf{r}')ds' = \oiint_{S'} \mathcal{K}_0\left(\mathbf{f}_j(\mathbf{r}')\right) \cdot \mathbf{f}_i^*(\mathbf{r}')ds' \tag{4.41}$$

$$\oiint_{S'} \mathcal{I}_{\hat{\mathbf{n}}_i}\left(\mathbf{f}_i(\mathbf{r}')\right) \cdot \mathbf{f}_j^*(\mathbf{r}')ds' = -\oiint_{S'} \mathcal{I}_{\hat{\mathbf{n}}_i}\left(\mathbf{f}_j(\mathbf{r}')\right) \cdot \mathbf{f}_i^*(\mathbf{r}')ds' \tag{4.42}$$

Based on this, the elements of $\mathbf{C}_I$ can be calculated as expressed in eq. (4.43), where the first term in the right part of the equation is pure imaginary and the second term is pure real. This real part only takes values in a few elements, where the original base are overlapped.

$$C_{i,j}^I = j\Im\left\{\oiint_{S'} \mathcal{K}_0\left(\mathbf{f}_i(\mathbf{r}')\right) \cdot \mathbf{f}_j^*(\mathbf{r}')ds'\right\} + \oiint_{S'} \mathcal{I}_{\hat{\mathbf{n}}_i}\left(\mathbf{f}_i(\mathbf{r}')\right) \cdot \mathbf{f}_j^*(\mathbf{r}')ds' \tag{4.43}$$

It is important to notice that the second term of $C_{i,j}^I$ in eq. (4.43) is a real term. Because of this property the total contribution to the total real radiated power is zero, resulting:

$$\begin{bmatrix} J^H M^H \end{bmatrix} \begin{bmatrix} 0 & \Re\{\mathbf{C}_I\} \\ -\Re\{\mathbf{C}_I\} & 0 \end{bmatrix} \begin{bmatrix} J \\ M \end{bmatrix} = -M^H \Re\{\mathbf{C}_I\} J + J^H \Re\{\mathbf{C}_I\} M \tag{4.44}$$

$$= -M^H \Re\{\mathbf{C}_I\} J + \left(\left(J^H \Re\{\mathbf{C}_I\} M\right)^H\right)^H = \tag{4.45}$$

$$- M^H \Re\{\mathbf{C}_I\} J + \left(M^H \left(\Re\{\mathbf{C}_I\}\right)^T J\right)^* = -M^H \Re\{\mathbf{C}_I\} J - \left(M^H \Re\{\mathbf{C}_I\} J\right)^* \tag{4.46}$$

Finally, the scattered power by the body enclosed by S can be expressed as in eq. (4.47), where $\mathbf{G}$ is a $2N \times 2N$ matrix that describes the electromagnetic power radiated by the body.

$$P_r = I^H \mathbf{G} I \tag{4.47}$$

This matrix is hermitian and positive semidefinite. Since $\mathbf{A}^R$ is real and symmetric as consequence of the properties of $\mathcal{L}$, $\mathbf{G}$ meets that $G^H = G$. Altough the demonstration of the semidefinite positive property is not trivial, is easy to prove due that

power is a positive physical magnitude, due this, radiated power can be expressed as eq. (4.47).

4.2.2 Macrobasis generation

Applying a singular value decomposition (SVD) over $\mathbf{G}$ results in decomposition of $\mathbf{G}$ shown in eq. (4.48), where where $\mathbf{U}$ and $\mathbf{V}$ are unitary $2N \times 2N$ matrices and Σ is a real positive diagonal matrix, $\Sigma = diag\{\sigma_1, \sigma_2, \ldots, \sigma_{2N}\}$.

$$\mathbf{G} = \mathbf{U}\Sigma\mathbf{V}^H \tag{4.48}$$

Since $\mathbf{G}$ is hermitian, $\mathbf{U}$ and $\mathbf{V}$ are orthonormal and is met $\mathbf{U} = \mathbf{V}$. Then, eq. (4.48) can be expressed as in eq. (4.49).

$$\mathbf{G} = \mathbf{U}\Sigma\mathbf{U}^H \tag{4.49}$$

Using the decomposition of eq. (4.49) in (4.47), the radiated power by the scattered fields can be obtained as expressed in eq. (4.50).

$$P_r = I^H\mathbf{G}I = I^H\mathbf{U}\Sigma\mathbf{U}^H I \tag{4.50}$$

Now, a new set of basis functions as the combination of the vector I can be expressed as $I = \mathbf{U}\bar{I}$. This new set of basis functions are macrobasis functions, and is composed by the columns of $\mathbf{U}$. Introducing this into eq. (4.50), results in eq. (4.51).

$$P_r = I^H\mathbf{G}I = \bar{I}^H\mathbf{U}^H\mathbf{U}\Sigma\mathbf{U}^H\mathbf{U}\bar{I} \tag{4.51}$$

Using the orthonormal property of the SVD for the $\mathbf{U}$ and $\mathbf{V}$ matrices, i.e. $\mathbf{U}^{-1} = \mathbf{U}^H$, the expression (4.52) is obtained, which represents the power radiated by the macrobasis given by $\bar{I}$.

$$P_r = \bar{I}^H\Sigma\bar{I} \tag{4.52}$$

From equation (4.52) derives the following important properties:

- The power radiated by the ith-macrobase is σ_i, i.e. if

$$\bar{I}_j = \begin{cases} 1, & \text{if } j = i \\ 0, & \text{otherwise} \end{cases}$$

  the power radiated by the body is σ_i.

- The radiated power by base i is the ith-term of diagonal matrix Σ multiplied by the square magnitude of this basis $\bar{I}_i$, i.e. $|\bar{I}_i|^2\sigma_i$

$$P_r = \bar{I}^H \Sigma \bar{I} = \sum_{i=1}^{2N} \sigma_i |\bar{I}_i|^2 = \sum_{i=1}^{2N} \{P_r\}_i \tag{4.53}$$

- As the macrobasis functions are generated by SVD, the set is shorted by power radiated in decreasing order:

$$\sigma_1 \geq \sigma_2 \geq \sigma_3 \geq \ldots \geq \sigma_{2N-1} \geq \sigma_{2N}$$

- The set of macrobasis functions are completely independent of the excitation of the problem, as well as the constitutive properties of the body. By contrast, the set presents dependence on the geometry, the frequency and the constitutive parameter of the lossless outer medium.

In addition to the above, matrix $\mathbf{G}$, and therefore matrix Σ, are, in general, very ill conditioned, hence

$$\sigma_i \ll \sigma_1 \text{ beyond certain } m < i$$

in consequence, only few macrobasis concentrate the total radiated power by the object. The rest of the set do not contribute significantly to the radiated energy and can be removed for radiation purposes. However, despite of not being relevant for the radiated energy, these macrobasis have play an important role in the reactive fields, which enforces to take them into account for the self-coupling or the near-field area.

In Fig. 4.2 are represented, for the J and M surface currents, some of the firsts macrobasis computed for a sphere of 2λ of diameter suspended in the free space. It can be appreciated that the representations resembles the *radiating modes* of the sphere. Also, related to the radiating modes, it can be observe how as the macrobase index increases also increases the variability of the macrobase over the body, which is consistent with the reactivity related to the higher index macrobasis.

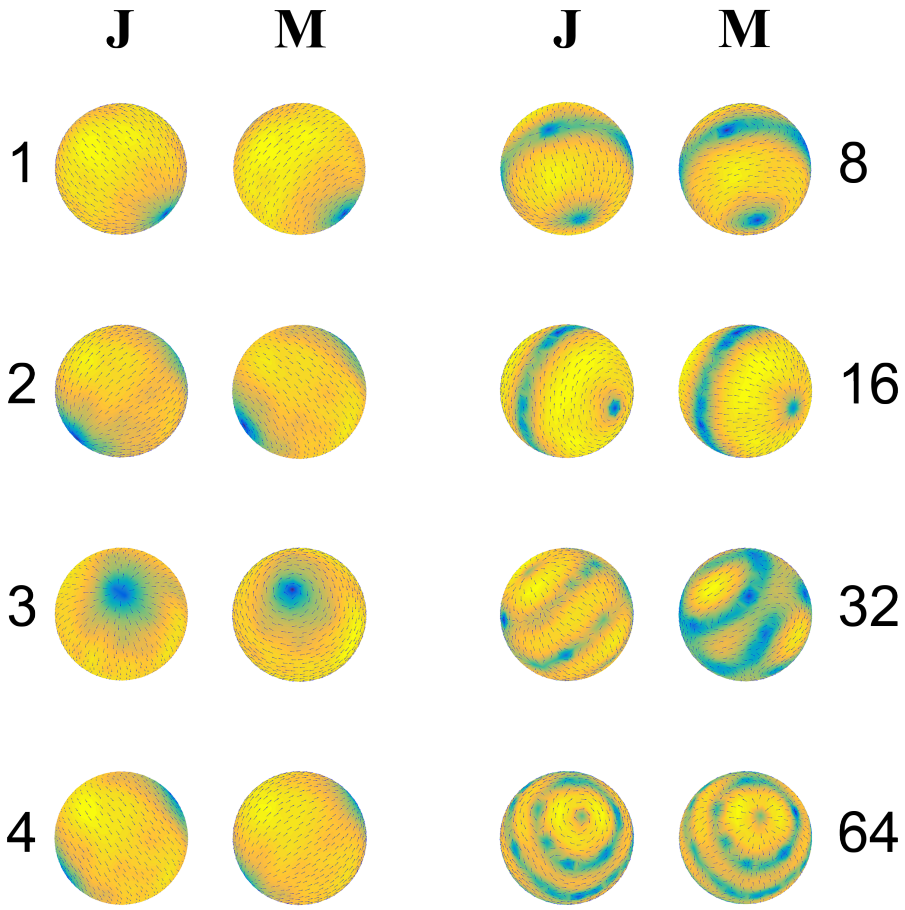

Figure 4.2: Representation of several low-order macrobasis computed for a dielectric sphere of 2λ of diameter for both electric and magnetic surface currents.

4.2.3 Macrobasis representativeness

As stated, due to the characteristics of the macrobasis, in combination with the process of its generation through SVD, the contribution of the basis decreases as the index increases. This can be seen in Fig. 4.3, where the power of each macrobase is represented for multiple geometries by σ_i^2. It can be observed how for all cases the power quickly decreases with the index i. To show the relevancy of the firsts macrobasis over the total, in fig. 4.5 the accumulated power of the firsts i macrobasis over the total power is represented, showing how, in the four cases, the total power is concentrated by the 5% of the macrobasis. Solving these cases of study excited with an incident planewave of λ =550nm to obtain the current distributions with the macrobasis gives place to Fig. 4.4. In this figure it can be appreciated that the dominance of the firsts macrobasis is met.

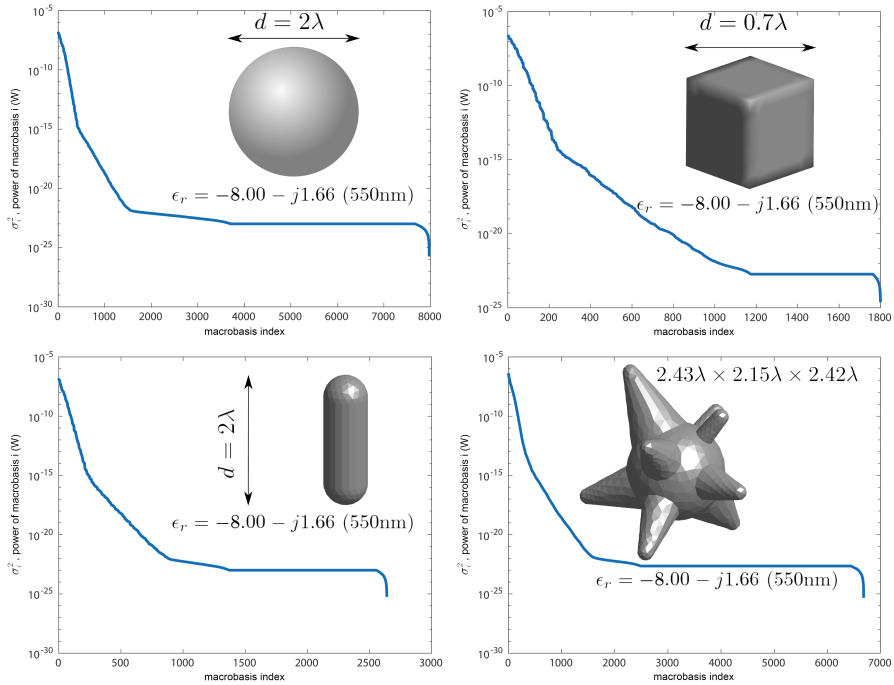

Figure 4.3: Representation of the power of each macrobasis (σ_i^2) for multiple geometries made of gold at 550nm.

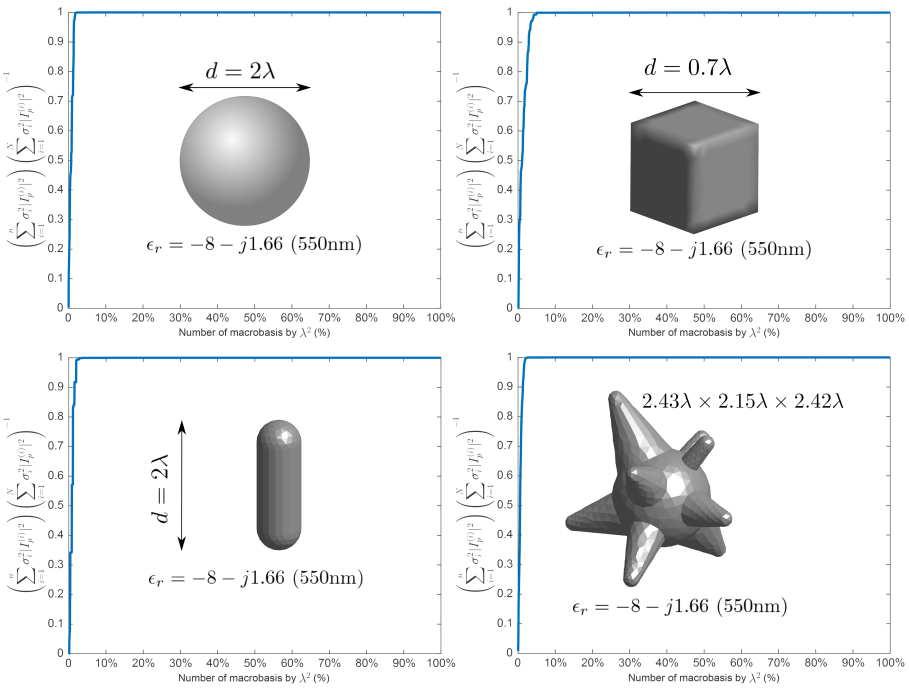

Figure 4.4: Representation of the total power emitted by the first i macrobasis pondered by its corresponding coefficients over the total for multiple geometries made of gold at 550nm.

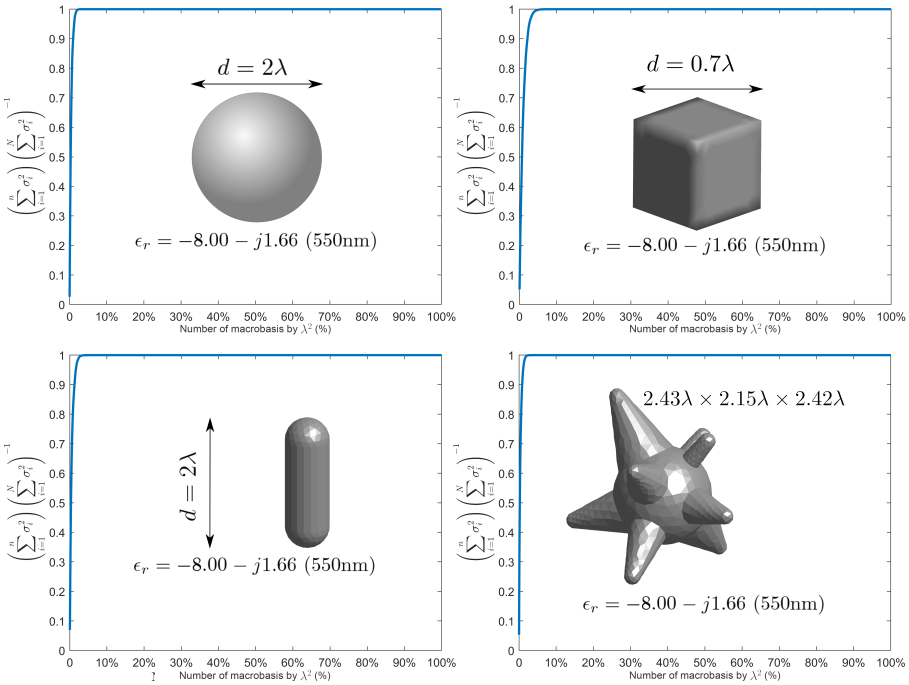

Figure 4.5: Representation of the total power emitted by the first i macrobasis over the total for multiple geometries made of gold at 550nm.

This dominance permits to describe the radiated fields with only few macrobasis, which may make possible to cast aside the high order macrobasis over the 5% of the total as they are not representative for the solution.

Another way to represent the dominance of the low order macrobasis is to use them to compute the scattered field by an object. For this, a sphere made of gold at 550nm of wavelength was solved using SIE-MoM to obtain the external surface current distributions for J and M, using a fraction of the total macrobasis to model the radiation for each case. Figure 4.6 compares the RCS obtained with all the basis and the same case using a 5%, 2.5%, 2% and 1% of the total macrobasis functions to compute the RCS. As it can be observed, for for the two firsts cases there is almost no visible difference between the result in comparison to the complete set of functions. However, it can be appreciated that in the cases of the 2% and 1% setups starts to appear differences, even asymmetries, in the diagram. This would prove that, when the low order macrobasis start to be removed, the total power radiated by the object is no longer properly described.

The last approach to study this phenomenon, through a small practical problem, was to carry out a similar procedure as the previous with a novel method of invisibilization proposed in [89]. This method consist in optimizing through SIE-MoM a filler

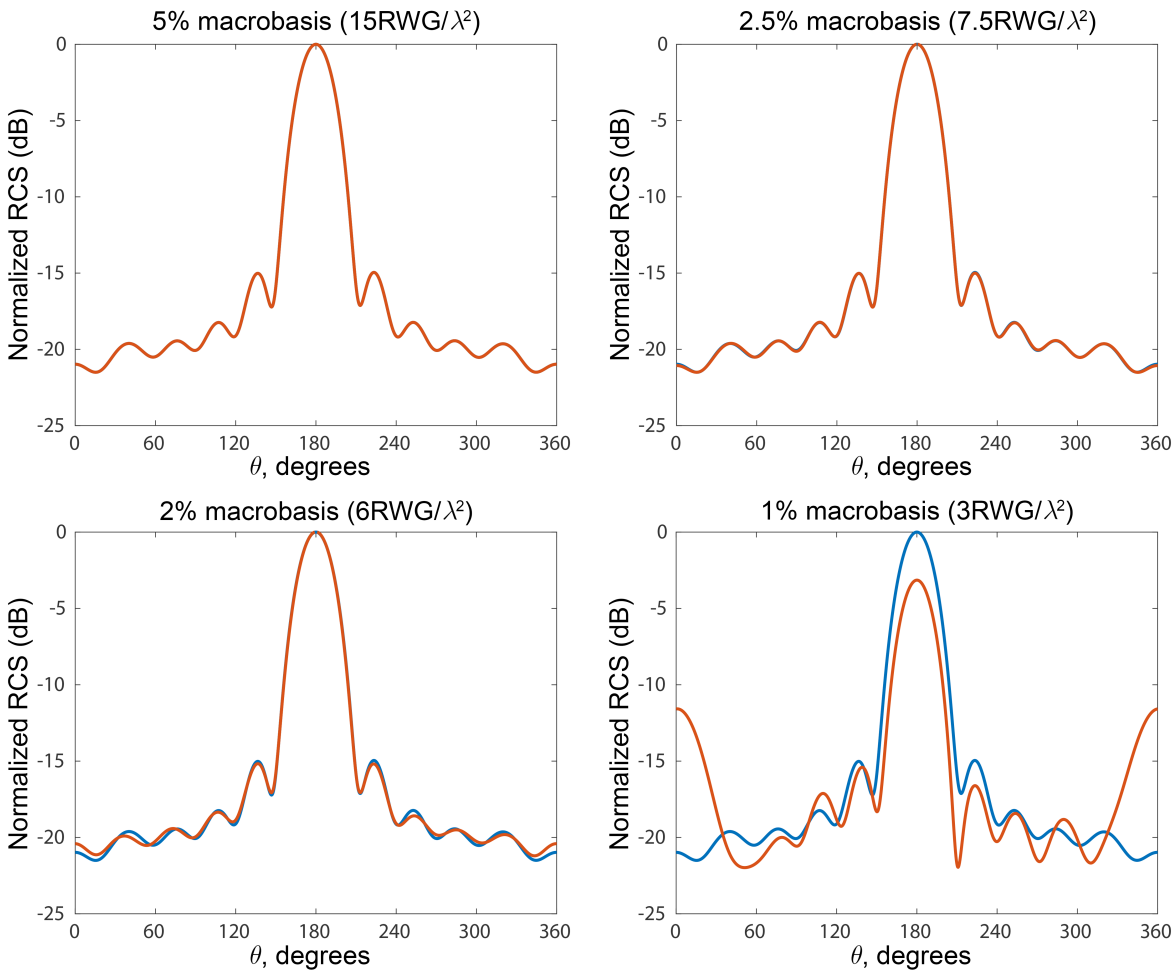

Figure 4.6: Comparison of the normalized RCS of a sphere of 2λ of diameter made of gold $\epsilon_r = -8.00 - j1.66$ at 550nm using different number of macrobasis functions per square wavelength. In blue the RCS with all the basis, in red the resulting RCS partially using the set of macrobasis.

for hollow objects with a set of layers of homogeneous materials with specific constitutive parameters and thicknesses. The purpose of doing this is to reduce the scattering cross section of the object so it becomes invisible. In particular, the case of a hollow sphere of $\lambda/2$ of diameter was studied and an thickness of 0.05λ. The sphere is made of silica ($\epsilon_r = 2.1756 - j2.36 \cdot 10^{-7}$ in the optical regime [90]). The resulting constitutive parameters and thicknesses used for the invisible filler of three layers are ϵ_{r1} =10.39, μ_{r1} =9.20, ϵ_{r2} =-13.50, μ_{r2} =-7.48, ϵ_{r3} =4.96, μ_{r3} =4.30 from the most external layer to the central one, with thicknesses of t_1 =0.0598λ and t_2 =0.0698λ. Figure 4.7(a) shows a comparison of the coefficients obtained for both cases for the external interface (in contact with the medium where the object is suspended). In the left the complete range is represented, where it can be appreciated that both cases are similar in the whole range except in the origin. In the right, the coefficients of the first macrobasis are represented in order to have a better visualization of them.

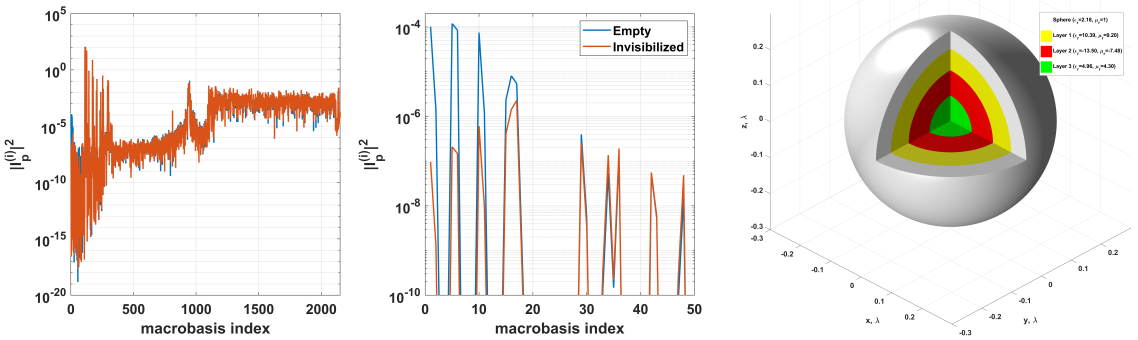

(a) Power emitted by macrobasis. (b) Object.

Figure 4.7: Representation of the invisibilized object and comparison of the power emitted by the macrobasis of the object and the object invisibilized.

It can be appreciated that in the case of the firsts macrobasis there is a relevant reduction in the power emitted, which agrees with what was expected from the statement on the radiation dominance, as the invisibilized object presents presents less radiated power dependent on these macrobasis. In Fig. 4.8 the scattering diagrams for both cases, where is can observed that, in effect, the scattering cross section is minor in the case that presents the lower contribution of the first macrobasis.

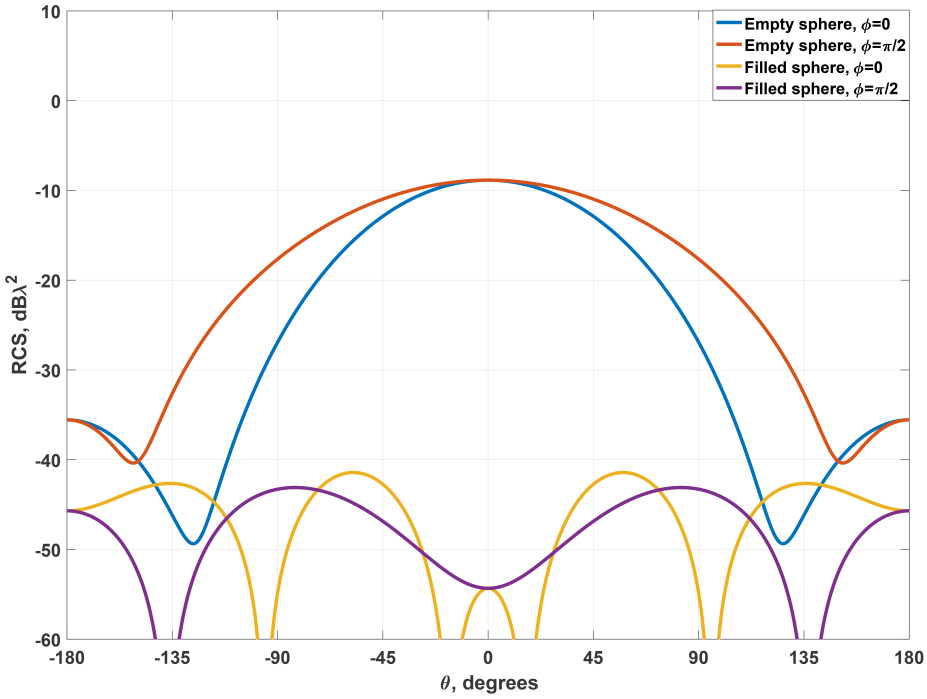

Figure 4.8: Comparison of the RCS for hollow sphere made of silica with $\lambda/2$ of diameter and the same sphere with a multilayer dielectric filler for invisibilizating it.

Finally, to prove the behavior of the macrobasis in the near-field, two cases were studied. In particular, the RCS was computed for two arrays of 3×3 gold spheres of 2λ of diameter. The solution was carried with SIE-MoM for the reference and using SIE-MoM with the firsts macrobasis for the near coupling in radiation between elements. The first one, shown in Fig. 4.9(a), has a separation of 4λ between the centers of the spheres, and the second one, shown in Fig. 4.9(b), a separation of 2.5λ. In both cases it can be appreciated the agreement of both curves, which implies that even in the near field with close distances, where the high order macrobasis has a relevant contribution to the reactive field, the low order macrobasis still work.

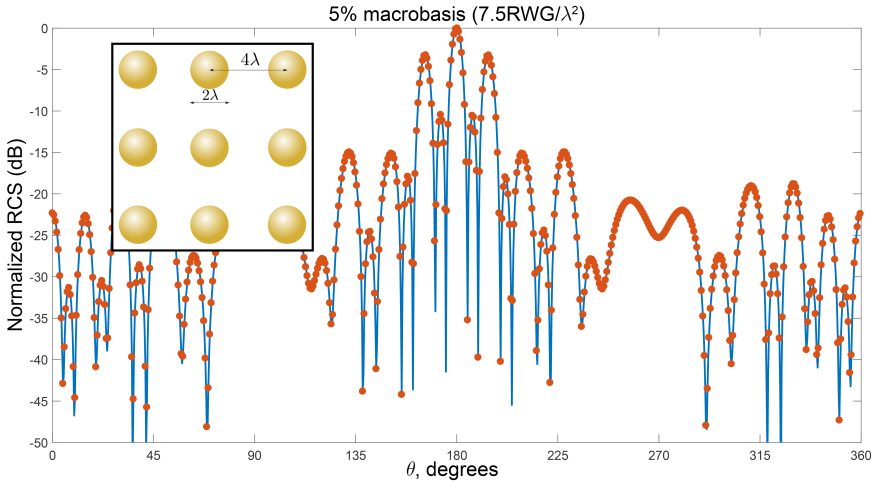

(a) 4λ of separation between centers.

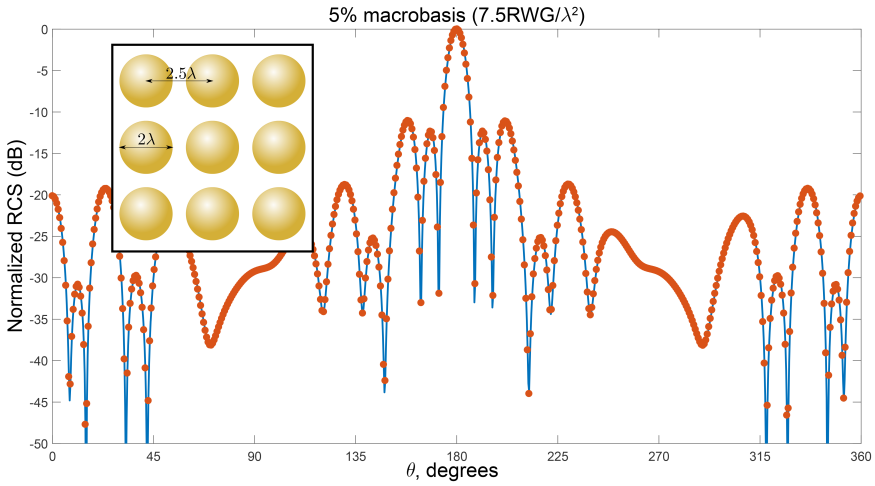

(b) 2.5λ of separation between centers.

Figure 4.9: Comparison of the normalized RCS of arrays of 3×3 spheres of 2λ of diameter with different separations made of gold ($\epsilon_r = -8.00 - j1.66$) at 550nm obtained with complete SIE-MoM and SIE-MoM with a partial set of macrobasis.

4.3 Skeletonization scheme

The work performed with the skeletonization scheme shown in this thesis was performed in Autumn of 2018, in a research visit at the Politecnico di Torino held by the Laboratory of Advanced Computational Electromagnetics (LACE). The base code used for the skeletons generation and ID were developed by Mario Echeverri in his PhD Thesis [91].

The skeletonization scheme is based on the identification of the dominant basis functions over the radiation of a discretized body. For this, the method departs from a matrix $\mathbf{Z}_s$, which contains the components of the electric field generated by each base function. To perform the testing for the sampling of the field process a Dirac deltas vector is used. Then, the electric field is calculated over a proxy surface [92] that encloses the object, which typically is shaped as a cube or a sphere [93, 94]. As result of this process $\mathbf{Z}_s$ contains $3Q \times n$ elements, being Q the number of points used to sample the electric field over the proxy surface. In Fig. 4.10 a representation of the $\mathbf{Z}_s$ matrix obtained for a cube is shown. By playing attention some rows of the matrix stands out over the rest, which generate higher levels of electric field over the proxy surface, i.e. rows #3, #8, #12, #15 and #17.

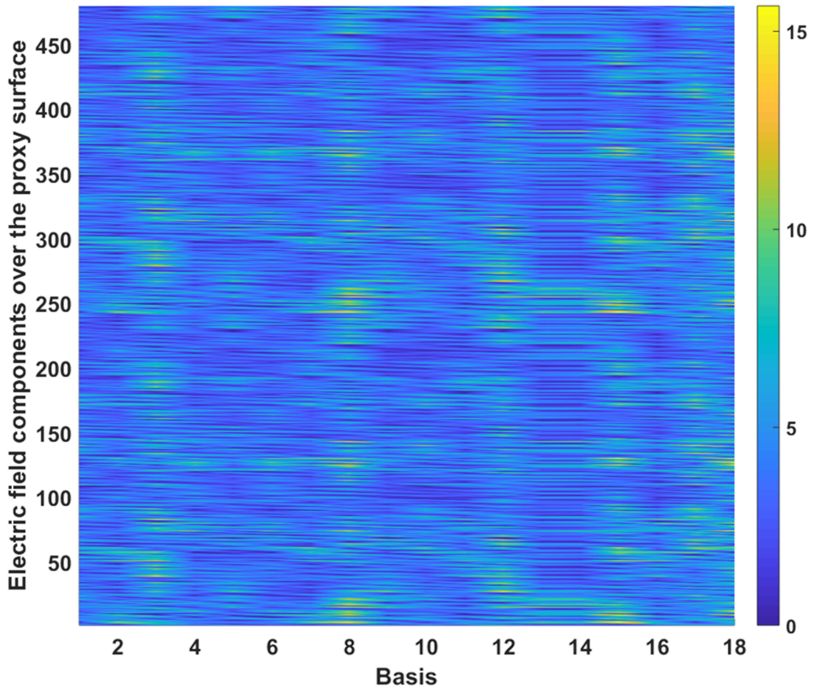

Figure 4.10: Representation of the $\mathbf{Z}_s$ matrix for a cube with 18 RWG basis.

Once $\mathbf{Z}_s$ is obtained the next step is to use it as input for the ID method [79] with a tolerance. This tolerance works as a threshold for the error allowed, being the difference between the electric field contribution of all the basis compared to the dominant ones (the magnetic field can be used too). Based on the data in $\mathbf{Z}_s$, which is rank deficient, and the tolerance, the ID method identify the dominant basis and then generates the skeletons, this is $\mathbf{U}$ and $\mathbf{V}$ interpolation and anterpolation matrices respectively, which permit to extract the dominant basis from $\mathbf{Z}$, and a list with the indexes of the dominant basis. Due to reciprocity, is meet that $\mathbf{V} = \mathbf{U}^T$. In Fig. 4.11 is shown the setup to apply ID to a nanorod made of gold at λ =550nm using a proxy surface with 180 points (left) and the dominant basis identified by interpolative method with a tolerance of 0.001, achieving a compression rate (CR) of 87.6%

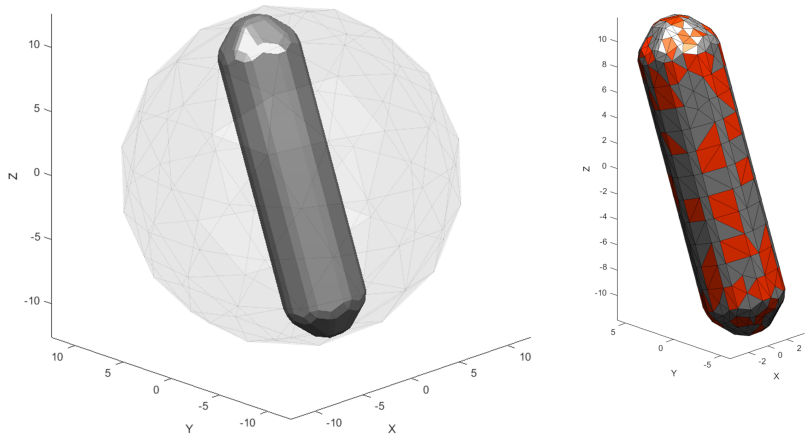

Figure 4.11: Representation of a nanorod and its associated proxy surface with 180 points (left) and its dominant basis after applying the skeletonization process with a tolerance of 0.001, achieving a compression rate of 87.6%.

Then, the complete problem can be decomposed as shown in in Fig. 4.12, where Z is a dense matrix, U and V^T are the interpolative and anterpolative matrices, Z_{NF} is the full ranks sub-blocks of Z for the near-field, and Z_{FF} is the full rank sampled version of Z for the far-field.

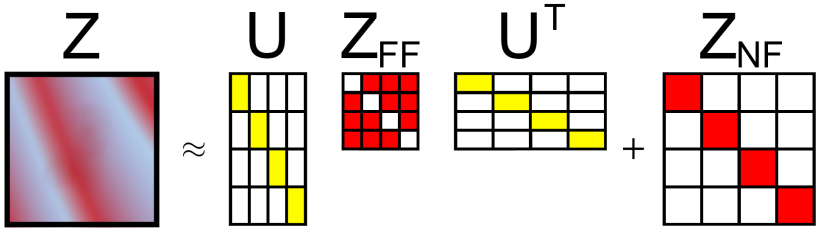

Figure 4.12: Representation of the matrices of the skeleton scheme generated by the interpolative decomposition.

4.4 Integration of matrix compression methods into slotFFT

In this section we explain the way that the matrix compression methods are integrated in the slotFFT algorithm, and the requirements that must be met for it. The integration described is valid for both versions of slotFFT. Prior to the description how this is done, it must be taken into account that slotFFT deal with the $\mathbf{z}_{i,j}$ sub-blocks that describes the coupling between elements with the same relative position of $\mathbf{Z}$ separately.

If a method is able to compress a sub-block $\mathbf{z}_{i,j}$ with independence of the other coupling sub-blocks then is suitable to be integrated into slotFFT. This is due to the fact that compression is performed directly to the $\mathbf{z}_{i,j}$ sub-blocks before being handled by slotFFT in the same way as an uncompressed sub-block would be processed. In spite of this, other methods that make use of especial features like junctions, overlapping regions or similar approaches may be integrable, but some modifications may be needed to be developed into slotFFT.

In general terms, all methods capable of performing the matrix compression as shown in eq. (4.54) are integrable into slotFFT algorithm, where $\tilde{\mathbf{z}}_{i,j}$ is the compressed coupling sub-block between elements *i,j*, $\mathbf{z}_{i,j}$ is the coupling sub-block between elements *i,j* which is going to be compressed and U and V the interpolation and anterpolation matrices respectively, which are completely independent of any combination of *i,j*.

$$\tilde{\mathbf{z}}_{i,j} = \mathbf{U}\mathbf{z}_{i,j}\mathbf{V} \tag{4.54}$$

It must be taken into account that due to the limitation for these methods compressing the emission and reception for the near field, the self-coupling sub-block never is compressed. In order to perform this in the integration, the coefficients associated to this sub-block are set to zero in the matrix used by slotFFT. Then, it is stored separately, so its contribution is computed for each element and added to the solution at the end of the MVP. If the example is especially dense, i.e. a SERS substrate, the same can be performed for additional sub-blocks. However, doing this operation for additional sub-blocks ends in a relevant reduction of the speed-up achievable due to the increment of the operations and memory accesses. In the case of this thesis, the compression methods that were integrated (as two separated approaches) are the macrobasis described in 4.2, applied to PEC and dielectric problems, and the skeletons scheme introduced in 4.3, applied only to PEC problems, in both cases leaving uncompressed only the self-coupling sub-block.

In the case of the macrobasis, the method has been applied for transmission and

reception. This approach has proven to work well when using the PMCHWT formulation, but has presented precision problems with other formulations.

One of the possible causes considered is that the macrobasis are developed for radiating, which may cause that the reception is not properly addressed by the method. The other reason may be related the terms $\hat{\mathbf{n}} \times J$ and $\hat{\mathbf{n}} \times M$ which are nullified by the PMCHWT formulation, which may have impact over the precision of the other methods when using macrobasis for the reception. The exact reason for this has not been figured out during the thesis, which make it an open problem.

4.5 Application and results

The first structure analyzed, using macrobasis and skeletons with PMCHWT formulation, was a canonical plane-shaped array, shown in Fig. 4.13. The structure is composed by 20×20 PEC spheres of $\lambda/6$ radius and separated between centers by $2/3\lambda$. A total of 270 RWG basis functions were used to model the electric surface currents, giving place to $108K$ unknowns for the complete problem. The excitation applied was a linear polarized planewave impinging with $\theta = 180°$ and $\phi = 0°$.

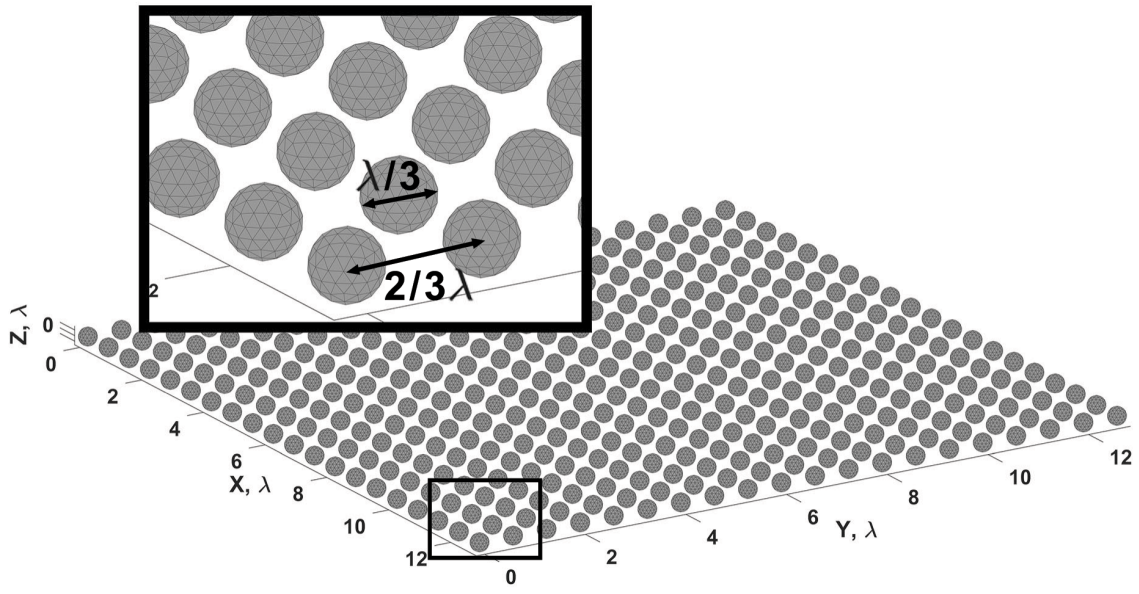

Figure 4.13: Analyzed periodic array, composed by 20×20 PEC spheres of $\lambda/6$ radius separated by $2\lambda/3$.

The firsts results corresponds to the application of the skeletons, using a spherical proxy surface with 180 points for sampling the electric fields and tolerances of 0.1, 0.01

and 0.001 as input for the ID method. These tolerances, combined with the proxy surface used, resulted in CR of 94.07%, 85.90% and 73.50% respectively. It must be taken into account that the CR makes reference to the percentage of basis removed versus the total. As the compression is being performed for emission and reception, the resulting matrix size reduction is $100(1-(1-CR/100)^2)\%$. As result of the resolution of the problem, the RCS diagrams shown in Fig. 4.14 were obtained. In the three cases the solutions almost overlap the reference RCS obtained with slotFFT without any compression applied.

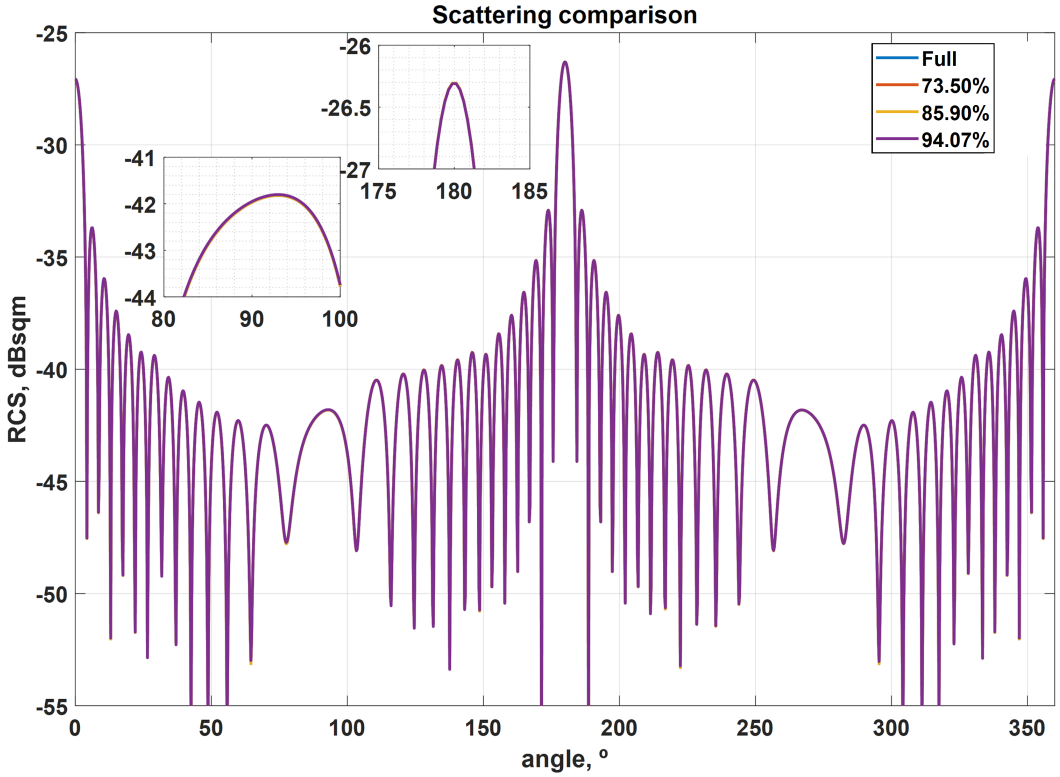

Figure 4.14: Comparison of the scattering diagrams of the proposed setups for the structure shown in Fig. 4.13 using skeletons with the scattering obtained through uncompressed slotFFT.

In Table 4.1 are presented the achieved speed-ups for the three cases, together with the corresponding RMS error over the surface electric currents and the RCS. The definition of the RMS error $\eta(\vec{x}_{ref}, \vec{x}_{approx})$ is shown in (4.55), where $\vec{x}_{ref}$ is the reference signal obtained with slotFFT, $\vec{x}_{approx}$ is the signal obtained through the compression method, and $\|\vec{x}\|$ is the euclidean norm of vector $\vec{x}$. As could be expected, the speed-up presents a direct relation to the compression rate. However, the RMS error, despite of being acceptable, is increased quickly with the compression.

$$\eta(\vec{x}_{ref}, \vec{x}_{approx}) = \frac{\|\vec{x}_{ref} - \vec{x}_{approx}\|}{\|\vec{x}_{ref}\|} \tag{4.55}$$

Table 4.1: Comparison of the speed-up solving the problem through GMRES and error introduced by compression through skeletons in the superficial electric currents and in the RCS for a PEC problem.

Compression rate (%)	Speed-Up	$\eta(J)$	$\eta(RCS)$
73.50	10.22	9.197E-04	9.372E-06
85.90	17.83	2.728E-03	4.316E-05
94.07	23.58	2.133E-02	6.531E-03

The following results were calculated performing compression through macrobasis. The CR used were taken from the ones computed by ID in the previous example in order to compare both methods afterwards, adding an additional value equal to 97.50% to take the method to its limits. The resulting RCS is shown in Fig. 4.15. As in the previous case, all curves show a good agreement with the reference solution, even the case with CR=97.5%, which only differs clearly in lobes with lowest levels and without introducing any asymmetry into the diagram.

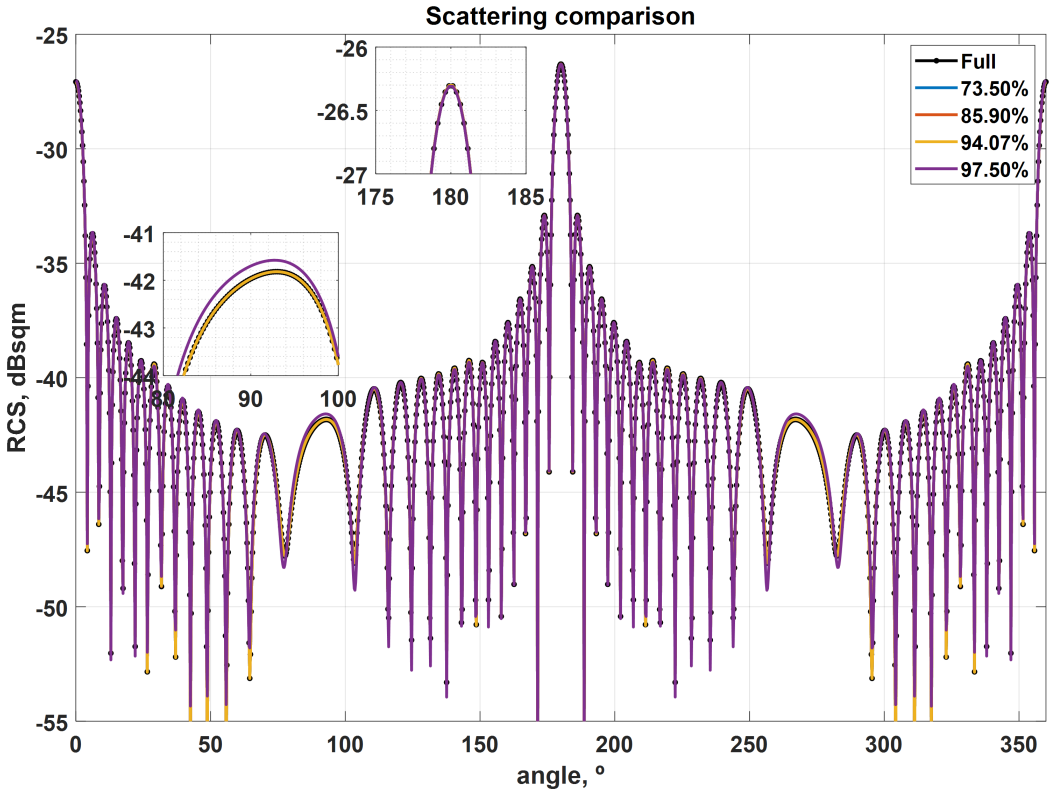

Figure 4.15: Comparison of the scattering diagrams of the proposed setups for the structure shown in Fig. 4.13 using macrobasis with the scattering obtained through uncompressed slotFFT.

Table 4.2 presents the achieved speed-ups achieved for the three cases, together with the corresponding RMS error over the electric currents and the RCS. According to the RCS diagram, the RMS errors in all the cases are acceptable, being the highest the corresponding with the RCS for the CR=97.5%, which is still under a 5%.

Table 4.2: Comparison of the speed-up solving the problem through GMRES and error introduced by compression through macrobasis in the superficial electric currents and in the RCS for a PEC problem.

Compression rate (%)	Speed-Up	$\eta(J)$	$\eta(RCS)$
73.50	10.97	7.929E-04	9.022E-06
85.90	18.17	2.535E-03	2.815E-05
94.07	24.99	1.176E-02	1.106E-03
97.50	26.06	2.386E-02	4.416E-02

The following representation, shown in Fig. 4.16, corresponds to a comparison of the previous RCS diagrams obtained with the skeleton compression (SK) and the macrobasis method (MB).

The Table 4.3 shows a direct comparison of the speed-ups and the RMS error over the surface electric currents and the RCS. Notice that the differences in the speed-up correspond to fluctuation of the machine, as the number of operations required in the MVP for both cases is the same. It can be appreciated that the macrobasis introduces a lower RMS error for the same CR than the skeletons, being this specially noticeable in the RCS.

This can be explained by the fundamentals of the macrobasis functions and its generation, as the macrobasis used are which contribute the most over the total radiation. Also, it must be taken into account that, despite of the compression, every macrobase has a complete set of pondered RWG basis functions in contrast to the skeletons, which completely removes individual basis from the problem. Whereas the amount of information removed may be the same, the sense of that information differs, as the macrobasis method has a *physical sense*.

Table 4.3: Comparison of the speed-up solving the problem through GMRES and error introduced by compression through macrobasis and skeletons in the superficial electric currents and in the RCS for a PEC problem.

Method)	Compression rate (%)	Speed-Up	$\eta(J)$	$\eta(RCS)$
MB	85.90	18.17	2.535E-03	2.815E-05
SK	85.90	17.83	2.728E-03	4.316E-05
MB	94.07	24.99	1.176E-02	1.106E-03
SK	94.07	23.58	2.133E-02	6.531E-03

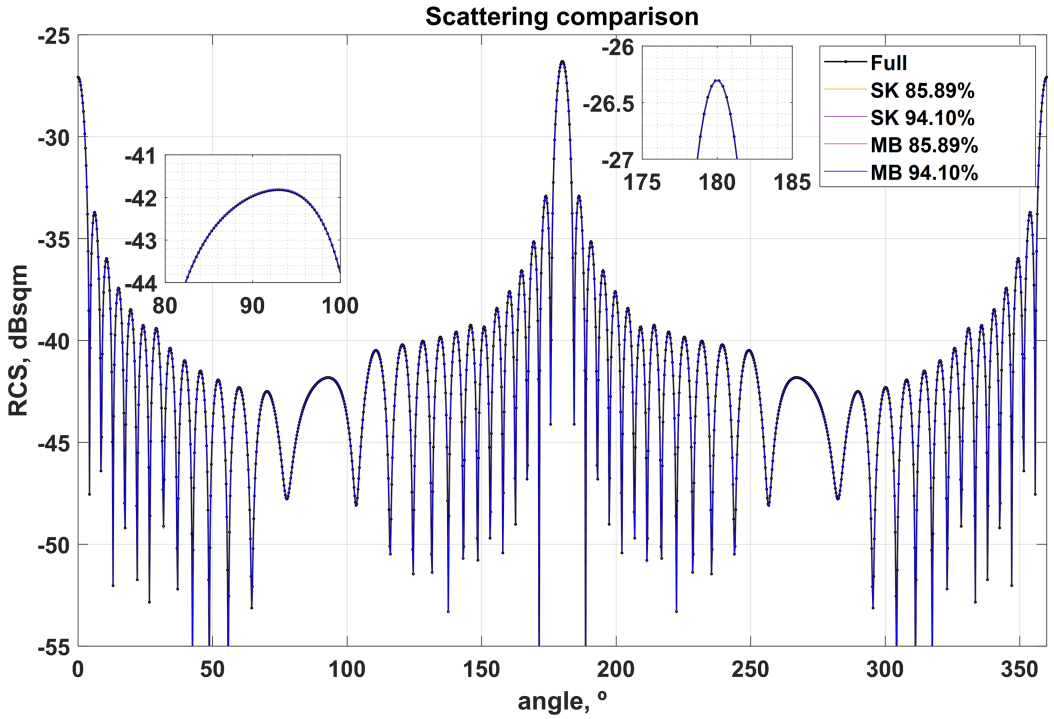

Figure 4.16: Comparison of the scattering diagrams of the proposed setups for the structure shown in Fig. 4.13 using macrobasis and skeletons with the scattering obtained through uncompressed slotFFT.

The next example corresponds to a plane-shaped array composed by 25×25 gold spheres, presented at [84], which it shown in Fig. 4.17. The spheres, with a diameter of λ and a separation between centers of 2λ, are modeled with n =2160 basis functions, resulting in a total of N =1.35 million unknowns for the complete problem, which was analyzed at λ =550nm. The problem, which due to the frequency and the material presents plasmonic behavior, was analyzed using 5 basis/λ^2, 10 basis/λ^2 and 30 basis/λ^2, which correspond to 98.3%, 96.7% and 90.0% CR.

The resulting RCS from the analysis can be seen in Fig. 4.18. It can be appreciated that the effect of the plasmonic behavior has a relevant impact over the solution in comparison to the previous results. However, the agreement for the main lobes is acceptable, specially for the 30 basis/λ^2 case. In Table 4.4 can be found the RMS errors introduced by the compression over the currents and the RCS. As expected from the RCS representation, the RMS error is higher than in the case of the PEC structure. However, it must be taken into account that plasmonic structures are a rough kind of problems in general, so this level of error is expectable as we are dealing with this behavior with a compression method that removes the reactive behavior of the elements (the high order macrobasis) without introducing additional uncompressed coupling sub-block to compensate that deficiency.

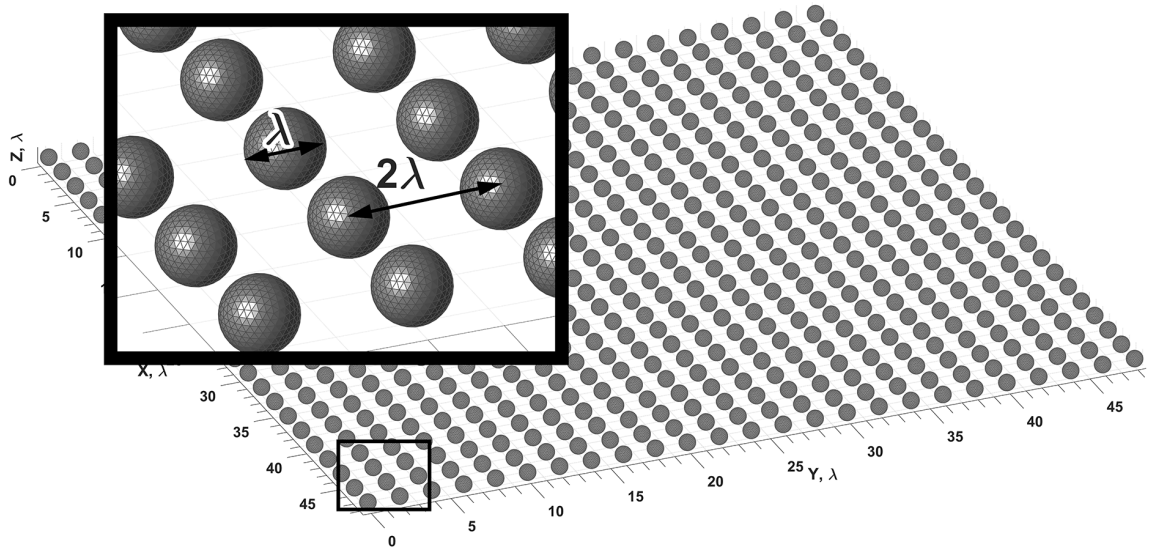

Figure 4.17: Analyzed periodic array, composed by 25×25 gold spheres of λ diameter separated by 2λ.

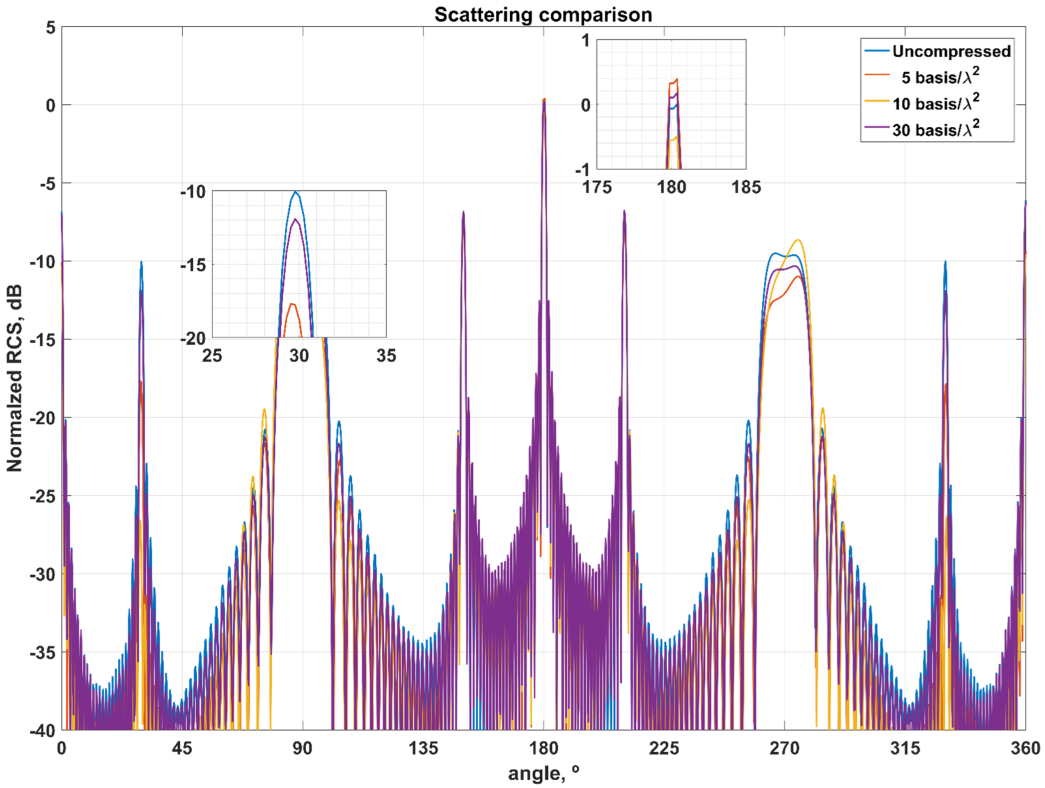

Figure 4.18: Comparison of the scattering diagrams of the proposed setups for the structure shown in Fig. 4.17 using macrobasis with the scattering obtained through uncompressed slotFFT analyzed at λ=550nm ($\epsilon_r = -5.9310 - j2.0971$).

Table 4.4: Comparison of the speed-up solving the structure shown in Fig. 4.18 through GMRES and error introduced by compression through macrobasis in the superficial electric currents and in the RCS for a plasmonic problem.

Compression rate (%)	$\eta(I)$	$\eta(RCS)$
90.0	2.88e-01	1.04e-01
96.7	3.62e-01	2.24e-01
98.3	3.84e-01	2.57e-01

At last, the method was applied to the structure shown un Fig. 3.14, analyzed previously with the double sampling version of slotFFT without performing compression. The setup was the same, but applying a CR of 90%. The obtained RCS is shown in Fig. 4.19. As it can be seen the agreement is relatively closed, being especially good at the main lobe, where the RMS error introduced is lower than 0,05. On the other hand, the speed-up achieved was a factor of x60. This achievable speed-up, represented in Fig. 4.20 through the mean MVP time for two CR levels in comparison to the uncompressed MVP, combined with possibility of improving the error through a slight increment of the macrobasis used, creates the potential for applying slotFFT combined with macrobasis for optimization problems.

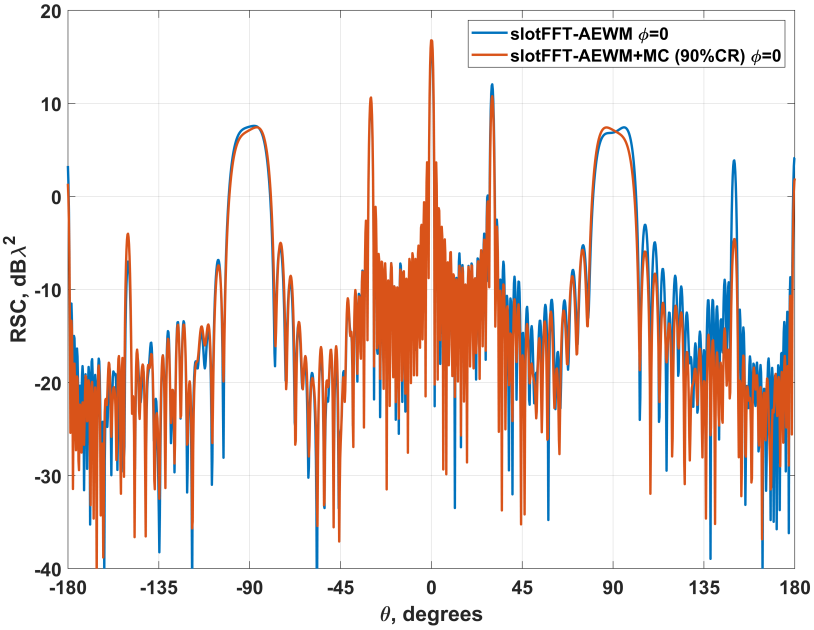

Figure 4.19: Representation of the RCS at $\lambda = 550$nm ($\epsilon_r = -5.9310 - j2.0971$ for gold, $\epsilon_r = -12.9374 - j0.4287$ for silver, $\epsilon_r = -5.6549 - j5.1989$ for cooper and $\epsilon_r = 2.1756 - j2.36e - 7$ for silica) for the uncompressed system and applying a 90% compression rate using macrobasis obtained for the structure shown in Fig. 3.14.

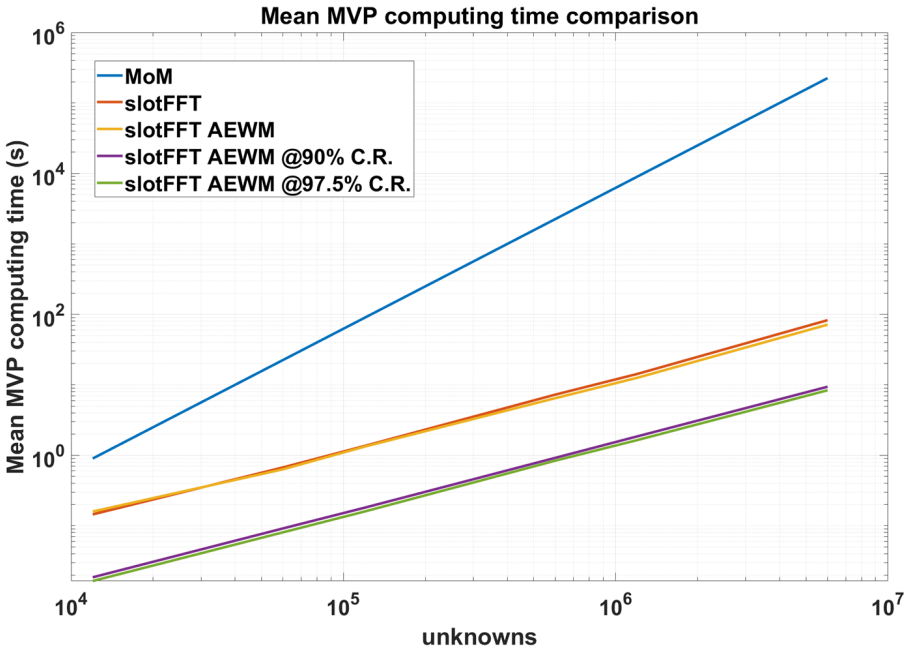

Figure 4.20: MVP computing times for MoM, double sampling slotFFT, double sampling slotFFT for aperiodic element-wise material structures and its compressed versions using 90% and 97.5% compression rates.

4.6 Application of matrix compression for preconditioning periodic problems

This section introduces the use of the introduced framework of the double sampling slotFFT algorithm with compression as a preconditioner. The application of the framework for this purpose was inspired by the application of a limited precision MLFMA as preconditioner [95].

In order to use the integration of slotFFT with matrix compression as preconditioner an auxiliary compressed version of $\mathbf{Z}$ is stored. The computational cost for the coupling sub-blocks for the preconditioner is null, as it is carried out for the main solver. At the same time, the additional memory required is negligible, as the minimal compression rate used for each sub-block reduces the maximum size of them to a 1% of the original size.

Once the setup for the main and the inner solver is finished, the scheme for the framework is the following:

- A main GMRES solver, which computes the MVP with slotFFT using the un-

compressed **Z** and preconditioned with an internal solver.

- An internal GMRES solver which computes the MVP with slotFFT using the compressed **Z** and the uncompressed self-coupling sub-block.
- A block-jacobi preconditioner to improve the convergence of the internal GMRES.

The configuration for the internal solver lies only on the compression level applied. The range of values for this parameter when applied as preconditioner goes from 1% up to a 10% of the total macrobasis. As example of the effectiveness of this preconditioning framework we present the analysis of a canonical structure, shown in Fig. 4.21. The analysis was carried out in a cluster with 4x Intel Xeon E7-8880 v2 processor (15 cores each) and 1TB of RAM memory.

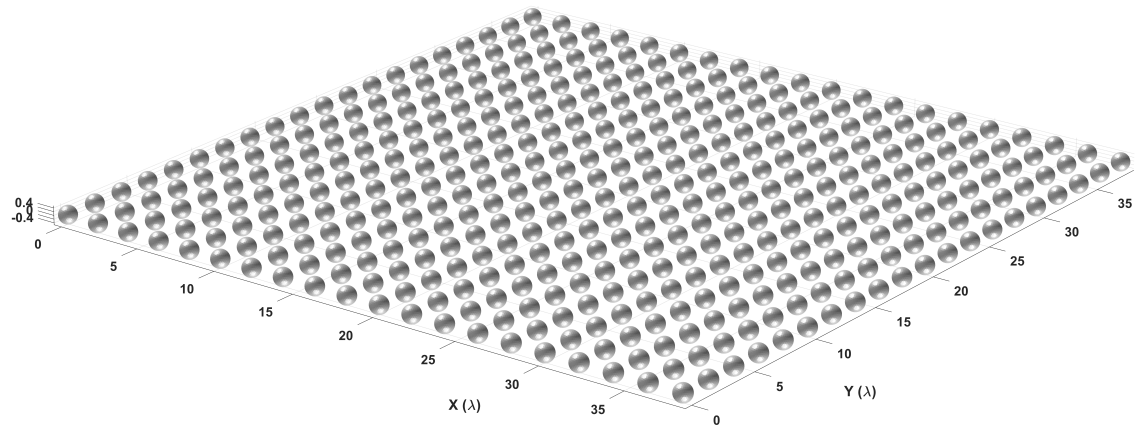

Figure 4.21: Representation of a canonical structure composed of 20×20 spheres of λ diameter and a separation of 2λ between centers.

The structure is surrounded by air and is composed by 20×20 silica spheres ($\epsilon_r = 2.1756 - j2.3600 \cdot 10^{-7}$), with λ of diameter and a separation between centers equals to 2λ. The discretization used 1080 unknowns per sphere to properly model the surface electric and magnetic currents. The setup of the preconditioner for this structure used a 5% of the total macrobasis.

In Fig. 4.22 can be seen how the convergence is improved, going from a total of 83 iterations down to 4 to attain the same residual. This improvement, in terms of total wall-clock time, translates approximately into an x11 speed-up in the solving time with respect to the block-jacobi preconditioning (which used approximately 7 hours for the iterative solver).

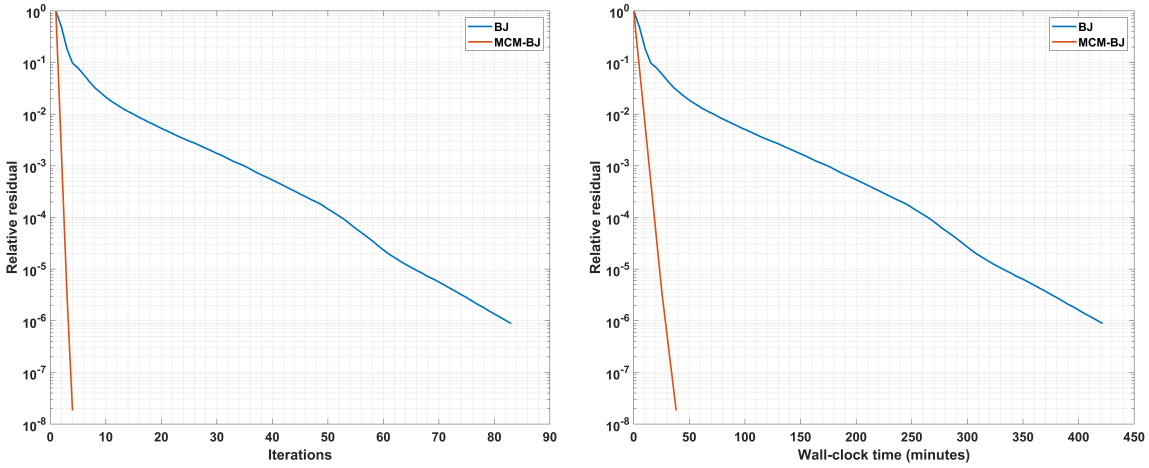

(a) convergence vs. number of iterations.

(b) convergence vs. wall-clock time.

Figure 4.22: Evolution of the convergence vs. number of iterations of the iterative solution of the structure shown in Fig. 4.21 made of silica ($\epsilon_r = 2.1756 - j2.36e-7$ at 550nm) preconditioned with a block-jacobi preconditioner (in blue) vs. matrix-compressed preconditioner (in red).

As second example for this application SERS substrate suspended in water was analyzed at $\lambda = 550nm$ shown in Fig. 4.23. Each nanosphere is discretized with 270 RWG basis for the electric and magnetic surface currents, and its made of gold ($\epsilon_r = 5.9310 - j2.0971$ at λ =550nm).

This particular structure is challenging for the matrix compression method used due to the proximity between elements. As stated for the structure shown in Fig. 4.17, the problem is caused by the reactive fields, modeled by the high order macrobasis that are not considered in the compressed system. However, as we are not aiming for an exact solution in the inner solver but an approximated one to accelerate the convergence of the main solver, these effects can be ignored in the preconditioning process, as they will be taken into account in the main solver. Despite this, it is recommended to properly set-up the preconditioner, as in other case it may cause stagnation problems to the main solver.

The setup of the preconditioner for this second case is equal to the first example, but using a 10% of the total macrobasis to avoid stagnation (incapability to improve the residual for several iterations) in the GMRES solver. The improvement in the convergence is shown in Fig. 4.24, reducing the total number of iterations from 79 to 13, whereas in terms of total wall-clock time, the improvement gives place to a speed-up equal to x2.4.

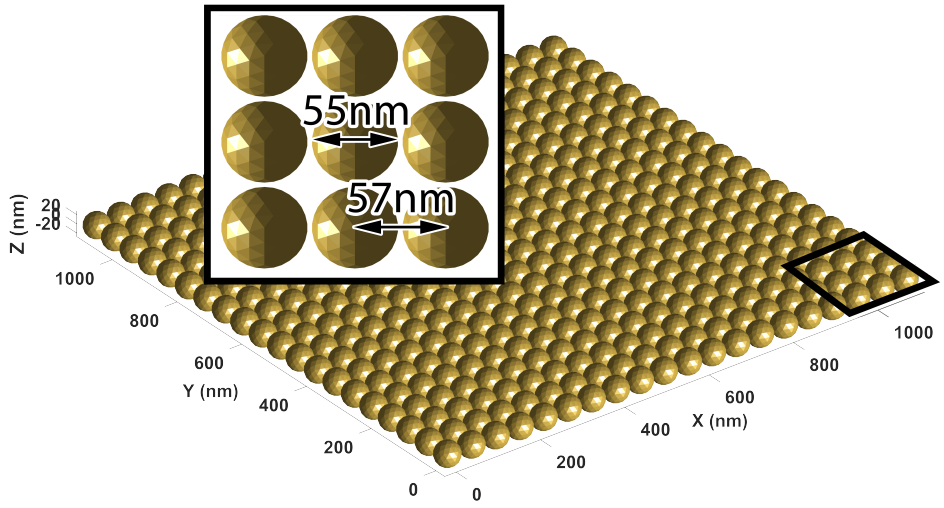

Figure 4.23: Representation of a SERS substrate composed of 20×20 gold nano-spheres ($\epsilon_r = -5.9310 - j2.0971$ at 550nm) of 55nm of diameter and a separation of 57nm between centers.

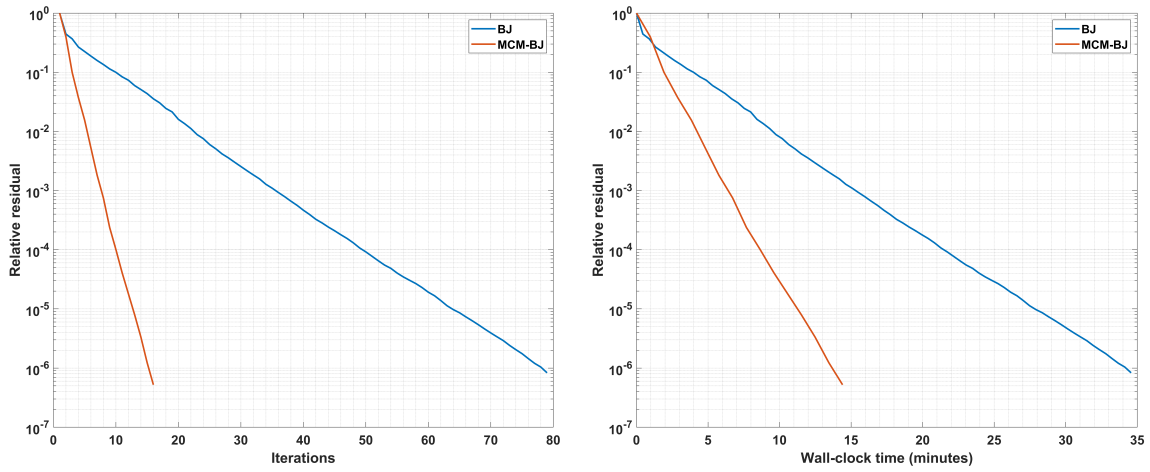

(a) convergence vs. number of iterations.

(b) convergence vs. wall-clock time.

Figure 4.24: Evolution of the convergence vs. number of iterations of the iterative solution of the structure shown in Fig. 4.23 made of gold ($\epsilon_r = -5.9310 - j2.0971$) preconditioned with a block-jacobi preconditioner (in blue) vs. matrix-compressed preconditioner (in red).

Chapter 5

Conclusion and future lines

5.1 Conclusion

The work developed in this thesis can be classified into two main lines.First, a novel method (namely slotFFT) has been devised and implemented for the accurate analysis of finite periodic structures. Secondly, a novel set of macrobasis was proposed for the compression of radiation problems.

The core method of this thesis is slotFFT, which has been developed in two different versions (single and double sampling). The method has proven to be an efficient approach to analyze periodic structures maintaining the precision of the SIE-MoM reference method, which lies underneath the algorithm, but reducing the computational cost of **exactly** performing the MVP from $\mathcal{O}N^2$ to $\mathcal{O}N\log(M)$.

The method has been applied to several problems in different disciplines in which there is a demand to analyze finite periodic structures quickly and with methods capable of the analysis of large finite problems with methods capable of approaching the problem without approximations. This This is the case of SERS substrates made up of periodical assemblies of nanoparticles, where global effects usually appear hybridizing the nanoparticle modes. A different example was the comparison of the ensemble of nanocubes with the equivalent homogeneized version with the Maxwell-Garnett and Bruggeman formulas, where some differences could be seen.

Also some applications in the limits of the thesis were studied, extending the algorithm with negligible costs and simple code modifications to especial cases. In particular, the method was firstly extended to periodic structures with aperiodic element-wise

materials. This extension enables the application of slotFFT to approach particular optimization problems, like discrete dielectric lenses. The second extension of the method was based on the the Huygens' equivalence theorem, enabling the analysis of non periodic structures by introducing a periodic array of Huygens' surfaces enclosing the elements of the structure. This last extension paves the way to the analysis of some appealing problems: metamaterials, metasurfaces, reflectarrays, transmitarrays, etc. Furthermore, it allows to introduce fabrication defects in order to properly characterize structures through an approach closer to reality.

The second part of the thesis was devoted to the development of a novel set of macrobasis based on the conservation of the energy theorem. The complete development proves the ease of its implementation with existing SIE-MoM codes. This new set of macrobasis has proven to be extremely effective describing the radiation of the bodies in lossless mediums through the low order macrobasis, being able to describe closely the radiation using up to a 2% of the total degrees of freedom. This was tested in different ways. In particular, the most novel was the application of the method to compare the differences between and object and its invisibilized version using a multilayer dielectric filler. In particular, it could be observed that that in the case of the low order macrobasis associated to the object were radiating less in the case with the filler in contrast to the empty object.

In the third part, two matrix compression methods were integrated into slotFFT. The first one was the mentioned set of macrobasis functions, and the second one was the skeleton decomposition, which was integrated in a joint activity with the Laboratory of Advance Communications and Electromagnetics (LACE) of the Politecnico di Torino. In the problems studied, it was observed that, when applied to reception, the macrobasis compression presented precision problems for all the tested integral equation formulations, with the exception of PMCHWT. This problem has not been solved in the thesis and is still open.

The examples analyzed proved that slotFFT in addition to matrix compression methods (MCM) can achieve high speed-ups with controlled impact over the precision with the methods integrated. Despite this, the macrobasis shown a slightly better result over the precision. At last, the integrated framework of slotFFT and MCM was applied as a preconditioner for finite periodic structures, achieving speed-ups via convergence even when applied to rough problems with plasmonic effects.

5.2 Future lines

There are four lines of work to be tackled in the near future. The first one is the integration of the developed framework into M-Cube, the CEM library of the research group. This could have potential when combined with other consolidated methods, like the domain decomposition method, to deal with large dense structures in a different approach.

The second line of work is the optimization of the codes for roughly periodic problems, which shows potential to approach new kind of problems that are at its peak, like metamaterials or new kind or quasi-periodic antennas. In its current stage, the method is valid and can approach several new kind of structures, but due to the current implementation is still inefficient in terms of computing time, as the computation of the local part enclosed by each Huygens' surface takes an important number of additional operations.

The resulting open problem when using macrobasis to perform matrix compression in reception conforms an additional line of work. Despite of being intended for radiating, the fact that the developed set of macrobasis works in both radiation and reception aims in the direction of some problem related to the SIE-MoM core for other formulations. A deeper study on the possible causes of this issue is need in order to extend the method to other formulations to compensate the limitations that PMCHWT formulations present of specific problems.

At last, the fourth line is the application of the developed framework for the optimization of discrete periodic problems, as shown in section 3.4. The analysis of this kind of problems with enough precision require the use of high performance computers, as the problem itself is large and usually are required many individuals in the population for the optimization algorithm in order to attain good results. The combination of slotFFT with the MCM developed allows to perform this kind of processes with affordable computers.

Bibliography

[1] Javier Rivero Campos. *Electromagnetismo Computacional Avanzado para Materiales Artificiales y Nanoestructuras Plasmónicas.* PhD thesis, University of Extremadura, 2012.

[2] Diego Martínez Solís. *Advanced Methods on Computational Electromagnetics and their Application to the Study of Plasmonics and Metamaterials.* PhD thesis, University of Vigo, 2014.

[3] M. G. Araüjo, J. M. Taboada, J. Rivero, and F. Obelleiro. Comparison of surface integral equations for left-handed materials. *Progress in Electromagnetics Research*, 118:425–440, 2011.

[4] M. G. Araújo, J. M. Taboada, D. M. Solís, J. Rivero, L. Landesa, and F. Obelleiro. Comparison of surface integral equation formulations for electromagnetic analysis of plasmonic nanoscatterers. *Optics Express*, 20(8):9161–9171, 2012.

[5] L. Landesa, M. G. Araújo, J. M. Taboada, L. Bote, and F. Obelleiro. Improving condition number and convergence of the surface integral-equation method of moments for penetrable bodies. *Optics Express*, 20(15):17237–17249, 2012.

[6] J. M. Taboada, J. Rivero, F. Obelleiro, M. G. Araújo, and L. Landesa. Method-of-moments formulation for the analysis of plasmonic nano-optical antennas. *Journal of the Optical Society of America A: Optics and Image Science, and Vision*, 28(7):1341–1348, 2011.

[7] M. G. Araujo, J. M. Taboada, J. Rivero, D. M. Solis, F. Obelleiro, and L. Landesa. Electromagnetic analysis of metamaterials and plasmonic nanostructures with the method of moments. *IEEE Antennas and Propagation Magazine*, 54(6):81–91, 2012.

[8] J. M. Taboada, M. G. Araújo, J. Rivero, L. Landesa, and F. Obelleiro. Surface integral equation solvers for large-scale conductors, metamaterials and plasmonic nanostructures. *Applied Computational Electromagnetics Society Journal*, 27(2):189–197, 2012.

[9] Roger F. Harrington. *Field Computation by Moment Methods*. Wiley-IEEE Press, 1993.

[10] S. M. Rao, D. R. Wilton, and A. W. Glisson. Electromagnetic scattering by surfaces of arbitrary shape. *IEEE Transactions on Antennas and Propagation*, 30(3):409–418, 1982.

[11] R. F. Harrington. *Time-Harmonic Electromagnetic Fields*. IEEE Press Series on Electromagnetic Wave Theory, USA, 2001.

[12] P. Ylä-Oijala, M. Taskinen, and S. Järvenpää. Surface integral equation formulations for solving electromagnetic scattering problems with iterative methods. *Radio Sci.*, 40(6):RS6002, 2005.

[13] M. G. Araújo, J. M. Taboada, J. Rivero, and F. Obelleiro. Comparison of surface integral equations for left-handed materials. *Prog. Electromagn. Res.*, 118:425–440, 2011.

[14] A. J. Poggio and E. K. Miller. *Computer Techniques for Electromagnetics*. Elmsford, NY: Permagon, USA, 1973.

[15] M. E. Veysoglu, R. T. Shin, and J. A. Kong. A Finite-Difference Time-Domain analysis of wave scattering from periodic surfaces: Oblique incidence case. *Journal of Electromagnetic Waves and Applications*, 7(12):1595–1607, 1993.

[16] Pochi Yeh, Amnon Yariv, and Chi-Shain Hong. Electromagnetic propagation in periodic stratified media. I. General theory. *J. Opt. Soc. Am.*, 67(4):423–438, Apr 1977.

[17] R. C. Hall, R. Mittra, and K. M. Mitzner. Analysis of multilayered periodic structures using generalized scattering matrix theory. *IEEE Transactions on Antennas and Propagation*, 36(4):511–517, 1988.

[18] T. K. Mealy, I. A. Eshrah, and T. M. Abuelfadl. Solution of periodically loaded waveguides using the eigenmode projection technique. In *2016 IEEE MTT-S International Microwave Symposium (IMS)*, pages 1–4, 2016.

[19] A. F. Abdelshafy, M. A. K. Othman, D. Oshmarin, A. T. Almutawa, and F. Capolino. Exceptional points of degeneracy in periodic coupled waveguides and the interplay of gain and radiation loss: Theoretical and experimental demonstration. *IEEE Transactions on Antennas and Propagation*, 67(11):6909–6923, 2019.

[20] O. Ergul and L. Gurel. *The Multilevel Fast Multipole Algorithm (MLFMA) for Solving Large-Scale Computational Electromagnetics Problems*. Wiley-IEEE Press, 2014.

[21] O. Ergul and L. Gurel. Accurate solutions of extremely large integral-equation problems in computational electromagnetics. *Proceedings of the IEEE*, 101(2):342–349, Feb 2013.

[22] O. Ergul. Analysis of composite nanoparticles with surface integral equations and the Multilevel Fast Multipole Algorithm. *Journal of Optics*, 14(6):062701, 2012.

[23] L. Gürel, Ö. Ergül, A. Ünal, and T. Malas. Fast and accurate analysis of large metamaterial structures using the multilevel fast multipole algorithm. *Progress in Electromagnetics Research*, 95:179–198, 2009.

[24] O. Ergul and L. Gurel. Fast and accurate analysis of large-scale composite structures with the parallel Multilevel Fast Multipole Algorithm. *J. Opt. Soc. Am. A*, 30(3):509–517, Mar 2013.

[25] J. M. Taboada, M. G. Araujo, J. M. Bertolo, L. Landesa, F. Obelleiro, and J. L. Rodriguez. MLFMA-FFT parallel algorithm for the solution of large-scale problems in electromagnetics. *Progress In Electromagnetics Research*, 105(3):15–30, Feb 2010.

[26] J. M. Taboada, M. G. Araujo, F. Obelleiro, J. L. Rodriguez, and L. Landesa. MLFMA-FFT parallel algorithm for the solution of extremely large problems in electromagnetics. *Proceedings of the IEEE*, 101(2):350–363, Feb 2013.

[27] M. G. Araujo, J. M. Taboada, J. Rivero, D. M. Solis, and F. Obelleiro. Solution of large-scale plasmonic problems with the multilevel fast multipole algorithm. *Opt. Lett.*, 37(3):416–418, Feb 2012.

[28] I. García-Tuñón, J. M. Taboada, J. L. Rodríguez, F. Obelleiro, and L. Landesa. Efficient asymptotic-phase modeling of the induced currents in the fast multipole method. *Microwave and Optical Technology Letters*, 48(8):1594–1599, 2006.

[29] J.C. Mouriño, A. Gómez, J.M. Taboada, L. Landesa, J.M. Bértolo, F. Obelleiro, and J.L. Rodríguez. High scalability multipole method. solving half billion of unknowns. *Computer Science - Research and Development*, 23(3-4):169–175, 2009.

[30] X.-C. Nie, L.-W. Li, and N. Yuan. Precorrected-FFT algorithm for solving combined field integral equations in electromagnetic scattering. *J. of Electromagn. Waves and Appl*, 16:1171–1187, 2002.

[31] V. Okhmatovski, M. Yuan, I. Jeffrey, and R. Phelps. A three-dimensional precorrected FFT algorithm for fast Method of Moments solutions of the mixed-potential integral equation in layered media. *IEEE Transactions on Microwave Theory and Techniques*, 57(12):3505–3517, Dec 2009.

[32] K. Xiao, F. Zhao, S.-L. Chai, J.-J. Mao, and J. L.-W. Li. Scattering analysis of periodic arrays using combined cbf/p-fft method. *Progress In Electromagnetics Research*, 115(131-146):169–175, 2011.

[33] K. Xiao, H. Qi, S. S. Wang, Y. Liu, L. Ding, and S. . Chai. Efficient analysis of rectangular-shape metamaterials using p-cbfm/p-fft method. *Progress In Electromagnetics Research M*, 51:121–129, 2016.

[34] Kai Yang, Fangzhou Wei, and A.E. Yilmaz. Truncated multigrid versus precorrected fft/aim for bioelectromagnetics: When is o(n) better than o(nlogn)? In *Computational Electromagnetics International Workshop (CEM), 2011*, pages 153–158, Aug 2011.

[35] Xiao-Chun Nie, Le-Wei Li, and Ning Yuan. Precorrected-fft algorithm for solving combined field integral equations in electromagnetic scattering. In *IEEE Antennas and Propagation Society International Symposium (IEEE Cat. No.02CH37313)*, volume 3, pages 574–577 vol.3, 2002.

[36] Manuel F. Catedra, Rafael P. Torres, Jose Basterrechea, and Emilio Gago. *The CG-FFT Method: Application of Signal Processing Techniques to Electromagnetics*. Artech House, 1995.

[37] Benjamin E. Barrowes, Fernando L. Teixeira, and Jin A. Kong. Fast algorithm for matrix–vector multiply of asymmetric multilevel block-Toeplitz matrices in 3-D scattering. *Microwave and Optical Technology Letters*, 31(1):28–32, 2001.

[38] Y. Zhang, J. Y. Li, C. H. Liang, and Y. J. Xie. A fast analysis of large finite-slot phased arrays fed by rectangular waveguides. *Journal of Electromagnetic Waves and Applications*, 18(6):715–727, 2004.

[39] Huiqing Zhai, Qiang Chen, Qiaoewi Yuan, Kunio Sawaya, and Changhong Liang. Analysis of large-scale periodic array antennas by CG-FFT combined with equivalent sub-array preconditioner. *IEICE Transactions on Electronics*, E89B(3):922–928, Mar 2006.

[40] E. H. Bleszynski, M. K. Bleszynski, and T. Jaroszewicz. Block-Toeplitz fast integral equation solver for large finite periodic and partially periodic antenna arrays. In *2003 IEEE Topical Conference on Wireless Communication Technology*, pages 428–429, Oct 2003.

[41] Elizabeth H. Bleszynski, Marek K. Bleszynski, and Thomas Jaroszewicz. Block-Toeplitz fast integral equation solver for large finite periodic and partially periodic array systems. *IEICE Transactions on Electronics*, E87C(9):1586–1594, Sep 2004.

[42] Xing-Xiang Liu, Jackson W. Massey, Ming-Feng Wu, Kristopher T. Kim, Robert A. Shore, Ali E. Yilmaz, and Andrea Alù. Homogenization of three-dimensional metamaterial objects and validation by a fast surface-integral equation solver. *Opt. Express*, 21(19):21714–21727, Sep 2013.

[43] A. J. Pickles and M. B. Steer. Effective permittivity of 3-d periodic composites with regular and irregular inclusions. *IEEE Access*, 1:523–536, 2013.

[44] Alberto Serna, Mario F. Manzano, Luis Landesa, Diego M. Solis, and Jose M. Taboada. Fast and accurate electromagnetic solutions of finite periodic optical structures. *Opt. Express*, 25(15):18031–18039, Jul 2017.

[45] Sebastian Schlücker. Surface-enhanced raman spectroscopy: Concepts and chemical applications. *Angewandte Chemie International Edition*, 53(19):4756–4795, 2014.

[46] R. A. Alvarez-Puebla and L. M. Liz-Marzán. Sers-based diagnosis and biodetection," small, vol. 6, no. 5, pp. 604–610, 2010.,. *Small*, 6(5):604–610, 2010.

[47] D. M. Solis, J. M. Taboada, L. Landesa, J. L. Rodriguez, and F. Obelleiro. Squeezing maxwell's equations into the nanoscale (invited paper). *Progress In Electromagnetics Research*, 154:35–50, 2015.

[48] Alberto Serna, Luis Landesa, Mario F. Manzano, and Jose M. Taboada. Solving extremely large periodic structures through slot fft techniques. In *XXXIII Simposium Nacional de la Unión Científica Internacional de Radio*, 2018.

[49] J. George and K. George Thomas. Surface plasmon coupled circular dichroism of au nanoparticles on peptide nanotubes. *Journal of the American Chemical Society*, 132(8):2502–2503, 2010.

[50] J. Kumar, H. Eraña, E. López-Martínez, N. Claes, V. F. Martín, D. M. Solís, S. Bals, A. L. Cortajarena, J. Castilla, and L. M. Liz-Marzán. Detection of amyloid fibrils in parkinson's disease using plasmonic chirality. *Proceedings of the National Academy of Sciences of the United States of America*, 115(13):3225–3230, 2018.

[51] K. W. Smith, H. Zhao, H. Zhang, A. Sánchez-Iglesias, M. Grzelczak, Y. Wang, W. . Chang, P. Nordlander, L. M. Liz-Marzán, and S. Link. Chiral and achiral nanodumbbell dimers: The effect of geometry on plasmonic properties. *ACS Nano*, 10(6):6180–6188, 2016. Cited By :43.

[52] D. M. Solís, J. M. Taboada, F. Obelleiro, L. M. Liz-Marzán, and F. J. García De Abajo. Toward ultimate nanoplasmonics modeling. *ACS Nano*, 8(8):7559–7570, 2014.

[53] J. Kumar, H. Eraña, E. López-Martínez, N. Claes, V. F. Martín, D. M. Solís, S. Bals, A. L. Cortajarena, J. Castilla, and L. M. Liz-Marzán. Detection of amyloid fibrils in parkinson's disease using plasmonic chirality. *Proceedings of the National Academy of Sciences of the United States of America*, 115(13):3225–3230, 2018.

[54] A. Serna, L. Landesa, and J. M. Taboada. Electromagnetic analysis of finite arrays with aperiodical element-wise materials. In *Proceedings of the 2019 21st International Conference on Electromagnetics in Advanced Applications, ICEAA 2019*, page 734, 2019.

[55] M. Lapine, L. Jelinek, R. Marqués, and M. J. Freire. Exact modelling method for discrete finite metamaterial lens. *IET Microwaves, Antennas and Propagation*, 4(8):1132–1139, 2010.

[56] J. A. T. Vasquez, Z. Peng, J. . Lee, G. Vecchi, and F. Vipiana. Automatic localized nonconformal mesh refinement for surface integral equations. *IEEE Transactions on Antennas and Propagation*, 68(2):967–975, 2020.

[57] V. V. S. Prakash and Raj Mittra. Characteristic basis function method: A new technique for efficient solution of method of moments matrix equations. *Microwave and Optical Technology Letters*, 36(2):95–100, 2003.

[58] E. Lucente, A. Monorchio, and R. Mittra. An iteration-free mom approach based on excitation independent characteristic basis functions for solving large multi-scale electromagnetic scattering problems. *IEEE Transactions on Antennas and Propagation*, 56(4):999–1007, April 2008.

[59] J. Laviada, F. Las-Heras, M. R. Pino, and R. Mittra. Solution of electrically large problems with multilevel characteristic basis functions. *IEEE Transactions on Antennas and Propagation*, 57(10 PART 2):3189–3198, 2009.

[60] R. Mittra and K. Du. Characteristic basis function method for iteration-free solution of large method of moments problems. *Progress In Electromagnetics Research B*, 6:307–336, 2008.

[61] J. Yeo, S. Köksoy, V. V. S. Prakash, and R. Mittra. Efficient generation of method of moments matrices using the characteristic function method. *IEEE Transactions on Antennas and Propagation*, 52(12):3405–3410, 2004.

[62] K. Yoo, N. Mehta, and R. Mittra. A new numerical technique for analysis of periodic structures. *Microwave and Optical Technology Letters*, 53(10):2332–2340, 2011.

[63] L. Hu, L. . Li, and R. Mittra. Electromagnetic scattering by finite periodic arrays using the characteristic basis function and adaptive integral methods. *IEEE Transactions on Antennas and Propagation*, 58(9):3086–3090, 2010.

[64] Kezhong Zhao, M. N. Vouvakis, and Jin-Fa Lee. The adaptive cross approximation algorithm for accelerated method of moments computations of emc problems. *IEEE Transactions on Electromagnetic Compatibility*, 47(4):763–773, Nov 2005.

[65] J. M. Tamayo, A. Heldring, and J. M. Rius. Multilevel adaptive cross approximation (mlaca). *IEEE Transactions on Antennas and Propagation*, 59(12):4600–4608, Dec 2011.

[66] A. Heldring, E. Ubeda, and J. M. Rius. On the convergence of the aca algorithm for radiation and scattering problems. *IEEE Transactions on Antennas and Propagation*, 62(7):3806–3809, July 2014.

[67] M. Bebendorf and S. Kunis. Recompression techniques for adaptive cross approximation. *Journal of Integral Equations and Applications*, 21(3):331–357, 2009.

[68] M. Bebendorf and R. Kriemann. Fast parallel solution of boundary integral equations and related problems. *Computing and Visualization in Science*, 8(3-4):121–135, 2005.

[69] M. Bebendorf. Adaptive cross approximation of multivariate functions. *Constructive Approximation*, 34(2):149–179, 2011.

[70] M. Bebendorf. Approximation of boundary element matrices. *Numerische Mathematik*, 86(4):565–589, 2000.

[71] I. Fenni, H. Roussel, M. Darces, and R. Mittra. Efficiency enhancement of the characteristic basis function method for modeling forest scattering using the adaptive cross approximation algorithm. *IEEE Transactions on Antennas and Propagation*, 64(10):4539–4544, Oct 2016.

[72] L. Matekovits, V. A. Laza, and G. Vecchi. Analysis of large complex structures with the synthetic-functions approach. *IEEE Transactions on Antennas and Propagation*, 55(9):2509–2521, Sept 2007.

[73] L. Matekovits, G. Vecchi, M. Bercigli, and M. Bandinelli. Synthetic-functions analysis of large aperture-coupled antennas. *IEEE Transactions on Antennas and Propagation*, 57(7):1936–1943, 2009.

[74] M. Bebendorf and R. Venn. Constructing nested bases approximations from the entries of non-local operators. *Numerische Mathematik*, 121(4):609–635, Aug 2012.

[75] M. Li, M. A. Francavilla, F. Vipiana, G. Vecchi, and R. Chen. Nested equivalent source approximation for the modeling of multiscale structures. *IEEE Transactions on Antennas and Propagation*, 62(7):3664–3678, July 2014.

[76] M. Li, M. A. Francavilla, R. Chen, and G. Vecchi. Wideband fast kernel-independent modeling of large multiscale structures via nested equivalent source approximation. *IEEE Transactions on Antennas and Propagation*, 63(5):2122–2134, 2015.

[77] M. Li, M. A. Francavilla, R. Chen, and G. Vecchi. Nested equivalent source approximation for the modeling of penetrable bodies. *IEEE Transactions on Antennas and Propagation*, 65(2):954–959, 2017.

[78] K. Ho and L. Greengard. A fast direct solver for structured linear systems by recursive skeletonization. *SIAM Journal on Scientific Computing*, 34(5):A2507–A2532, 2012.

[79] H. Cheng, Z. Gimbutas, P. G. Martinsson, and V. Rokhlin. On the compression of low rank matrices. *SIAM Journal on Scientific Computing*, 26(4):1389–1404, 2005.

[80] M. A. E. Bautista, M. A. Francavilla, P. Martinsson, and F. Vipiana. $\mathcal{O}(n)$ nested skeletonization scheme for the analysis of multiscale structures using the method of moments. *IEEE Journal on Multiscale and Multiphysics Computational Techniques*, 1:139–150, 2016.

[81] Z. Rong, M. Jiang, Y. Chen, L. Lei, Z. Nie, and J. Hu. Fast direct surface integral equation solution for electromagnetic scattering analysis with skeletonization factorization. *IEEE Transactions on Antennas and Propagation*, 68(4):3016–3025, 2020.

[82] Luis Landesa, Alberto Serna, and Jose M. Taboada. Macrobases desacopladas en potencia para el método de los momentos de dispersores dieléctricos. In *XXXIII Simposium Nacional de la Unión Científica Internacional de Radio*, 2018.

[83] Luis Landesa, Alberto Serna, and J. M. Taboada. Aceleración de problemas periódicos finitos mediante vases desacopladas y slotfft. In *XXXIV Simposium Nacional de la Unión Científica Internacional de Radio*, 2019.

[84] A. Serna, L. Landesa, and J. M. Taboada. Acceleration of finite periodic structures analysis through full-domain basis for matrix compression. In *2019 IEEE International Symposium on Antennas and Propagation and USNC-URSI Radio Science Meeting, APSURSI 2019 - Proceedings*, pages 1687–1688, 2019.

[85] A. Serna, J. T. Vasquez, J. Rivero, L. Landesa, and F. Vipiana. Acceleration of finite periodic structures analysis through matrix compression techniques. In *13th European Conference on Antennas and Propagation, EuCAP 2019*, 2019.

[86] L. Landesa, A. Serna, M. F. Manzano, J. M. Taboada, and D. M. Solis. Slotfft techniques for fast computation of large and periodic electromagnetics problems.

In *CEM 2017 - 2017 Computing and Electromagnetics International Workshop*, pages 57–58, 2017.

[87] A. Serna, L. Landesa, J. M. Taboada, and M. F. Manzano. Distributed macrobasis decomposition for the electromagnetic solution of large periodic structures. In *2017 International Applied Computational Electromagnetics Society Symposium - Italy, ACES 2017*, 2017.

[88] Gloria Gajardo Silva. *Transformaciones basadas en la radiació electromagnética con aplicaciones en aceleración y compresión.* PhD thesis, University of Extremadura, 2011.

[89] A. Serna, L. J. Molina, J. Rivero, L. Landesa, and J. M. Taboada. Multilayer homogeneous dielectric filler for electromagnetic invisibility. *Scientific Reports*, 8(1), 2018.

[90] R. Kitamura, L. Pilon, and M. Jonasz. Optical constants of silica glass from extreme ultraviolet to far infrared at near room temperature. *Appl. Opt.*, 46:8118–8133, 2007.

[91] Mario Echeverri. *Fast solvers for integral equations in electromagnetics.* PhD thesis, Politecnico di Torino, May 2016.

[92] P. . Martinsson and V. Rokhlin. A fast direct solver for boundary integral equations in two dimensions. *Journal of Computational Physics*, 205(1):1–23, 2005.

[93] J. . Wei, Z. Peng, and J. . Lee. A fast direct matrix solver for surface integral equation methods for electromagnetic wave scattering from non-penetrable targets. *Radio Science*, 47(4), 2012.

[94] X. Pan and X. Sheng. Hierarchical interpolative decomposition multilevel fast multipole algorithm for dynamic electromagnetic simulations. *Progress in Electromagnetics Research*, 134:79–94, 2012.

[95] T. Malas, Ö. Ergül, and L. Gürel. Approximate mlfma as an efficient preconditioner. In *IEEE Antennas and Propagation Society, AP-S International Symposium (Digest)*, pages 1289–1292, 2007.